TWO-PROTON CORRELATIONS IN p+Pb AND S+Pb COLLISIONS AT THE CERN SUPER PROTON SYNCHROTRON

Maxim Potekhin

Advisor: Professor William Willis

Submitted in partial fulfillment of
the requirements for the degree
of Doctor of Philosophy in the
Graduate School of Arts and Sciences

Columbia University

1996

©1996

Maxim Potekhin

All Rights Reserved

ABSTRACT

TWO-PROTON CORRELATIONS IN p+Pb AND S+Pb COLLISIONS AT THE CERN SUPER PROTON SYNCHROTRON

Maxim Potekhin

Two–proton correlations in ^{32}S+^{208}Pb collisions at 200 GeV/c per nucleon and p+^{208}Pb collisions at 450 GeV/c are presented, as measured by the focusing spectrometer of the NA44 experiment at CERN. The technique of intensity interferometry of pairs with low relative momentum has been used. A dependence of the correlation function on the event multiplicity is found. A detailed Monte Carlo calculation has been performed for the purpose of comparison of the data with the `RQMD` model, taking into account effects relating to the acceptance, momentum resolution and track reconstruction in the apparatus, as well as contamination of the proton sample by Λ decays. The centrality of the events studied was estimated using data from a silicon multiplicity detector and a `GEANT` based simulation of that detector. We find that the `RQMD` predictions do not agree with the data. If the strange baryon contribution is estimated from the available experimental data rather than `RQMD`, an additional systematic uncertainty margin is introduced, making the discrepancy between Monte Carlo and the data less significant. The difference could be interpreted as an indication that the measured proton source, in S+Pb reactions, is somewhat larger than predicted by `RQMD` (this is less certain for p+Pb). An alternative interpretation is that dynamical effects in `RQMD` are different from those in the actual source.

Contents

List of Figures

List of Tables

Acknowledgements

Many people contributed to this thesis, directly and indirectly. To all of them I wish to express my sincere gratitude.

First of all, I thank the members of the NA44 Collaboration for being good friends and good professionals. Jeremy Dodd gave me crucial moral as well as practical support and helped me to improve this document significantly. I would like to thank Martin Sarabura, who helped me to learn about the NA44 software; Achim Franz, whose expertise and industrious spirit made possible the successful running of the experiment; Gilbert Poulard, who managed the NA44 software complex.

Raymond Lee, Hal Kalechofsky and Sanjeev Pandey made a contribution to NA44 that can't be exaggerated. The Los Alamos team, and John Sullivan and Hubert Van Hecke in particular, were always extremely helpful. I thank Jehanne Simon-Gillo for her support when we worked together on the uranium calorimeter. My friends from Hiroshima University, S.Esumi, N.Maeda, S.Nishimura, A.Sakaguchi, Prof. T.Sugitate and others performed the difficult and essential task of the hodoscope maintenance and calibration and thus actually made NA44 possible, and also contributed, in no trivial manner, to the analysis and interpretation of the data.

I am very grateful to my thesis advisor, Prof. W.Willis, for his constant support. I also wish to thank Prof. H.Bøggild, Prof. C.Fabjan, Prof. T.Humanic, Prof. B.Jacak for their guidance.

Professors W. Zajc and B. Cole of Columbia University were always willing to discuss difficult topics of this thesis. Mikhail Leltchouk has assisted in managing parts of the Monte Carlo calculations. Prof. A. Blaer was one of those who made learning physics a wonderful experience for me and many other Columbia students.

Scott Pratt of Michigan State University provided an important piece of computer code and often helped me with his expert advice. I wish to thank Michael Murray (Texas A&M) for many useful discussions.

I really enjoyed the many years I spent in physics. I am grateful to my high school physics teacher, L.Pigalitzin, for showing me the ultimate beauty of this science. Prof. Boris Dolgoshein was my teacher, advisor and, to put it plainly, boss, in 1984-1991 and, through his personality, expertise and enthusiasm added a lot to the inspiration that guided me through much of my life. Pavel Nevsky taught me a better programming style and helped in matters big and small during the last 12 years.

Finally, I gratefully acknowledge my indebtedness to my parents, Valery and

Irina Potekhin, whose support and faith in me never failed and who taught me to work hard and strive for knowledge. I am grateful to all my friends, whose love, friendship and support make life worth living.

To my parents

Chapter 1

Introduction

1.1 General introduction

The physics of heavy-ion collisions is an interdisciplinary field that has emerged from particle physics and nuclear physics. Its subject is the study of bulk matter consisting of strongly interacting particles, under extreme conditions. As this suggests, a connection has to be made between the elementary interaction aspect of such a system, and its "macroscopic" properties. The hope is to describe complex multiparticle states using the language of thermodynamics and macroscopic variables such as temperature, density, entropy etc.

In essence, Relativistic Heavy Ion Collisions *(RHIC)* serve as a tool to examine the behavior of nuclear matter under conditions of temperature and density that are much higher than those existing in "normal" nuclei. The most exciting prediction of QCD is that under such conditions, a transition happens into a new state, the quark-gluon plasma (QGP), where partons become deconfined [1, 2, 3]. The phase diagram of nuclear matter, in the form T vs ρ, is shown in Fig. 1.1.

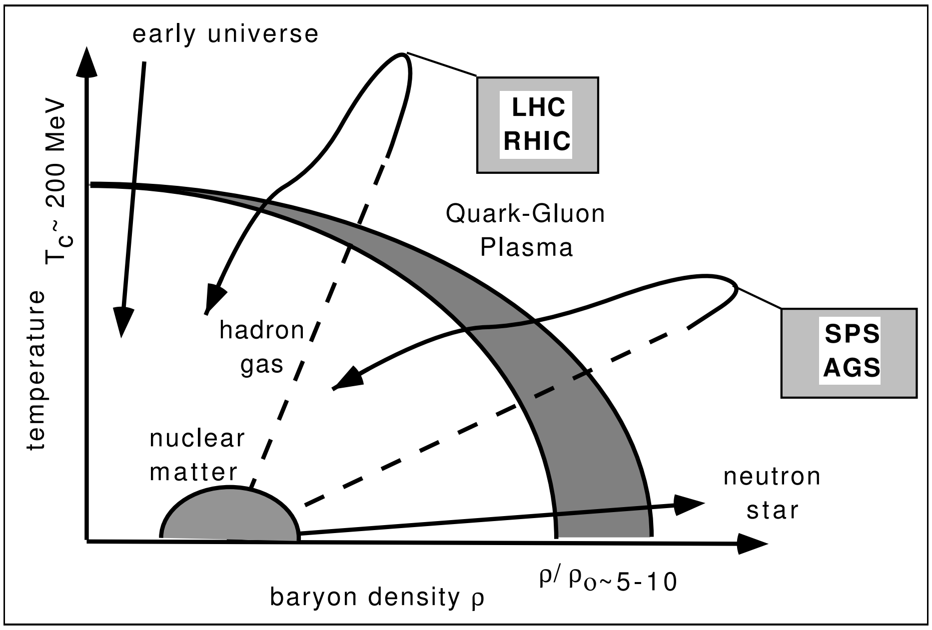

Figure 1.1: The Phase Diagram

Studying this phenomenon is of interest because

- it could provide insight into the nature of confinement, i.e. non-observability of free quarks and gluons, the nature of the QCD vacuum, and, therefore, advance our understanding of the strong interaction
- hot and compressed nuclear matter was present in early stages of the evolution of the Universe; it is believed that the quark–hadron phase transition took place approximately 10^{-5} seconds after the Big Bang [4, 3], and features of this transition, such as long-range density fluctuations, may be significant in cosmology
- in astrophysics, the dynamics of supernova explosions and the stability of

neutron stars depend on the compressibility and therefore the equation of state of nuclear matter

The utility of *RHIC* as a tool to create and study QGP depends on a number of conditions [3]:

- the energy density should be sufficient for QGP formation, and according to QCD must be of the order of 1-3 GeV/fm^3
- in order for macroscopic variables to be applicable, the system has to be much bigger than the typical scale of strong interaction (1 fm) and to consist of a large number of particles
- the lifetime of the system has to be long enough for it to reach equilibrium, otherwise thermodynamic concepts wouldn't be applicable

Experimental verification of these conditions is an important topic in the heavy-ion research. In fact, quite generally, we may say that the task of experiments is to (a) assess the initial conditions, (b) search for signals of the possible phase transition.

1.2 Relativistic Heavy Ion Collisions *(RHIC)*

1.2.1 The Role of Geometry and Stopping in *RHIC*

The small Compton wavelength ($\hbar/mc$) of the nucleons participating in *RHIC* makes it possible to disregard the quantum-mechanical uncertainty in shape and position of the participating nuclei, and consider the collision from the point of view of straight-line geometry.

A sketch of a reaction between two asymmetric nuclei is shown in Fig. 1.2. The collision is characterized by the impact parameter (further referred to as "b"), and the projectile nucleus effectively bores a hole through the target nucleus. Hence, the nucleons fall into two categories: participants, that are contained in the overlapping zone of both nuclei (sometimes referred to as "bore cylinder"), and spectators, located outside of that zone, which proceed with little perturbation along their original path [3, 5][1].

In order to describe the kinematics of particles participating in the collision, the *rapidity variable* y is very commonly used (see Appendix A). In terms of y we can distinguish nucleons in the region of *target* rapidity, y_{target}, and the *projectile* rapidity, $y_{projectile}$. The overlapping zone defined in the geometrical picture discussed above corresponds to the kinematic region between the target and the projectile, that is often referred to as "central" or mid-rapidity.

In the overlapping zone, a fraction of the kinetic energy of the projectile–target system is deposited, via hard scattering on the parton level as well as soft nucleon-nucleon collisions, and details of this process actually depend on the energy and volume of the colliding nuclei. The degree to which the participant nucleons decelerate in the process of the collision and the amount of energy deposited in the reaction volume are usually referred to in terms of the so-called *stopping* [6, 2]

[1]However, the remnant of the nucleus is excited and likely to fragment

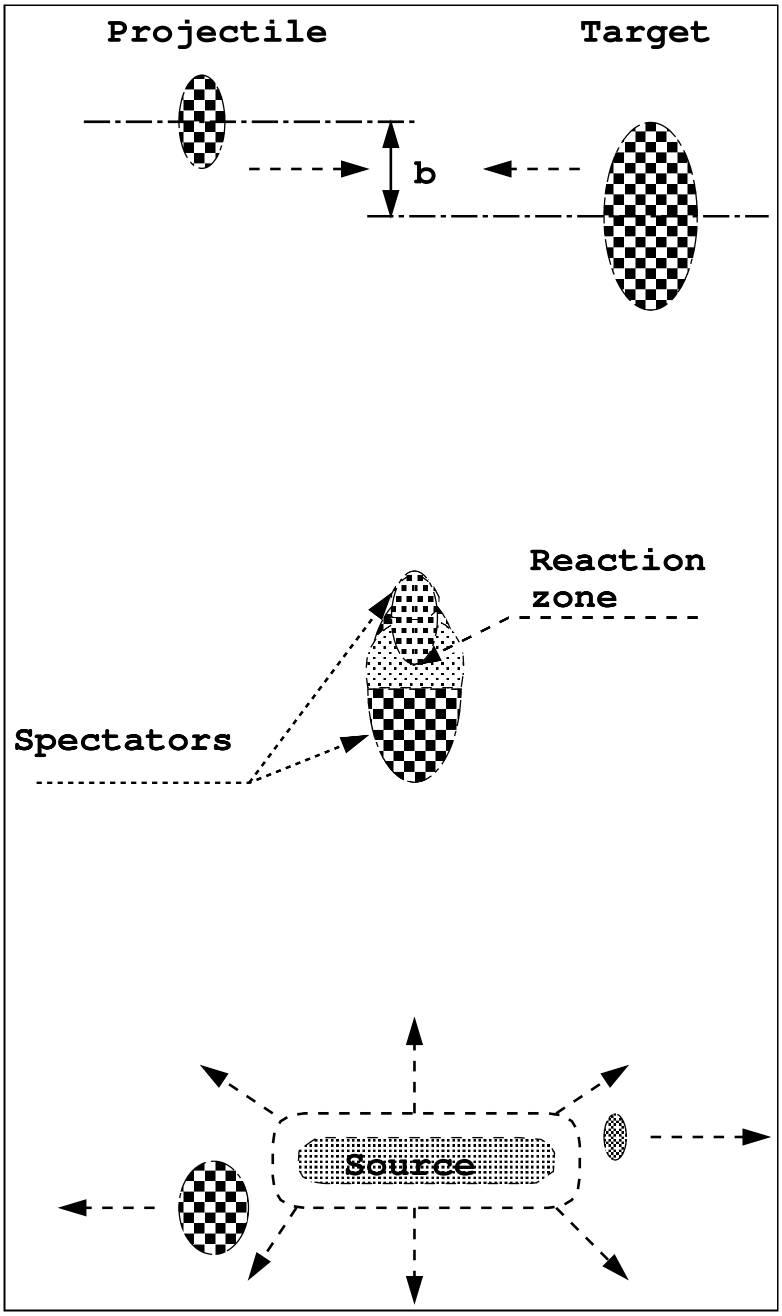

Figure 1.2: Artist's view of a heavy-ion collision

and can be estimated by studying hadron production at mid-rapidity. A review of the experimental program will be presented later; for now we note that such measurements have been performed at the BNL Alternating Gradient Synchrotron (AGS) and the CERN Super Proton Synchrotron (SPS). At the AGS, Si+Pb and Si+Al collisions were studied [7, 8] at 14.6 GeV per nucleon[2], and at CERN, S+Au and S+S at 200 GeV per nucleon[3] [9, 10]. The data indicate that there is a significant amount of stopping in either case.

At lower collision energies (e.g. AGS) the participants lose most of their energy through multiple inelastic scattering off other participants and the parts of the projectile and the target that are involved in the reaction come to a virtual stop in the nucleon-nucleon c.m.s. This results in high energy and baryon density in the reaction volume. At the SPS energies that are of interest in the present study, the picture is somewhat different. The severely Lorentz-contracted nuclei ("pancakes") lose part of their respective energies in the process of the collision, leaving in their wake a region of the highly excited QCD field, with lower concentration of baryons.

In this picture of a heavy-ion collision, the volume of the reaction zone plays an important role in determining the observables. The bigger it is, the more energy becomes available for particle production in the central rapidity region [5] (an equivalent statement: less energy is carried away by the spectators). Moreover, as

[2]more recently, Au+Au data became available

[3]in 1994, experimentation started with Pb beams

we already discussed, a large system volume is necessary to justify the thermodynamic approach. This, in particular, is one of the motivations to experiment with *heavy* ions – the current experimental programs at the AGS and the SPS involve Au+Au and Pb+Pb collisions, respectively.

1.2.2 Space-Time Evolution of *RHIC*

Let us now consider the space-time diagram of the collision, as shown in Fig. 1.3. The trajectories of the colliding nuclei are shown as thick lines. Soon after the collision, the energy density may be high enough to make the formation of the Quark-Gluon Plasma possible [2, 3, 11]. It is assumed that, after a certain proper time has passed, local equilibrium is achieved and laws of hydrodynamics become applicable [2]. The plasma then expands, and therefore its temperature eventually drops below the critical transition temperature T_c. At this point, hadrons start to "crystallize" out of QGP, a process in which the system goes from the large number of degrees of freedom (partons) of the QGP to the smaller number available in the hadronic phase, with a corresponding release of latent heat[4].

At this stage, the system exists in the mixed phase, where a gas of hadrons coexists with QGP. The source continues to evolve into the stage of expansion of the hadron gas, with rescattering of particles. It then expands until the so-called 'freeze-out', when interactions cease (due to the low density) and the particles can be considered in their "final state".

[4] we should note that the order of this transition is still not quite clear

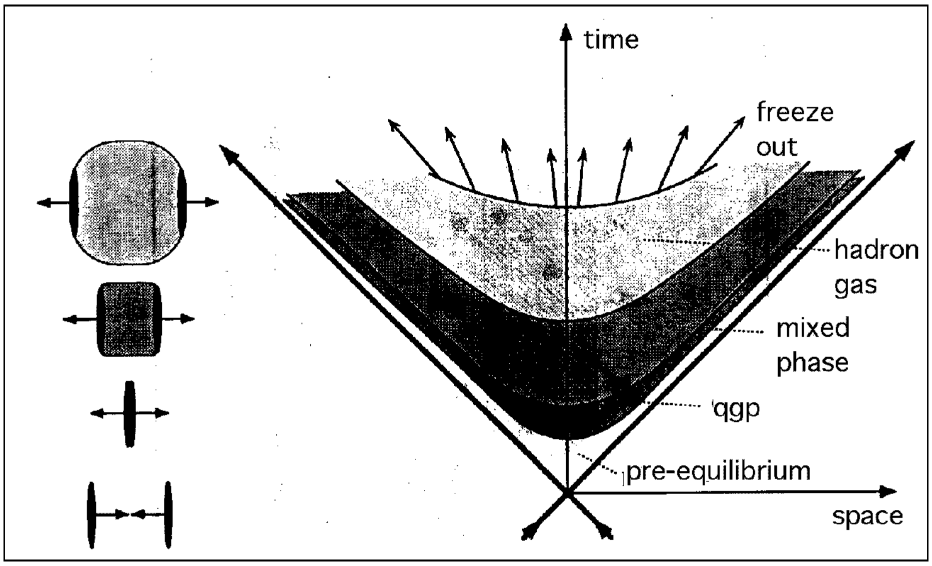

Figure 1.3: Evolution of Nuclear Matter in a Heavy-Ion Collision

1.2.3 Observables Characterizing *RHIC*

As already mentioned, the goals of a heavy-ion experiment are two-fold:

- understanding the initial conditions in the system created in the process of a nucleus-nucleus collision
- understanding its evolution, which at some point may include the QGP stage

The initial conditions, as discussed above, depend on the amount of stopping in the system[5], and can be estimated by measuring the distributions $dE_\perp/d\eta$ and $dN_{ch}/d\eta$ [3][6]. Another important variable, already mentioned, is the baryon rapidity distribution.

[5]since it determines how much energy becomes available for possible creation of QGP

[6]$E_\perp$ is usually defined as $E_\perp \equiv \sum_i E_i sin\theta_i$, where the summing is performed over all particles and θ_i is the angle between tha particle trajectory and the collision axis; N_{ch} is the charged-particle multiplicity; for definition of η, see Appendix A

Based on the measured values of $dE_\perp/d\eta$ (or $dE_\perp/dy$) one may apply Bjorken's formula [12, 3, 6, 2] to estimate the energy density ε achieved in heavy-ion reactions[7]:

$$\varepsilon = \left(\pi R^2 \tau_0\right)^{-1} (dE_\perp/dy) \tag{1.1}$$

where πR^2 is the area of the projectile and τ_0 ("formation time") is usually chosen[8] of the order of 1 fm/c.

Let us now consider the observables that can be used to extract information about the evolution of the hot and compressed nuclear matter once it is created. In a more narrow sense, in this case one is looking for the so-called "signatures of the Quark-Gluon Plasma". These include [2, 5, 6]:

- P_T distributions
- Direct photon production
- Suppression of the J/ψ production
- Signals from Intensity Interferometry
- Fluctuations in rapidity distributions and intermittency
- Strangeness production

[7] we should note that this formula is applicable subject to a number of assumptions, such as a flat dE/dy distribution at mid-rapidity, and is derived based on the hydrodynamic model; the reader is referred to the original paper [12] for details

[8] fairly arbitrary [6, 12]

Each of these signals contains extremely rich physics and their complete review is beyond the scope of present discussion. One of them, however – **Intensity Interferometry** – is of direct relevance to the topic of this thesis.

Intensity interferometry is a technique based on the fact that particles emitted from a source, due to their statistical properties and/or interaction with each other, exhibit correlated behavior. This behavior can be revealed and treated quantitatively if one introduces the *Correlation Function*, which we will discuss in detail in section 2.2.1.

The physics behind this type of measurement will be described in chapter 2 in some detail; we will show that the Correlation Function can be used to extract information about the "geometry", or space-time configuration, of the particle source resulting from a heavy-ion collision and in some cases about the dynamics of the source [2, 13, 14].

Studying correlations in pairs of different particles ($\pi\pi, KK, pp$ and even non-identical particles [13]) and with different projectile-target combinations, as well as the dependence of such correlations on various kinematic variables, can provide a wealth of information about the spatial extent, lifetime and dynamics of the system [15][9]. In simplest cases, one is trying to determine the so-called "source radius" [16].

[9]we will explain later why such "extraction" of the source parameters is equivalent to the introduction of a source model

1.3 Experiments with Heavy Ions

1.3.1 Overview

The systematic study of *RHIC* began in 1974, with the advent of the Berkeley Bevalac, with beams of up to 2.1 GeV/A and projectiles with up to A=57 (after the upgrade in 1982). Experiments at the Bevalac were aimed at the exploration of general features of nucleus–nucleus collisions. The possibility to conduct experiments with hot and dense nuclear matter spurred hopes to determine the nuclear equation of state, and even though this then proved unattainable, the results of these studies helped to shape the field.

The Alternating Gradient Synchrotron at Brookhaven National Laboratory was transformed into a heavy ion accelerator in 1986 and, since then, a rich experimental program has been pursued, first with ^{28}Si beams, and starting in 1992 with ^{197}Au. Extensive data have been collected on single and multi-particle production.

At CERN (Geneva, Switzerland) the Super Proton Synchrotron began accelerating ^{16}O at 60 and 200 GeV/A in 1986 and ^{32}S in 1987. Starting in 1990, a long-term program of heavy ion physics was established, with six principal experiments[10] (and a large number of smaller ones) and with up to 8 weeks of ^{32}S beam each year. In 1994, the SPS was further upgraded to accelerate ^{208}Pb ions at 158 GeV/A, in order to provide a significant increase in the volume and

[10] NA34, NA35, NA36, NA38, WA80 and WA85

lifetime of the reaction zone, and potentially, a higher energy density. First results from the lead beams at CERN were presented at the Quark Matter 95 Conference, and now experimental physics of high-energy ^{208}Pb+^{208}Pb collisions enters its third year.

In the initial part of the experimental program, global features of nuclear collisions were studied, such as distributions of $E_\perp$ and multiplicity, with a wide variety of projectile-target combinations and at different bombarding energies. It was established that these data are consistent with the geometrical picture of a heavy-ion collision that we discussed above and reflect the probability distribution of the number of nucleon–nucleon interactions in the overlapping region of the two nuclei.

Measurements of the baryon rapidity distributions have been performed at the AGS and the SPS [7, 8, 9, 10], at about 2.5 GeV/A and 10 GeV/A in nucleon-nucleon c.m.s., respectively. As already mentioned, the data indicate a significant amount of stopping at both energies. In particular, at AGS the highest baryon densities of roughly $10\rho_0$ are attained [6].

Application of Bjorken's formula (eq. 1.1) for S+Au collisions measured at CERN yields ε=2–3 GeV/fm^3.

The conclusion made on the basis of these measurements is that the energy densities[11] achieved in nuclear collisions studied at the AGS and the SPS are large and an order of magnitude higher than in ground-state nuclear matter, verifying

[11]and, in case of the AGS, the baryon density

that it is likely that conditions necessary for the formation of QGP have indeed been created in the laboratory.

Observation of the signatures of the QGP itself (see section 1.2.3) is, of course, the prime goal of most heavy-ion experiments. In the 1990's, a vast amount of data has been collected and analyzed at both AGS and SPS in search of the "anomalous phenomena" [6]. Identifying the signatures of the QGP in the data is an extremely difficult task. As noted in [3],

> `Because the created system is not static but rather rapidly evolving, experimental observables will, in general, correspond to an integral over the complete space-time history of the reaction until freeze-out, and disentangling the various contributions to a signal from the different phases ... presents indeed a formidable challenge.`

Up to date there has been no unambiguous evidence of the existence of QGP. At the same time, a number of physics observables are not readily reconciled with the predictions of the existing dynamical models [5, 6][12].

1.3.2 The Role of Intensity Interferometry

Probing the space-time characteristics of the expanding system provides an important test of various scenarios of the heavy-ion collisions. Knowledge of the size

[12]an example quoted in [6] is the strangeness production, especially strange antibaryon yields

and shape of the system at freeze-out provides important input for models. It is even possible to observe, via particle correlations, such dynamical phenomena as radial expansion [15, 14, 17].

Different particle species can be used in correlation measurements, providing complementary information about the collision. Pions were historically the first to be used for that purpose (partly due to their abundance). Positive kaons have significantly lower cross-section of interaction with nuclear matter and therefore escape the reaction zone with less rescattering, carrying information about earlier stages of the collision. Protons allow a correlation measurement of the reaction volume at freeze-out.

A review of the current status of intensity interferometry measurements can be found in [15]. Most recently such measurements have been performed in experiments E859/E866 and E814 at the AGS and NA44, NA35 and WA80 at CERN. We refer the reader to chapter 2 for an introduction to concepts and techniques that allow one, in some cases, to estimate the "source size", i.e. the spatial extent of the region of particle emission. Keeping in mind that direct comparison of the "source radii" as measured in different experiments carries a large degree of systematic uncertainty, there are still some general conclusions about the trends in the data. For example, the source size measured with kaon pairs appears to be consistently smaller than the pion source[13]. In all cases the source appears to be larger than the projectile – a phenomenon non-trivial in itself. It is certain that

[13] as should be expected since the cross-section of scattering is smaller for K than for π

the system created in relativistic heavy-ion collisions is, indeed, large.

With the advent of sophisticated event generators[14] experimentalists have a new opportunity to assess the collision dynamics, by making detailed comparisons of the data and theory. This, of course, is relevant not only for correlation studies but for virtually any aspect of heavy-ion physics. It represents one step beyond the standard source size estimation techniques[15] and allows one to consider the effects of particle production, hadron rescattering and resonance formation and decay.

In particular, we can hope to "provide another check for any theoretical scenario that might be proposed to accurately describe an ultrarelativistic heavy-ion collision" [11].

1.4 Proton Correlation Measurements

Proton correlation measurements have been used to investigate nuclear reactions in many experiments at intermediate and high energies [18, 19, 20]. Perhaps the most popular technique used to extract "source sizes" has been to fit the data with a theoretical calculation based on a Gaussian source model, assuming vanishing emission time[16], as suggested by Koonin [21]. Experimental effects, such as the finite momentum resolution and acceptance are usually taken into account by introducing the corresponding factors into the calculation. As a result, one is able

[14] see [3] for an overview

[15] we will see that such techniques involve some kind of source parametrization, meaning that in fact a primitive model of the source is used

[16] this assumption, in many cases, is essentially a rather crude approximation

to estimate the "source radius" in the Gaussian or hard sphere approximation.

The first measurement of two-proton correlation functions in intermediate-energy heavy-ion collisions, performed by Lynch *et al* in 1983, provided evidence of particle emission from localized regions of high excitation. The reaction studied was $^{16}O+^{197}Au$ at an incident ion energy of 400 MeV. The proton correlation data, analyzed in different momentum bins, indicated that protons of higher momentum are emitted by a localized source ("hot spot"), whereas slow protons appeared to be coming from a source comparable or larger in size than the compound nucleus.

Since then, a large number of experiments have been performed by different groups at incident energies of 10–100 MeV per nucleon and a variety of projectile-target combinations (see [13] for an overview).

Measurements with a neon projectile on different targets at bombarding energies 400 and 800 MeV per nucleon have been performed by Dupieux *et al* [22]. The investigators found a dependence of the apparent proton source size on the event multiplicity and projectile energy, suggesting increasing compressibility of nuclear matter at the higher bombarding energy.

The reactions Ca+Ca and Nb+Nb at 400 MeV per nucleon were studied by the Plastic Ball collaboration at the Bevalac [23]. The source sizes were found to depend on the event multiplicity, and the dependence was explained in terms of the varying number of nucleons participating in the reaction.

There have been significantly fewer measurements with proton pairs at ultrarelativistic energies. At the AGS, there exist analyzed data from the E802/E859 and E814/E877 collaborations. As reported by the E802/E859 group [24, 25, 19], a dependence of the "source radius" on the target mass was found; in particular, in the reaction Si+Au $\rightarrow 2p+$X the radius is found to be significantly bigger than that of the ^{28}Si nucleus [24].

The analysis of two-proton correlations in E814/E877 is still under way and now includes new data from Au+Au collisions [26]. Its focus is on detailed comparison to event generators such as `RQMD`[17]. Preliminary results indicate a fair degree of consistency between the data and `RQMD`.

Interesting results on two-proton correlations in the target fragmentation region, at beam energies of 200 GeV/A, have been obtained by the WA80 collaboration at CERN. The following reactions were studied

- p and ^{16}O projectiles with C, Cu, Ag and Au targets
- ^{32}S with Al and Au target

The protons were measured by the Plastic Ball detector that had been previously used at the Bevalac [23] and provided the pseudorapidity coverage $-1.7 < \eta < 1.3$. The results of the source radii measurements were interpreted as an indication of emission taking place from the whole volume of the excited target nucleus.

There have been no reports on two-proton correlation measurements at CERN energies in the central rapidity region. Thus, this thesis presents the first ever

[17] this particular model will be discussed in detail in chapter 5

analysis of data of this kind.

1.5 Thesis Objective

The objective of this thesis is to apply the method of Intensity Interferometry to the study of proton pairs with low relative momentum produced in ultrarelativistic S+Pb and p+Pb collisions, in order to assess the space-time characteristics of the particle source resulting from such collisions.

Our approach will be to present and analyze the experimental data in comparison with the `RQMD` model[18], that has been used earlier in the NA44 investigation of two-pion and two-kaon correlations [30, 31, 15]. As we will see, certain conclusions can be drawn from such comparison about the size and dynamic characteristics of the particle source. In this respect the two-proton measurement is one that complements earlier studies of the correlation signals in NA44 and provides additional information about the particle source produced in ultrarelativistic heavy-ion and proton-nucleus collisions.

We will show that there are important factors, due to the effects of the trigger bias, apparatus resolution and acceptance as well as background events, that need to be taken into account when making comparisons of the theory to data. One of the goals achieved in the process of this research is the creation of a sophisticated Monte Carlo scheme which allows the inclusion of all these factors in a realistic manner when calculating the correlation function based on the event

[18] [27, 28, 29] and references therein

generator predictions. We will provide a rather complete analysis of the systematic uncertainties in the data and in the Monte Carlo.

1.6 Organization of this thesis

In this Introduction, we have presented the background material. We will proceed to a review of the physics of two–proton correlations (Chapter 2), with references to Intensity Interferometry of identical bosons, widely known as HBT measurements. The experimental apparatus and related issues are discussed in Chapter 3, with details of the detector design, hardware and data-taking conditions.

Chapter 4 presents an overview of the detector calibration and details of the data reduction and other analysis procedures, leading to the construction of the correlation function. A description of the track reconstruction in NA44 and its performance can be found there. We discuss important details of the Particle Identification scheme and its implications for the Monte Carlo. The stability of the proton pair data with respect to various cuts used during the data reduction is also discussed.

The structure of the Monte Carlo (MC) calculations, rather crucial for interpretation of the data and comparison with models, is explained in Chapter 5. We start with characteristics of the particle source predicted by the `RQMD` model, and proceed to a detailed explanation of various components of the MC chain that include simulation of the apparatus and tracking system, estimation of the event centrality and analysis of the effect of background on the result. We then study the systematic uncertainty of all components of the Monte Carlo system.

In Chapter 6 we compare the results from the Monte Carlo with the experimental data, paying attention to the role of the systematic uncertainty. Chapter 7 summarizes the important points of the data analysis and the Monte Carlo and attempts to draw conclusions from their comparison.

There are several appendices, which present details and explanations which would otherwise interfere with the flow of the text.

Terms related to computers and software are typeset in the typewriter font (for example, `UNIX`). All trademarks mentioned are recognized as such. This document was typeset using LaTeX.

Chapter 2

Intensity Interferometry of Proton Pairs

2.1 Intensity Interferometry

Intensity interferometry is a technique based on the fact that particles emitted from a source, due to their statistical properties and/or interaction with each other, exhibit correlated behavior. The study of such correlations can be used to extract characteristics, such as the spatial extent, of the particle-emitting region. A comprehensive review of particle interferometry can be found in [13]. Features of correlations in the system of two protons are described in an important paper by Koonin [21], among others. Here we provide a brief (and rather standard) qualitative outline of the subject, following [13] and [32].

Consider two identical particles leaving the source (Fig. 2.1) at points α and β, and suppose that the wave function of each particle is a plane wave, $\psi(\mathbf{r}) \sim exp(i\mathbf{pr})$. Let us assume now that the source is characterized by random phase factors with a magnitude corresponding to the strength of the source; the

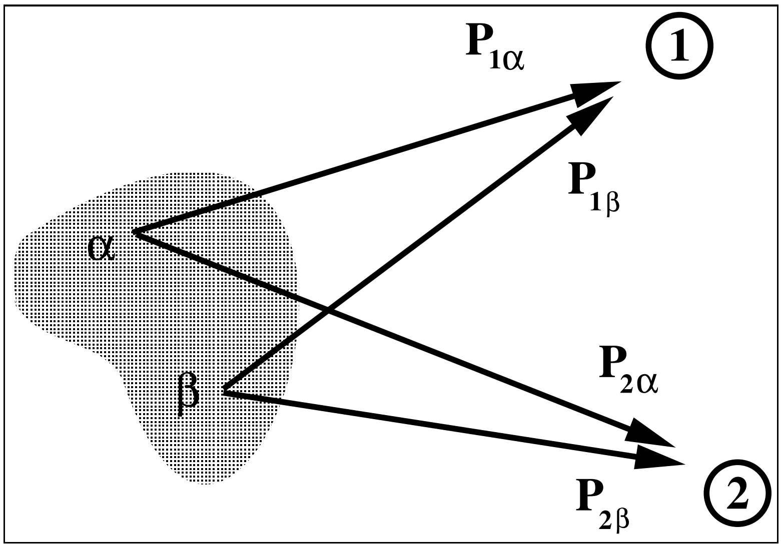

Figure 2.1: Schematic representation of the emission of two indistinguishable particles from two points (α and β) on a source. The particles are observed at points 1 and 2

randomness of phase means we are considering an *incoherent* particle source. The joint amplitude of the process, for two emission points and two detectors, takes the form

$$A(1,2) = \langle \mathbf{p}_1, \mathbf{p}_2 | \mathbf{r}_\alpha, \mathbf{r}_\beta \rangle = \frac{1}{\sqrt{2}} \left[e^{-i\mathbf{p}_1\mathbf{r}_\alpha} e^{-i\mathbf{p}_2\mathbf{r}_\beta} \pm e^{-i\mathbf{p}_1\mathbf{r}_\beta} e^{-i\mathbf{p}_2\mathbf{r}_\alpha} \right] \tag{2.1}$$

where the $\pm$ sign reflects the particles' statistics: "+" for bosons and "$-$" for fermions.

Integrating over the source, we find the corresponding probability of observation

$$\langle P(1,2) \rangle = \int d^3\mathbf{r}_\alpha d^3\mathbf{r}_\beta A(1,2) A^*(1,2) \rho(\mathbf{r}_\alpha) \rho(\mathbf{r}_\beta) \tag{2.2}$$

where $\rho(\mathbf{r})$ is essentially the source density. Substituting $A(1,2)$, it is easy to obtain

$$\langle P(1,2)\rangle = 1 \pm |\tilde{\rho}(\mathbf{p}_1 - \mathbf{p}_2)|^2 \tag{2.3}$$

where $\tilde{\rho}$ is the Fourier transform of $\rho(\mathbf{r})$. In the above derivation we assumed an *incoherent* emission of particles (see [13] for a discussion of coherent vs incoherent particle production).

We may now look at the above arguments from the point of view of the uncertainty principle. If sites of emission, or, to be more precise, final scatterings of the two particles are separated by distance r, there will be correlation or anti-correlation between them over a range of relative momenta

$$\Delta p \approx \hbar / r \tag{2.4}$$

depending on whether wave function of the system is symmetric or antisymmetric. In the case we are interested in, i.e. that of two protons, one must take into account the spin degree of freedom. Thus, the final state of the pair is described by a superposition of singlet and triplet wave functions, the former being symmetric and the latter antisymmetric. The net result is a depletion in the probability of finding two protons close to each other in phase space. In a system of identical bosons, e.g. $\pi\pi$, such probability, on the contrary, is enhanced. In either case, the correlator defined in eq. 2.3 deviates from its (asymptotic) value of 1 when $|\mathbf{p}_1 - \mathbf{p}_2| \sim \hbar / r$.

2.2 Correlation Function: the Definition

2.2.1 The Definition

In order to quantify correlation phenomena, it is customary to define a correlation function in the following way

$$C(\mathbf{p}_1, \mathbf{p}_2) = A \frac{R(\mathbf{p}_1, \mathbf{p}_2)}{B(\mathbf{p}_1, \mathbf{p}_2)}, \tag{2.5}$$

where $\mathbf{p}_{1,2}$ are the particles' 3-momenta. $R(\mathbf{p}_1, \mathbf{p}_2)$, the 'real distribution', is essentially the density of events in the phase space of the two particles. The denominator $B(\mathbf{p}_1, \mathbf{p}_2)$, often referred to as 'background distribution', is constructed in a way such that all correlations are removed. "A" is a normalization constant and will be discussed later. Deviation of this ratio from constant at some values of the momenta indicates the presence of correlations due to statistical phenomena and/or final interactions.

2.2.2 The Choice of the Momentum Variable

It is difficult to visualize and interpret a function of six variables; also, collecting enough experimental events to provide sufficient statistics in six-dimensional bins may be a problem. Therefore, the form 2.5 is often projected on a smaller number of dimensions and presented in terms of some convenient variables, whose choice depends on the particle source parameters that need to be extracted.

To clarify this, let us consider, briefly, examples from the boson interferometry studies, where the particle-emitting source is often approximated by means of Gaussian density distribution[1]. It follows from the known property of the Fourier transform that a Gaussian form for $\rho(\mathbf{r})$ will lead to a Gaussian shape of $\tilde{\rho}$ (eq. 2.3). For this reason, *fitting the data with a Gaussian form* allows one to extract "the radius" of the source; in many correlation studies [24, 33], the following parametrization has been used[2]:

$$\rho source \sim exp\left(-\frac{r^2}{2R^2}\right) \tag{2.6}$$

$$C(Q_{inv}) \sim 1 + \lambda exp(-Q_{inv}^2 R^2) \tag{2.7}$$

where

$$Q_{inv} = \sqrt{-\Delta p^\mu \Delta p_\mu} \tag{2.8}$$

$$\Delta p^\mu = p_1^\mu - p_2^\mu$$

where $p_{1,2}^\mu$ are 4-momenta of the particles that constitute the pair. Hence, we may say that eq. 2.5 was effectively projected on the one-dimensional variable Q_{inv}.

We note that, as can be seen in eq. 2.3, the Fourier transform for each component of $\mathbf{p}_1 - \mathbf{p}_2$ can be carried out independently; in [15] the following form of the Gaussian fit is suggested

$$C(\mathbf{q}) \sim 1 + \lambda exp\left\{-q_{t_O}^2 R_{t_O}^2 - q_{t_s}^2 R_{t_s}^2 - q_l^2 R_l^2\right\} \tag{2.9}$$

where q is defined as the relative momentum vector. This fit allows one to extract information about the source size in three dimensions[3]. Therefore, in this case

[1] later we will discuss the validity of such approximation and its applicability to the present study

[2] λ is the so-called chaoticity parameter – see [13, 34, 15]

[3] fitting techniques are undoubtedly the most widely used tool in boson interferometry

eq. 2.5 was projected on the three-dimensional space of variables q_{t_O}, q_{t_s} and q_l (see [15, 34] for details of the definition of these variables).

In our proton correlation study, we use the kinematic variable

$$q_{inv} = \frac{1}{2}\sqrt{-\Delta p^{\mu}\Delta p_{\mu}} \tag{2.10}$$

In fact, $q_{inv} = \frac{1}{2}Q_{inv}$, the latter being the variable popular in one-dimensional boson interferometry[4] (eq. 2.8). Also, q_{inv} has the following property: in the center-of-mass system of the pair, $|\mathbf{p}_1| = |\mathbf{p}_2| = q_{inv}$.

We chose q_{inv} because it was used in previous *pp*-correlation studies, both experimental and theoretical, by other groups and as such makes notation and comparisons easier. It is understood that by studying correlations in just one dimension, we can't get information about *the shape* of the source in 3D, but can only estimate its volume [19, 25, 14]. The discussion of this issue is deferred until section 2.3, where the final state interactions in the system of two protons will be considered.

2.2.3 The Shape of $C(q_{inv})$ without the Final State Interactions

In the literature, the correlation function defined above is often denoted as C_2. We will follow [14] and drop the index "2", referring to the correlation function as $C(q_{inv})$ or $C(Q_{inv})$. Let us rewrite eq-s. 2.5 and 2.3 as

$$C(q_{inv}) = A\frac{R(q_{inv})}{B(q_{inv})} \tag{2.11}$$

[4] in the center-of-mass system of the pair, $Q_{inv} = |\mathbf{p}_1 - \mathbf{p}_2|$, i.e. it is equal to the relative momentum of the two particles

$$C(q_{inv}) = 1 \pm \tilde{\rho}(q_{inv}) \tag{2.12}$$

respectively. There is a plus or minus sign depending on symmetrization/antisymmetrization requirement on the final state. For example, in case of two pions, there should be a plus sign. A system of two protons, as we already mentioned, is described by a combination of singlet and triplet wave functions (due to the spin degree of freedom): $^1\Psi$ and $^3\Psi$, the former being symmetric and the latter antisymmetric, and may be symbolically represented as $\uparrow\downarrow$ and $\uparrow\uparrow$.

Hence, to calculate $C(q_{inv})$ at q_{inv}=0 (the intercept), the last term[5] in equation 2.12 should be written as a weighted sum:

$$(-1) \times \frac{3}{4} + (+1) \times \frac{1}{4} = -0.5$$

where $\frac{3}{4}$ is the weight for the triplet state and $\frac{1}{4}$ for the singlet. Therefore, in the two-proton system C(0)=0.5. The corresponding conceptual shape of the correlation function, for both boson and spin $\frac{1}{2}$ fermion cases (for example, $\pi\pi$ and pp pairs) is presented in Fig. 2.2. We emphasize that the final state interactions haven't been considered yet.

2.2.4 Constructing the Correlation Function

To construct the correlation function according to the definition presented above, we proceed in the following manner: we form the 'real distribution' $R(q_{inv})$ – the q_{inv} spectrum of the detected proton pairs, whereas the 'background distribution'

[5] assuming parametrization similar to eq. 2.7

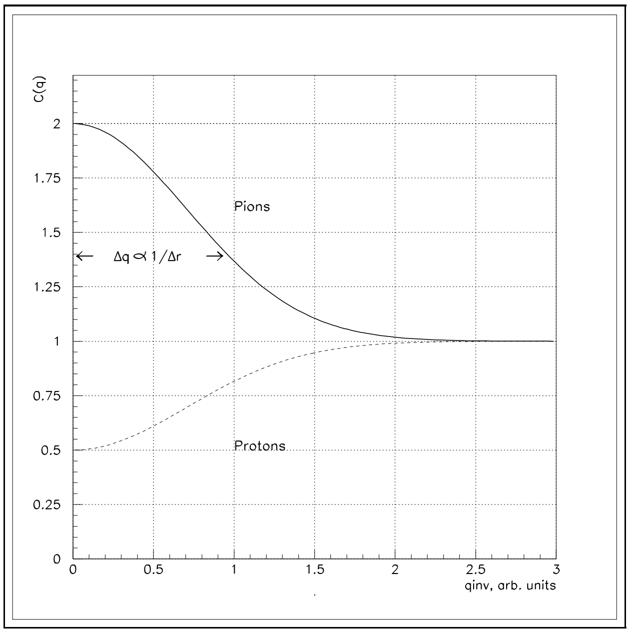

Figure 2.2: Conceptual shape of the proton and pion correlation functions, due to statistics only.

$B(q_{inv})$ is constructed using the standard event mixing technique [13, 16, 25, 14, 35], with pairs formed by randomly sampling a list of registered particles, from different events, with their corresponding momenta. Ideally, pairs thus formed should not have any correlations due to their interactions or statistical nature and simply represent the available phase space in terms of the variable q_{inv}.

The ratio $\frac{R}{B}$ is then multiplied by the normalization factor A (eq.2.11), that is often chosen such that, asymptotically, $C(q_{inv}) \equiv 1.0$. However, we chose a slightly different normalization, whereby R and B are normalized *to the same number of events*, since

- as we will see, the NA44 acceptance in q_{inv} is relatively narrow, making the asymptotic approach somewhat ambiguous

- it is very easy to implement and it does not need to be modified in case we need to change the binning of the R and B distributions

- since, as we will see, the objective of our study is comparison of the data and a model, we just need to provide a consistent normalization in both data and theory

Finally, we note that under the proposed normalization the asymptotic value of $C(q_{inv})$ is usually close to 1 anyway.

2.3 Final State Interactions

A very important aspect of two-particle correlations is the presence of final state interactions (f.s.i.). Given the spatial and energy scales of the phenomena involved, both Coulomb and strong interaction effects should be taken into account.

Common for pairs of charged bosons and fermions is the **Coulomb** effect: as two same-sign particles with similar momenta follow their trajectories, they repel each other. This leads, in the case of both bosons and fermions, to *suppression of the two-particle probability* in the region of low relative momentum. This effect is routinely taken into account in interferometry studies with pions and kaons, whereby *data are corrected* by the so-called "Gamow factor"

$$G_0 = \frac{2\pi\eta}{exp(2\pi\eta) - 1}, \text{ where } \eta = \frac{me^2}{2\hbar q} \qquad (2.13)$$

and m is the mass of the particle. It is worth mentioning that the above factor has a rather strong dependence on the particle mass, and therefore the effect is more significant for protons than it is for pions. Because of the importance of the Coulomb effect for our study of two-proton correlations, we review the Coulomb wave function and the origin of the Gamow factor, in detail, in Appendix B. In particular, this factor is essentially the square of the Coulomb wave function $|\psi_c(0)|^2$ calculated at the origin, hence, strictly speaking, it is only applicable when both particles are emitted from the same point, i.e. from a point source – an unrealistic situation. As will be discussed later, the Coulomb effect is included in our calculation in a more consistent manner, via integration of the Coulomb wave functions.

Whereas the **strong interaction** in $\pi\pi$ and KK systems of the same sign is usually ignored [36, 37, 16], that is definitely not the case with proton pairs. The proton-proton system features a short-range attractive interaction[6] (often approximated by the Reid soft core potential, [38], see Fig. 2.3), which leads to an enhancement in the $l = 0$ scattering channel (s-wave) at $q_{inv} \approx 20$ MeV. As stated in [21], the magnitude of such an enhancement

> `scales as` $(a/r)^3$`, i.e. proportional to the fractional volume of the system within the range` a `of the nuclear force from a given point`

[6]which becomes repulsive at very small distances

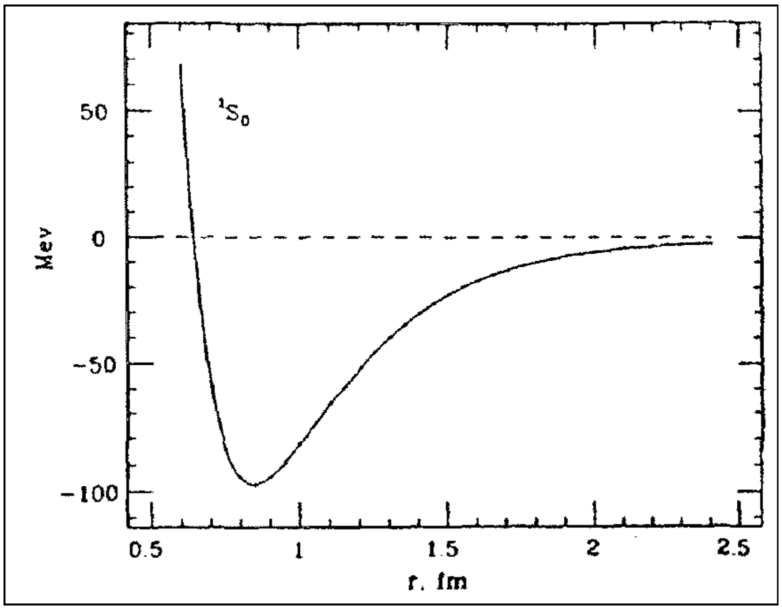

Figure 2.3: The $^1S_0$ Reid soft core potential

A similar result is obtained in [25], where it is derived based on an expression for the density of states in a system of non-interacting fermions in a spherical box of the volume $V = \frac{4}{3}\pi r^3$. The corresponding change in the correlation function is written

$$\Delta C(q_{inv}) = \frac{3}{2}\frac{\hbar^2}{r^3 q_{inv}^2}\frac{d\delta_0}{dq_{inv}} \tag{2.14}$$

where δ_0 represents the phase shift of the s-wave[7].

Numerical calculations [21, 25] confirm that the attractive interaction in the *pp* system is the dominant factor defining the shape of the correlation function; this, in turn, means that the correlation function *contains no directional information about the source* (because of the isotropy of the s-wave) and is only sensitive

[7]thus the enhancement is actually defined by the rapid change of the phase of the $s = 0$ partial wave

to the volume of the source. This effectively justifies using a one-dimensional expression for the correlation function and eliminates the need to consider individual components of the relative momentum vector.

Combination of the Coulomb and strong interactions leads to the following features of the proton correlation function:

- due to Coulomb repulsion between the two protons, the correlation functions has a dip at very low q_{inv} that goes all the way to zero
- the dip is immediately followed by a peak at about 20 MeV in q_{inv} that is due to strong interaction

A conceptual "ideal" proton correlation function is presented in Fig. 2.4. It is

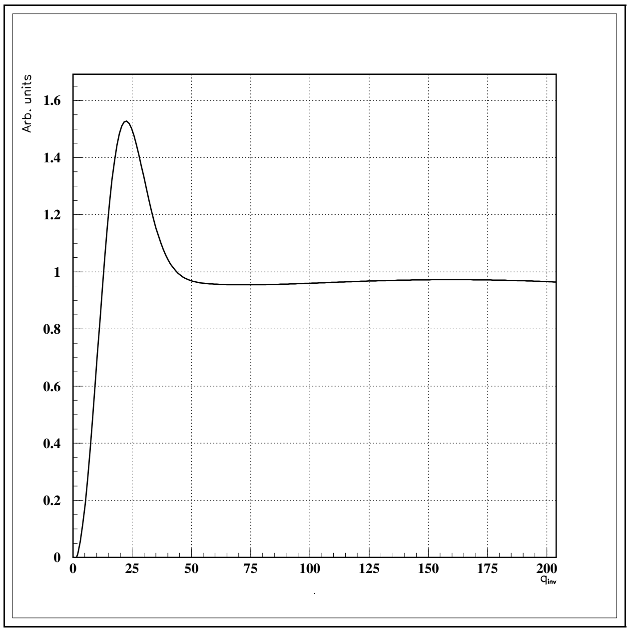

Figure 2.4: Conceptual shape of the proton correlation function.

mainly shaped by the f.s.i. and to somewhat lesser extent by statistical behavior of the particles involved, as opposed to $\pi\pi$ and KK systems which present a "cleaner" case of two-particle interferometry. However, it may be actually considered a bonus[8]: since, as explained above, the amplitude of the peak depends on the probability of finding two protons within the effective range of strong interaction and, and, in general, goes as $\sim r^{-3}$, it is rather sensitive to the spatial characteristics of the emitting source. In general, a source of protons that is more localized yields a curve with a *sharper peak*, and, reciprocally, a source that is more diffuse would be characterized by a *flatter* correlation function.

In principle, one should also address the issue of interaction, in the final state, of the proton pair with the particle source as a whole[9]. We note that by definition we consider a pair to be in the *final state* after the last rescattering due to strong interaction takes place[10], therefore, the interaction of the pair with the rest of the source is essentially Coulomb. It is argued [14, 35] that the change of momentum of each particle in the pair due to the Coulomb force is practically the same, for particles of the same charge and small relative momenta. A quantum-mechanical analysis of this problem, developed in [39], shows that, indeed, for identical particles this effect can be safely neglected[11].

---

[8] as stated in [21], "Instead of obscuring the effect however, these interactions enhance the sensitivity of the proton technique... "

[9] often referred to as "residual" or "remaining" nuclear matter

[10] the issue of the hadronic mean field is discussed in [14] and references therein

[11] whereas it can be used to assess temporal evolution of the particle source through the measurement of particles with different charge, such as np pairs

2.4 Calculation of the Correlation Function

2.4.1 Analysis of the Two-Particle Emission

The ultimate (and rather ambitious) goal of a correlation measurement is determination of the space-time characteristics of the particle source. In a more narrow sense, in order to make use of such a measurement, *one must be able to make a connection between the parameters of the source and the correlation function.* In our case this, clearly, involves calculating $C(q_{inv})$ based on a source model. In the "ideal" case, i.e. in the absence of the f.s.i., the equation 2.12 should be sufficient for that purpose.

However, in view of the f.s.i. problem that we just discussed, we need to improve on our naïve, Fourier transform representation of the correlation function and include the final state interactions.

To get some insight into the problem, let us first consider the argument in [21, 13]. In the context of nonrelativistic quantum mechanics, consider $D(\vec{r}t, \vec{p})$, the space-time distribution of final proton scatterings during a heavy-ion collision. The joint probability of observing protons with momenta $\mathbf{p}_1$, $\mathbf{p}_2$ is given by the square of the overlap between the single-particle wave packets and the final state wave function; the double differential two-proton inclusive cross-section may then be approximated as

$$\frac{1}{\sigma}\frac{d\sigma}{d\mathbf{p}_1 d\mathbf{p}_1} = \int\limits_{-\infty}^{+\infty} dt_1 dt_2 \int d\mathbf{r}_1 d\mathbf{r}_2 D(\mathbf{r}_1 t_1, \mathbf{p}) D(\mathbf{r}_2 t_2, \mathbf{p}) \times \left\{ \frac{1}{4} |^1\Psi_{\mathbf{p}_1\mathbf{p}_2}|^2 + \frac{3}{4} |^3\Psi_{\mathbf{p}_1\mathbf{p}_2}|^2 \right\} \tag{2.15}$$

where, again, $^1\Psi$ and $^3\Psi$ are singlet and triplet pp scattering wave functions, that are respectively symmetric and antisymmetric under interchange of their spatial or momentum arguments. These wave functions satisfy the two-body pp Schrödinger equation containing both nuclear and Coulomb potential (and that is exactly how the f.s.i. are taken into account). In [21], Koonin further proceeds to introduce a Gaussian parametrization of the proton source and calculates the correlation function for that parametrization.

A detailed justification of this approach and analysis of the approximations involved is presented in [14]. Here we will briefly summarize the most relevant arguments from this paper. The two-particle emission is first described in the most general way by the two particle $\mathcal{T}$-matrix:

$$P_2(\mathbf{p}_1, \mathbf{p}_2) = \sum_f \left| \int d^4x_1 d^4x_2 \mathcal{T}_f(x_1, x_2) U(x_1, x_2; p_1, p_2) \right|^2 \tag{2.16}$$

where U is the evolution matrix. Assuming incoherent particle production (chaotic source), the $\mathcal{T}$-matrix factorizes

$$\mathcal{T}_f(x_1, x_2) \approx \mathcal{T}_{f_1}(x_1) \mathcal{T}_{f_2}(x_2) \tag{2.17}$$

After performing Wigner decomposition of $\mathcal{T}$-matrices and the evolution operator

U, and some Fourier transforms, equation 2.16 can be rewritten

$$P_2(\mathbf{p}_1,\mathbf{p}_2) = \int d^4q d^4x_1 d^4x_2 S(x_1, \frac{m_1 K}{m_1+m_2} + q) S(x_2, \frac{m_b K}{m_1+m_2} - q) W_{\mathbf{k}}(q, x_2 - x_1) \tag{2.18}$$

where $K = p_1 + p_2$ and $W_{\mathbf{k}}$ is the Wigner decomposition of the outgoing state with relative momentum $\mathbf{k}$ and $S(x,p)$ is essentially the source function[12].

It is further argued in [14] that q-dependence in equation 2.18 can be safely neglected[13] and one thus obtains

$$P_2(\mathbf{p}_1,\mathbf{p}_2) = \int d^4x_1 d^4x_2 S(x_1,p_1) S(x_2,p_2) \left|\phi_{\mathbf{k}}(\mathbf{x}_2 - \mathbf{x}_1 - \mathbf{v}_{12}(t_1-t_2))\right|^2 \tag{2.19}$$

where ϕ is relative wave function evaluated in the rest frame of the pair and $\mathbf{v}_{ab}$ is the velocity of the pair's center of mass. Hence, the problem of calculating correlations in the two-particle system is reduced to evaluation of the integral in eq. 2.19, based on $S(x,p)$ that is presumably known from a model, and on the outgoing two-particle wave function ϕ, which is calculated separately.

2.4.2 Prescription for the Calculation

Equation 2.19 can now be applied to generate correlation functions from models [31, 14]. The most straightforward way to evaluate the integral is to apply the Monte Carlo method (note that it only requires single-particle input, $S(x,p)$). This can be done by randomly sampling the integrand and accumulating the sum

[12] in particular, when S is evaluated on the mass shell, it yields $P_1(\mathbf{p}) = \int d^4x S(p,x)$, i.e. the single-particle probability

[13] i.e. $S(x,p)$ varies slowly in p

of its values, which will become the relative-momentum dependent two-particle probability function.

The prescription, therefore, is to use a model to create a list of emission points $(p_x, p_y, p_z, x, y, z, t)$, that effectively correspond to the particle's last interaction[14]. Then, one must randomly choose two particles from this list and evaluate the wave function squared[15]

$$w_{ij} = \left|\phi_{\mathbf{k}_{ij}}(\mathbf{r}_i - \mathbf{r}_j - \mathbf{v}_{ij}(t_j - t_i))\right|^2 \tag{2.20}$$

where labels i and j are indices of the particles chosen from the list. It is then possible to construct the two-particle probability density function simply by calculating, with sufficient statistics, and histogramming the values of w_{ij}, in terms of a convenient momentum variable (or variables). Since we define the correlation function in terms of q_{inv} (see eq. 2.11), this part of the procedure can be formally described as construction of $R(q_{inv})$ in the form of a discrete distribution. Denoting the summation in the Monte Carlo process as $\sum_{ij}$, this distribution can be written in terms of its bins' contents:

$$R_l = \sum_{ij} \delta(n_{bin}(q^{ij}_{inv}), l) w_{ij} \tag{2.21}$$

where l is the bin's number, $\delta(n, m)$ is the Kronecker delta, $n_{bin}(q)$ is a function that defines the bin number based on the value of its argument and w_{ij} is calculated according to eq. 2.20. Following the same line of argument, the "Background

[14]obviously, this list represents $S(x, p)$ in the calculation

[15]in the next section we will detail this part of the calculation

distribution" is formed according to

$$B_l = \sum_{ij} \delta(n_{bin}(q_{inv}^{ij}), l) \tag{2.22}$$

i.e. it assumes *no correlation* between the particles in the pair (as it should!).

In summary, the Monte Carlo process described by equations 2.21 and 2.22 continues until an adequate degree of accuracy of both distributions is achieved, and the correlation function is then calculated as the ratio

$$C_l = A \frac{R_l}{B_l} \tag{2.23}$$

where A is the normalization factor.

2.4.3 Two-Proton Wave Function

To calculate the wave function ϕ in eq. 2.20, we need to solve the Schrödinger equation given the interaction between the particles and also take into account the Fermi antisymmetrization. The solution of the Schrödinger equation for Coulomb wave function is briefly discussed in Appendix B. The result is

$$\phi_c(\mathbf{k}, \mathbf{r}) = e^{-\frac{1}{2}\pi\gamma} \Gamma(1 + i\gamma) e^{ikz} F\left[-i\gamma|1|ik(r - z)\right] \tag{2.24}$$

where $\gamma = e^2/\hbar v$. Since the hadronic interaction in the system of two protons is known (section 2.3), it is possible to find the corresponding corrections $\Delta\phi_l$ to partial waves

$$\phi(\mathbf{k}, \mathbf{r}) = \phi_c(\mathbf{k}, \mathbf{r}) + \sum_l i^l (2l + 1) P_l(cos\theta) \Delta\phi_l(kr) \tag{2.25}$$

For the two-proton system, only s-wave needs to be taken into account [14, 25]. It is clear that using the above expression for $\phi(\mathbf{k}, \mathbf{r})$, that takes into account the f.s.i., in equation 2.20, provides automatic inclusion of both Coulomb and strong interaction effects and makes the Gamow correction factor unnecessary.

2.4.4 Comparison of the Theoretical $C(q_{inv})$ to the Data

Distortion of $C(q_{inv})$ due to the Effects of the Measurement

In section 2.3, we demonstrated how the Final State Interactions change the shape of the proton correlation function (compare Figs. 2.2 and 2.4). However, the f.s.i.-modified curve presented in Fig. 2.4 itself is not final but will, in general, be subject to further modifications due to the effects of the measurement. More specifically, the R and B distributions considered above are affected by factors such as

- finite momentum resolution of the apparatus, typically leading to smearing out, to some extent, of the features of R and B
- distortion of B by the so-called "residual correlations in the background"

The effect of the finite momentum resolution is schematically illustrated in Fig. 2.5. It typically leads to "diffusion" of events from bins with larger statistics to adjacent bins with smaller statistics, hence the "smearing" of the q_{inv} spectra. The distribution in Fig. 2.5 is hypothetical but it does have a realistic feature – it goes to 0 at $q_{inv} = 0$ due to the phase space and Coulomb effects.

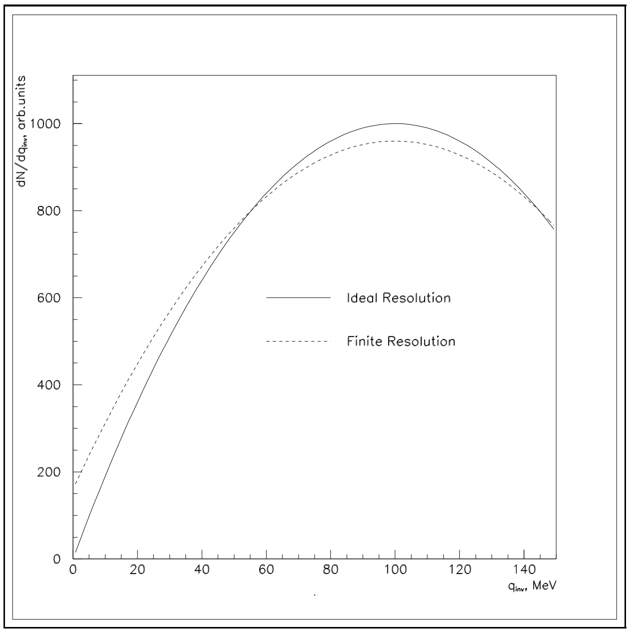

Figure 2.5: Distortion of a hypothetical q_{inv} distribution due to the finite momentum resolution

Because of the diffusion-like nature of the momentum smearing effect, bins at the lowest q_{inv} values, where the curve is the steepest, can be expected to be influenced the most. The effect is exacerbated by the fact that the statistics are the lowest in these bins. The peak in the two-proton correlation function (discussed above) will also be affected.

"Residual correlations in the background" are due to the requirement of two particles in the limited acceptance of the apparatus. For example, if there is a positive Bose-Einstein correlation, the individual particle spectra will be biased towards the center of the acceptance[16], leading to changes in the shape of B (see [40, 16, 35] for a complete treatment of the problem).

[16] usually the effect is not large and affects $C(q_{inv})$ at most on the level of a few percent

Correction of data in Boson Intensity Interferometry

As we already mentioned, an approach where the source is parametrized with a Gaussian (or some other analytical form) and the relevant source characteristics are then extracted by fitting the data, is widely used in the field of boson intensity interferometry. Historically, in this approach, all effects leading to deviation of the correlation function from the "ideal" Fourier transform behavior (eq. 2.12) of the data are treated as a distortion and an attempt is usually made to remove these effects in order to make the Gaussian (or other, as appropriate) fit feasible. This is accomplished by applying various *correction factors* to the data.

It is important to remember that, according to this prescription, not only the effects of measurement, but also the f.s.i., such as Coulomb, are corrected for (see the discussion of the Gamow factor in section 2.3). Hence, the overall correction factor has several components. Note that

- each component of the correction factor is momentum-dependent (and the Gamow factor, according to eq. 2.13, can be expected to have the strongest dependence), therefore, the relevant corrections are, in fact, bin-specific *(bin-wise correction)*[17]

- the components of the correction *do not factorize*

The factorization is not possible because, as mentioned above, the relative mag-

[17]meaning that each bin of the relevant q_{inv} distributions (R and/or B) should be multiplied by a different number

nitude of the distortion due to momentum smearing, in a given bin, depends on the behavior of the q_{inv} distribution in the vicinity of that bin (subject to other correction factors), plus the correction for the "residual correlations in the background" [40, 16, 35] also depends on the final shape of the correlation function that *is not known beforehand.* In order to solve this problem, an iterative procedure is usually introduced whereby the bin-specific values of the correction factors are calculated based on the "current" fit parameters, then applied to the "current" correlation function and the fitting procedure is repeated; usually the process converges within a few iterations [35].

It would be interesting to question the validity of this approach more rigorously, from the mathematical point of view, however, it is beyond the scope of this thesis. We emphasize, however, that due to the impossibility of factorization of corrections, this method is only applicable if one is using a model of the source, such as a Gaussian, (a) where the parameters can be varied freely, and (b) a known analytical form exists for the theoretical correlation function. As will be discussed later, our goal is to compare the data with the results from a sophisticated event generator, so neither (a) nor (b) is attainable.

Applicability of Corrections to the pp Correlation Function

The problem of taking into account the factors that influence the correlation function without invoking the fitting procedure is analyzed in [25]. In particular, it is concluded that de-convoluting the "real" shape of the correlation function by removing the effects of the finite momentum resolution, *if done without assumptions about the form of the correlation function*, bears a close resemblance to the Fourier analysis technique, involving matrix inversion. Since the "signal" to be restored (the correlation function) is "noisy" (i.e. has statistical fluctuations as well as inevitable admixture of background events etc.), application of this technique is found to lead to sometimes divergent and, in general, unreliable results.

Since we expect the undistorted $C(q_{inv})$ (Fig. 2.4) to have somewhat sharper features in case of protons, compared to bosons, the correction factors become respectively larger and the "de-convolution" more difficult.

Perhaps the most important comment on correcting the correlation function concerns the final state interactions. Even though the f.s.i. are present in both proton and π/K cases, their relative significance for the measurement is different. As already pointed out, the shape of the proton correlation functions is, by large, determined by the f.s.i. and to a lesser extent by the statistical effects [19, 14]. Moreover, it is due to the f.s.i. that it is rather sensitive to the source parameters[18] (such as size). In this respect *not correcting the data* for the f.s.i. should be considered beneficial as it improves the sensitivity of the measurement.

[18]recall the $1/r^3$ dependence of the correlation function enhancement on source size, that we discussed earlier

Treatment of the Proton Correlation Function

As we have just shown, direct application of the methods from Bose-Einstein interferometry to the treatment of the proton correlation function is problematic.

An alternative approach has been suggested in [25], under the name of "Response Function Distorted Theoretical Prediction", or *RFDTP*, briefly discussed in Appendix C. In essence, one starts with a model of the particle source (in [25] it was a Gaussian parametrization), then puts in the correlations due to quantum statistics and the f.s.i., and finally applies the apparatus response function to take into account the measurement-related effects considered above. The apparatus response function is determined by means of a sufficiently realistic Monte Carlo simulation. The resulting correlation function is then compared directly to the data (which is not corrected at all). Furthermore, the parameters of the source can be varied in order to fit the experimental data, thus allowing extraction of the spatial characteristics of the reaction[19]. It should be stressed that the method is universal and can, in fact, be applied to any kind of correlations, including Bose-Einstein.

The *RFDTP* method, as used in [25], has certain limitations. In particular, only "real" q_{inv} distribution (R) was convoluted with the apparatus response function[20], and the "background" distribution (B) was taken from the experimental data. Since B is itself subject to various instrumental effects (section 2.4.4),

[19] in fact, this method was used in many previous studies of two-proton correlations that we briefly discussed in chapter 1

[20] see Appendix C

the whole method becomes somewhat less consistent.

In our study of two-proton correlations, we took the *RFDTP* technique one step further. During the calculation of the theoretical correlation function, the statistical weight of each proton pair is calculated according to eq. 2.20, and then propagation of *each particle* through the spectrometer is simulated. Then, track reconstruction is performed with the same software as was used with the actual data. The reconstructed particle momenta are then used to calculate q^{ij}_{inv} in equations 2.21 and 2.22. This way, important factors such as the momentum-dependent reconstruction efficiency and effects of the limited acceptance are included in the calculation of $C(q_{inv})$ in a consistent manner[21]. A complete description of the method will be presented in chapter 5.

2.5 Practical Aspects of the Correlation Measurement

As discussed in the previous section, the two-particle resolution of the apparatus is an important factor in the analysis and interpretation of the experimental correlation data. We will discuss here other factors that must be taken into account (the actual details of necessary calculations are explained in chapter 5).

[21]as a side comment, in this approach the Monte Carlo *emulates the experiment*

2.5.1 Centrality of Events

As already mentioned in chapter 1, the impact parameter b of a heavy ion collision defines the geometrical characteristics of the collision[22], and hence the volume of the resulting source. Therefore, we would like to have an estimate of the "centrality", or the impact parameter range, of the events in the data sample. Often the centrality is quoted as a fraction, in percent, of the total cross section – for example, "5% most central".

Such "percentage" estimates are usually based on certain observables, such as transverse energy or charged particle multiplicity, that are expected to be correlated with the impact parameter [35, 3]. For example, one can perform a comparison of the charged particle multiplicity observed under the relevant trigger conditions with that measured with the "minimum bias" trigger[23].

We have chosen an approach whereby one extracts the b distribution by measuring particle multiplicity of actual events and matching the predictions of a theoretical model to the observed values (this is possible because, in general, particle multiplicities are predicted rather well by event generators). This way, we don't necessarily have to assume any particular shape of the b distribution. In chapter 5 we explain the procedure in detail.

[22] in chapter 5 we will discuss in detail the dependence of the correlation function on the impact parameter

[23] hence in this method the "percentage" is essentially the ratio of normalized rates

2.5.2 Decay Protons and Other Background Tracks

As in any measurement in high energy physics, one must consider the problem of various sources of background and their influence on the observable – in our case, on the shape of the measured proton correlation function. Three such sources have been identified:

1. "Fake" tracks
2. Misidentified particles
3. Protons coming from decays of secondary particles in the vicinity of the target

As will be discussed in chapters 3 and 4, the particle identification and tracking capabilities of the NA44 spectrometer made it possible to control, quite efficiently, particle misidentification[24] and "fake" tracks.

Item 3 in the above list turns out to be the most significant background factor. In particular, the decay

$$\Lambda \to p + \pi^-$$

can not be identified by the NA44 apparatus[25], and protons resulting from such decay, as will be shown later, are reconstructed with a high efficiency (the branching ratio for this decay is about 64%). It is clear that a proton pair in which one of

[24] using Čerenkov counters and precision time-of-flight measurement, the proton sample contamination by kaons was kept at a better than 1% level

[25] NA44 does not have tracking detectors in the immediate vicinity of the target, that would be necessary if one wants to tag Λ decays

the particles comes from a Λ decay cannot possibly exhibit any kind of correlated behavior, since Λ's, on the space-time scale of a nuclear reaction, decay infinitely far from the original particle source ($c\tau = 7.89$ cm). The presence of such uncorrelated pairs will "dilute" the observed correlations, leading to suppression of the correlation peak and filling up of the dip at low q_{inv} (Fig. 2.4). We defer the quantitative discussion of this issue until chapter 5, and for now just note that the contribution of such decays is not trivial. In principle, one should also look at decays like $\Sigma^+ \rightarrow p + \pi^0$ and $\Sigma^0 \rightarrow \Lambda + \gamma$, and even $\Xi^0 \rightarrow \Lambda + \pi^0$ and $\Xi^- \rightarrow \Lambda + \pi^-$. We will find, however, that the decay of Λ's is by far the dominant factor[26].

2.5.3 Summary

Based on the previous discussion, we can expect that there are three main factors to be taken into account when considering the experimental proton correlation function:

- Two–particle resolution of the spectrometer
- Event centrality (i.e. trigger bias)
- Contamination of the proton sample by strange baryon decays

These issues will be addressed in the following chapters and in chapter 5 in particular.

[26] There's a great deal of uncertainty, at present, concerning data on the strange baryon production in heavy-ion collisions. The heavier baryons mentioned here should be considered less important, given the large systematic error in the Λ production measurements

2.6 The Particle Source Model

A review of particle source parametrizations can be found in [13]. In [25] and in a number of other studies of proton correlations, as well as in the vast majority of works in the field of boson interferometry, a Gaussian parametrization of the particle source is used. There is no compelling physics motivation for using Gaussians; on the other hand, in many cases they allow to obtain a reasonably good fit of the data [16, 15]. We already considered an example of such parametrization in equations 2.6 and 2.7.

In fact, parametrizing the source effectively constitutes introducing a model; in particular, implicit in this approach are the following:

1. The particle source density distribution is Gaussian
2. There is no correlation between the spatial coordinates of the emission point (x, y, z) and the components of the emitted particle's momentum (p_x, p_y, p_z)
3. Assumptions have to be made about the time dependence of particle emission

Item 2 on this list seems especially unrealistic, since in virtually any scenario of a heavy-ion collision there is an expansion stage, meaning that there actually *is* a correlation between the coordinates of particles and their momenta [3, 19, 15]. Also, an assumed time dependence of the source will also have an effect on other parameters of the fit[27].

We decided to not use the Gaussian parametrization since, in our opinion, the source parameters extracted from it would suffer from systematic uncertainties that are hard to control (due to the assumptions discussed above). Instead, the RQMD 1.08 event generator ([27, 28, 29] and references therein) was used as a basis for comparison. The RQMD model, which will be briefly discussed in section 5.2.2, enjoys a fair degree of success in explaining a variety of characteristics of heavy-ion collisions and, in general, compares favorably with boson interferometry measurements from NA44 and several other experiments [31]. An independent interferometric measurement with a different particle type, such as the proton, can serve as an additional check on the validity of the model and as a probe for new phenomena.

Although, as we will see, at present there are certain discrepancies between its predictions and the experimental data, the RQMD model is still a valuable tool in the investigation of heavy-ion collisions, and in any case gives a lot more insight into the configuration and evolution of the source than a Gaussian parametrization.

[27]in the majority of proton correlation studies that we mentioned in chapter 1, an assumption of instantaneous emission ($\tau = 0$) was made

Chapter 3

The NA44 experiment

3.1 Introduction

This chapter contains a description of the NA44 Focusing Spectrometer in the configuration which was used to take the data presented in this thesis[1], in 1991-1993. The following sections, respectively, describe the physics considerations of the spectrometer and its overview, the detailed functioning of the principal subsystems, trigger, data-acquisition (DAQ) and the on-line detector monitoring.

3.2 The Concept of the Detector

The NA44 design goal is to provide good particle identification capability and momentum resolution for particles measured at mid-rapidity, to allow the study of single identified particle inclusive distributions (π, K, p, d), and two- and three-particle correlations ($\pi\pi, KK, pp$).

NA44 is a focusing spectrometer; the idea behind this design is to provide

[1] The spectrometer underwent significant changes in 1994-1995, when it was upgraded to run with ^{208}Pb beams. The improvements include introduction of new wire chambers with pad and strip readout for tracking, and RICH-type detector for enhanced multiparticle PID. The reader is referred to recent NA44 publications for details.

magnetic transport of some fraction of the secondary particles, from a selected portion of the phase space, throughout the whole spectrometer, where they are measured by a variety of detectors with a relatively small surface area. Such design

- optimizes acceptance of particles with small relative momentum
- allows one to concentrate on quality measurement of a few particles, out of many hundreds produced, with low multiplicity and low backgrounds inside the acceptance
- allows for a simple trigger on interesting events, such as pairs of identical particles, and on particle type (for example, π, p, K); this feature was important since it made possible faster accumulation of data samples (as an example, it was possible to trigger on rare events such as K^-K^-)
- makes the *geometric* acceptance relatively small, allowing to instrument it with advanced detectors in an economical way and facilitate the particle identification task

The principal particle identification technique in NA44 is the time-of-flight measurement[2]. This measurement, and the measurement of particle tracks, were performed by arrays of scintillation counters *(hodoscopes)*.

[2] see section 4.4.3 for details

3.3 The NA44 Spectrometer

3.3.1 Layout of the Spectrometer

Experiment NA44 is located at CERN (European Organization for Nuclear Research) in Geneva, Switzerland. It uses the H4 beam line of the CERN Super Proton Synchrotron (SPS) and is housed in the **North** experimental **Area** (see Fig. 3.1). It is assigned the serial number **44**, hence the name of the experiment. The SPS complex delivers beams of protons at 450 GeV/c and fully stripped ^{32}S ions at 200 GeV per nucleon[3]. The accelerator works cyclically : the sulphur beam is on the target for $\approx$5 s ("burst"), with $\approx$14 s breaks ($\approx$2.5 and 12 seconds, correspondingly, for protons). Typical intensities during data taking were 6×10^6 ^{32}S ions per burst (or 15×10^6 protons). The beam cross section was 0.2 mm (horizontal) $\times$ 0.5 mm (vertical) and it was possible, by means of rather sophisticated beam optics, to precisely position it on the center of the target (typically, a disk of 10 mm diameter). The beam particles that did not interact in the target (i.e. most of them) are dissipated in the yoke of D1 (see description below) and adjacent shielding blocks.

The layout of the spectrometer is shown in Fig. 3.2. The total length of the detector is about 25 m. The focusing properties were provided by three superconducting quadrupoles (Q1,Q2 and Q3), whereas dipole magnets D1 and D2 served as means for the momentum analysis. Dipole D3 was used in conjunction

[3] starting in 1994, ^{208}Pb beams became available

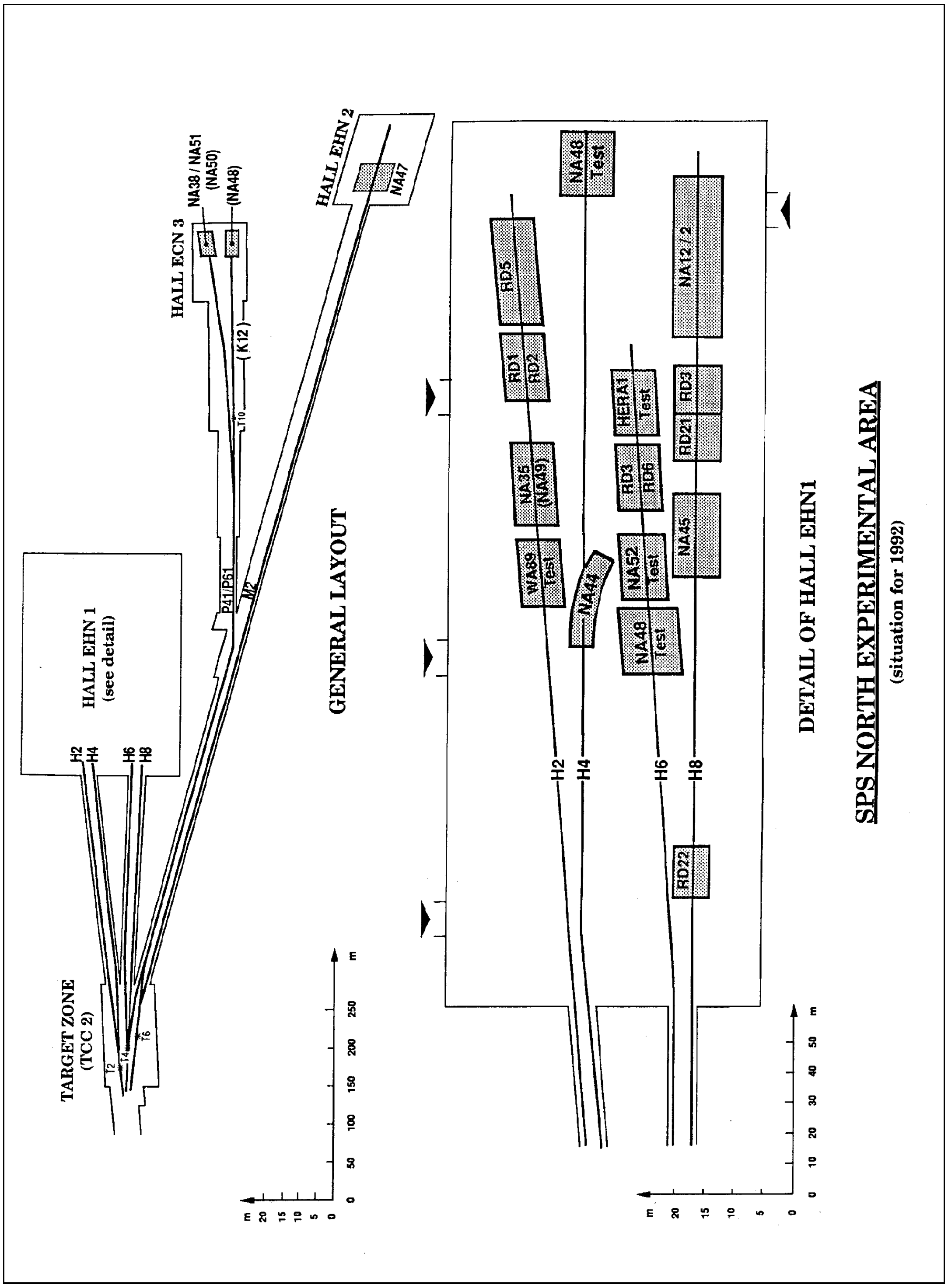

Figure 3.1: Layout of the North Experimental Area

with a system of wire chambers (MWPC1-MWPC4) to perform a check on the absolute momentum calibration of the apparatus[4].

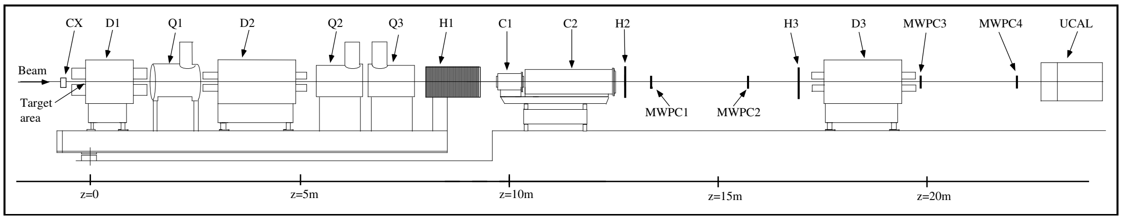

Figure 3.2: The NA44 experimental set-up, side view.

One of the most crucial elements of the spectrometer was a system of three hodoscopes, H1-H3, reviewed in detail in section 3.3.3. These hodoscopes provided the means for tracking (hence, for particle momentum determination) and for precision time-of-flight measurement (used for particle identification). The coordinate system of the hodoscopes is defined in the following way: the z axis coincides with the optical axis of the spectrometer and passes through centers of Q2-Q3, H1-H3 and C1-C2. The x axis is horizontal and perpendicular to z, and y is the vertical dimension.

Particle identification on the trigger level was provided by two Čerenkov counters, C1 and C2.

Other important detectors included the Beam Counter and the so-called T0 counter, whose design and properties will also be discussed below. They were used for triggering and timing purposes.

[4]in the setting used to take the data presented here, corresponding to the nominal momentum 6 GeV/c, the $B \cdot L$ value was 1.44 T-M for D1 and 2.04 T-M for D2 and D3

To characterize events in terms of the charged particle multiplicity, the NA44 spectrometer was equipped with a highly segmented Silicon Pad detector located downstream of the target.

Only one charge state particles, i.e. positive or negative, could be detected in the spectrometer at a time. The momentum range of the spectrometer setting used to take the data presented here covered a band of $\pm$ 20% about the nominal momentum of 6 GeV/c. The acceptance in (y, p_T) for various particle types and three different momentum settings is shown in Fig. 3.3. The acceptance for protons in the 6 GeV/c setting is shown in more detail in Fig. 3.4. It spans the rapidity range from 2.35 to 2.70, and a p_T range from 0.00 to 0.66 GeV/c. At the nominal sulphur beam momentum, 200 GeV/c, the nucleon–nucleon c.m.s. reference frame corresponds to $y = 3.03$, and at the nominal proton beam momentum, 450 GeV/c, it correponds to $y = 3.43$.

We will now discuss the following detector subsystems, important for our analysis of proton correlations: the Target Area detectors, the Hodoscopes and the Čerenkov counters.

Then, we will briefly review the auxiliary detectors, not involved directly in the present analysis – the Wire Chambers, and the Uranium Calorimeter.

3.3.2 The Target Area

Grouped in the target are the following detector subsystems:

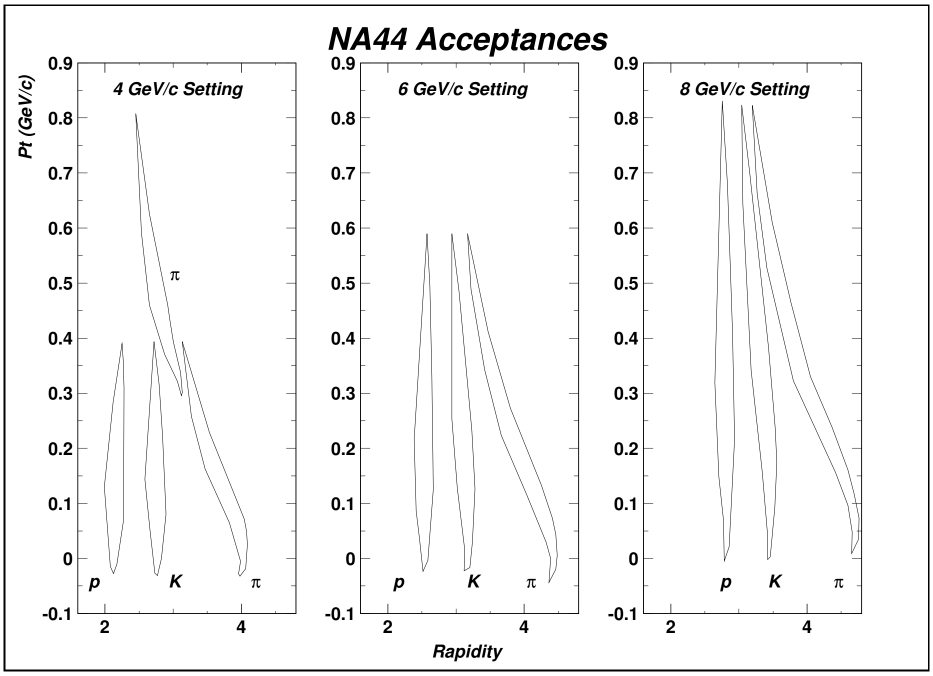

Figure 3.3: The NA44 acceptance for different particle types and momentum settings.

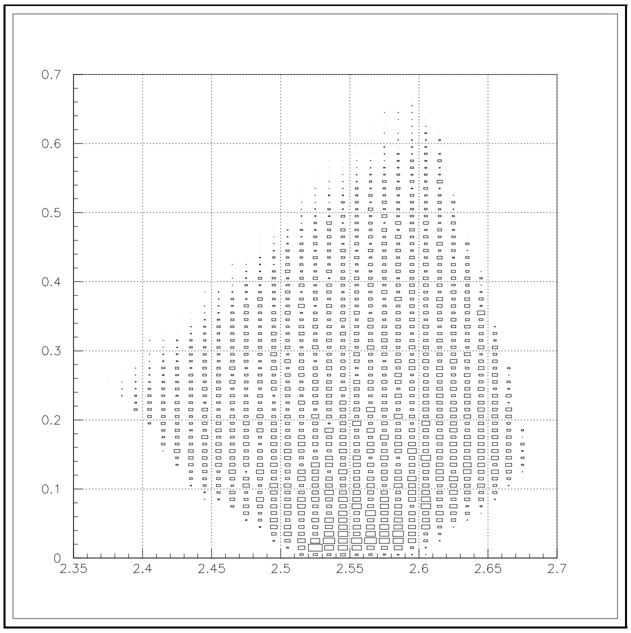

Figure 3.4: The NA44 acceptance for protons.

- the Target, on a mechanized target mount
- the Beam Counters, counting the beam particles and defining the start signal for the time-of-flight system
- the T0 counter, used for triggering purposes and, in particular, to control the selectivity of the trigger with respect to the event centrality; as will be explained later, in some cases it was also used to provide the start signal for the time-of-flight system
- the Silicon Pad Detector for the measurement of the charged particle multiplicity

We will now describe each of these subsystems.

The Targets

The targets used to take most of the data in NA44 are disk-shaped, 10 mm in diameter, and are of different thicknesses and materials. The data presented in this thesis were taken with ^{208}Pb targets: one target, 5 mm thick, was used to study S+Pb reactions and the other, 10 mm, for p+Pb runs. The disk is attached to a target mount by means of a styrofoam ring, in order to reduce interactions in the material immediately adjacent to the target. The mount is mechanized and allows remotely controlled insertion of the target into the beam.

One would like, of course, to run with targets as thin as possible to reduce the effect of multiple scattering that leads to worsening of the momentum resolution.

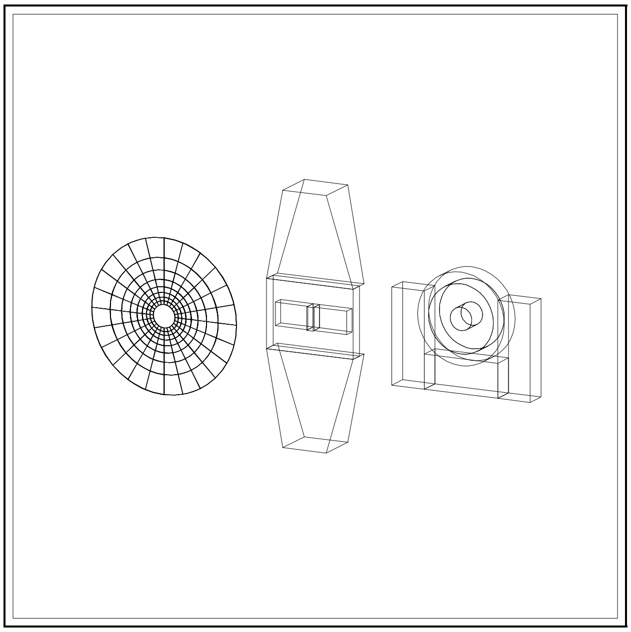

Figure 3.5: `GEANT` images of the elements of the Target Area. On the left, the segmented silicon pad detector; in the middle, the T0 counter; on the right, the target on the mount (see text)

Having thin targets, on the other hand, reduces the event rate. The target parameters quoted above were chosen, after some experimentation, in order to have an interaction rate that would allow sufficient statistics to be collected, as a tradeoff. This rather large material thickness makes multiple scattering in the target the leading contribution to the overall momentum resolution of the spectrometer and had to be taken into account, via Monte Carlo simulation of the apparatus, when comparing the results of the data analysis to a "theoretical" correlation function. This is explained in detail in chapter 5.

Runs taken for test purposes without target showed essentially no background pair events.

The Target Area Counters

In summary, the counters located in the immediate vicinity of the target provide the start signal for the time-of-flight system, determine if there was an interaction in the target, and count the beam particles.

As already mentioned, the start signal for the time-of-flight system can be determined using two alternate systems: the Beam Counter (labeled CX) and the scintillation counter (labeled T0). The CX counter exists in two implementations – Čerenkov, used for S+Pb runs, and scintillation, used to take p+Pb data. Its additional purpose is to count the beam particles.

The CX beam counter, used when running with sulphur beam, is based on the Čerenkov principle and consists of two cylindrical gas radiator volumes, CX1 and CX2, each viewed by a separate PM tube. The respective signals are further fanned out and sent to discriminators connected to the trigger logic, and also to TDC's and charge integrating ADC's so as to measure both amplitude and timing information. Having two independent time measurements makes it possible to measure the intrinsic time resolution of each of the CX detectors, and it was found to be approximately 35 ps. This number itself carries a degree of uncertainty due to systematic errors such as the finite binning of the TDC scale but, as will be discussed later, the overall TOF resolution is anyway dominated by the hodoscopes.

The number of photoelectrons produced in the CX counter is proportional to the Z^2 of the passing particle. While the counter could operate efficiently with sulphur beams, in case of proton projectile the signal becomes too small to be useful. Instead, the T0 counter (discussed below) was used to generate the TOF start signal when taking p+A data, with time resolution of about 110 ps. The CX Čerenkov counter is then replaced by a small scintillation counter located upstream from the target, which used to count the beam particles.

The principal instrument used to detect *interactions in the target* is the T0 counter. It consists of two small pieces of scintillator, $10 \times 15 \times 5$ mm, positioned behind the target and separated by a narrow gap, $\approx$3 mm, so that the beam particles that didn't interact in the target go through this gap and don't yield any signal. The scintillator pieces were embedded in a plastic plate coupled with two long lightguides carrying the light signal to two PM tubes (top and bottom) located outside of the magnetic field of dipole 1 (Fig. 3.5, center – central part of the T0 assembly). In the case of interactions, however, the charged secondaries pass through the scintillator and produce a signal that is proportional to the multiplicity of the event. Hence, T0 can be used to tag the event centrality on the trigger level (see the section on the trigger system) by including the discriminated T0 signal in its logic[5].

In order to better define the beam, there was also a veto counter (a small paddle with a hole of 4 mm diameter), located at 2 cm before the target, and an additional veto counter for the CX counter.

The Silicon Pad Detector

All data presented here are characterized by the charged particle event multiplicity, as measured by the Silicon Pad Detector. The detector used in the 1991-1993 runs was a circular silicon wafer, of 3.350 cm radius, with a small central hole, of the radius 0.500 cm (see Fig. 3.5, left). The detector was located at 7.0 cm downstream from the nominal target position. With this geometry, the charged-particle multiplicity distribution was measured with 2π acceptance in ϕ, covering the pseudorapidity range $1.5 < \eta < 3.3$.

The detector was constructed by layering the thin (300 μm) silicon wafer over

[5]Further analysis of the recorded events in terms of their centrality is possible off-line using T0 and/or the Silicon Pad Detector data, as will be discussed separately

a ceramic readout board (760 μm thickness) whose function was to provide structural support and fan out the signals from each pad to the peripheral connectors that were, in turn, soldered to the readout PC board housing the front-end electronics. The silicon disk was partitioned into 24 equal azimuthal sectors (each covering 15 degrees), and then radially into 8 rings with outer radii of 0.654, 0.816, 1.011, 1.256, 1.567, 1.968, 2.500, 3.350 cm, thus producing 192 independent pads. The purpose of such division was to provide, roughly, equal occupancy in each of the pads.

The readout PC board was, in turn, mounted on a stiff aluminum plate, with a central window cut through to minimize the amount of material in front of the detector, and enclosed in a thin aluminum shielding box. The `GEANT` picture of the assembly is shown in Fig. 3.6. Each channel was instrumented with a charge-sensitive ADC. The charged particle multiplicity, in the fiducial η range, could be found by counting the number of pads giving signals corresponding to the single as well as multiple minimum ionizing particle peaks (double, triple, etc). As will be discussed in chapter 4, in order to estimate the *event centrality*, it is sufficient to simply count the number of pads with signals above the pedestal, thus avoiding the issue of multiple occupancy[6].

The 192 pads provide a certain level of redundancy, when a few failed pads can be tolerated – the resulting inefficiency can be taken into account in a rather

[6]as we will see, it was accomplished by means of a complete Monte Carlo simulation of the silicon detector and the target area

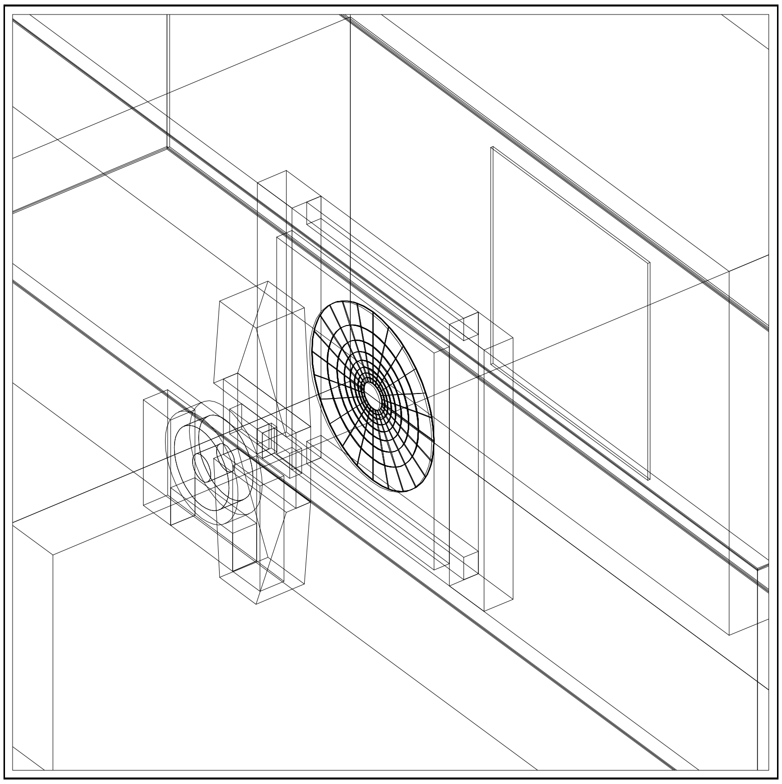

Figure 3.6: `GEANT` image of the target,T0 counter and the Silicon Pad Detector Assembly

straightforward manner.

3.3.3 Tracking and Particle Identification (PID)

The Hodoscopes

The spectrometer used three highly segmented scintillator hodoscopes, named H1, H2, and H3 [41], for tracking and time-of-flight measurements. Each of the hodoscopes consisted of thin vertical slats of scintillator. Geometrical parameters of the hodoscopes are given in Table 3.1[7].

Table 3.1: Geometry of the hodoscopes

Hodoscope No.	Slat dimensions,mm	Number of slats	Nominal Z coordinate,m
1	$28 \times 1 \times 260$	50	8.62
2	$6 \times 6 \times 200$	60	13.88
3	$13 \times 10 \times 220$	50	18.35

The hodoscopes are the heart of the apparatus since they provide both tracking (hence, momentum reconstruction) and PID. Each slat had individual PM tubes (Hamamatsu R3478S) attached on the top and on the bottom; the signals from PM tubes were read out by

- discriminators, for triggering
- TDCs, for time-of-flight measurement and also for the y coordinate determination

[7] H1 is positioned at a 5 deg angle with respect to the central axis of the detector, H2 and H3 are perpendicular to that axis

- ADCs, to measure amplitude of the signals, necessary for slewing correction and handling of multiple hits, as well as to confirm that the signal is compatible with a minimum ionizing particle

The x and z coordinates of the track are defined simply by the slat that has a signal above a certain threshold (i.e., had a "hit" on it). The y coordinate is determined by comparing timing information from the top and bottom TDC's (details are presented in the chapter on data analysis). Given these measured coordinates, and with knowledge of the magnetic fields in the spectrometer, one can reconstruct the momentum[8].

The time of flight (TOF) was measured in all three planes, however only TOF from H3 was used for this analysis since it turned out to be of much better precision due to the large flight path (18.35 m). The time resolution of H3 was about 100 ps [41]. Given the TOF and the flight path, one calculates the velocity β of the particle, and in combination with the momentum information, it can be used to determine the particle mass. The particle identification scheme in NA44 is explained in detail in section 4.4.3.

Each hodoscope assembly also included a set of three so-called "finger counters" which were thin horizontal sticks of scintillator, whose position was precisely known. They were used for calibration purposes[9].

[8] see section 4.4.1

[9] basically, their position was used as a reference, to equalize the TOF differences of the top and bottom PM tubes, and subsequently determine the y coordinate of tracks

The Čerenkov counters

The two Čerenkov counters C1 and C2, seen in Fig. 3.2, are used for particle identification. They both are shaped like tubes and used pressurized gas as a radiator; some of their parameters are shown in Table 3.2. Since, as mentioned

Table 3.2: Parameters of the threshold Čerenkov counters

Counter	Length, cm	Diameter, cm	Gas	Pressure range,atm
C1	62	23	Freon 12	1.4-2.7
C2	229	23	N/Ne	1.0-1.3

earlier, at a given momentum setting, the focusing spectrometer accepts a rather limited band of particle momenta, it makes it easier to associate a given particle type with a certain range of velocity. Thus, operation in a simple threshold mode was possible: since the Čerenkov radiation takes place if the particle is traveling at velocities larger than $v_{threshold} > c/n$, one can adjust the pressure in the counters (and therefore the index of refraction n) such that only particles below a certain mass radiate. With proper pressure settings, one can thus distinguish μ, π, K and p using C1 and discriminate between e and μ, π using C2. The properties of the Čerenkov counters are illustrated in Table 3.3, where we show the indices of refraction for both counters and the threshold momentum values for particles of different mass, in the particular pressure setting used to take the data presented here[10].

The Čerenkov counters could be included in the on-line trigger logic in one

[10] electrons are not in this table as they have an extremely low threshold

Table 3.3: The threshold momentum values (in GeV) of the Čerenkov counters

Counter	n-1	π	K	p
C1	1.657×10^{-3}	2.5	8.9	16.9
C2	0.342×10^{-3}	5.2	18.3	34.8

of three modes: "ignore", "veto" or "require" and provided the necessary trigger selectivity. In the particular setting used to take the data presented here, both counters were used in "veto" mode, hence only events containing kaons and/or protons were accepted.

The Wire Chambers

The four multiwire proportional chambers (MWPC1-4) played an auxiliary role, covering only a part of the acceptance. In conjunction with dipole 3, they were employed to independently check the momentum scale and resolution of the spectrometer[11]. Chambers 1 and 2 were located before the magnet and defined a track before it would enter the dipole, whereas chambers 3 and 4 were placed downstream of the magnet and used to measure the outgoing track that is bent by a few mrad angle. Each chamber has 256 vertical anode wires with 2 mm pitch as well as 96 horizontal cathode strips, 5 mm wide. The wire signals are read out using Lecroy PCOS electronics, while the cathode strips are instrumented with Amplex chips.

[11]it was found that in the 8 GeV setting, there was about 1.25% difference between the momenta as reconstructed by the MWPC and the hodoscopes. The reader is reminded that in the present study we concern ourselves with *the relative momenta* of particles, so a small shift of the *absolute* scale is not important

The Uranium Calorimeter (UCAL)

UCAL is the last in the chain of detectors in NA44 and is located at the very end of the spectrometer (see Fig. 3.2). It is made up of 9 "stacks"[12] that are divided into electromagnetic and hadronic sections. The stack is a sandwich assembly of thin uranium plates and sheets of plastic scintillator that are optically coupled to the wavelength shifter (WLS) plates that transport the light signal out of the stack, to the PM tubes mounted on the backplane. There are 6 pairs of WLS plates per stack and they are constructed in such a way that the stack is effectively segmented into 6 "towers" of 20×20 cm cross section. Thus, each tower has 4 photomultiplier tubes: 2 in the electromagnetic section and 2 in the hadronic, and the total channel count is $4 \times 6 \times 9 = 216$. Each tube is instrumented with an ADC.

The UCAL allowed e, μ and hadron separation and proved extremely useful in solving the background problem when extracting rare particles (such as deuterons) from the single particle data sample. To this end, the tracking system was required to provide a pointer to the particular tower in UCAL that was hit, for cluster analysis. However, UCAL was not suited for study of low relative momentum pairs due to insufficient spatial resolution and was not used in the present proton pair analysis.

[12]The stacks were "recycled" from the HELIOS experiment at CERN

3.4 Readout

3.4.1 Trigger

The basic trigger condition can be written as a coincidence of signals

$$Trigger = (\text{Valid Beam})\times(\text{T0})\times(\text{Hits in the spectrometer})\times(\text{Čerenkov counters})$$

where (Valid Beam) $= CX \times \overline{VETO}$. The T0 represents a signal above the threshold in the T0 counter. "Hits in the spectrometer" is a requirement of at least two hit candidates in each of the three hodoscopes, where a hit candidate is defined as a discriminated signal in any of the hodoscope's "top" PM tubes. Ideally, one would use signals from both top and bottom tubes in coincidence to provide better rejection against various backgrounds and make the trigger more selective, however, in 1991-1993 the simpler scheme with just one discriminator per slat was used[13], and a fraction of events were accepted that actually contained a combination of a valid track and "garbage" hits. Such events were eliminated in the off-line analysis.

The "Čerenkov counters" means the correct state of the $\check{C}_1$- $\check{C}_2$ system and, in case of the Kp trigger, was $\overline{C_1} \times \overline{C_2}$, meaning that light particles (e, μ, π) were vetoed on-line[14].

The threshold in T0 could be varied depending on the desired data taking

[13]The scheme with top and bottom channels of each slat connected to a coincidence unit was implemented as a part of the detector upgrade in 1994

[14]this could, *in principle*, introduce some unwanted distortions in the trigger, however, the NA44 acceptance is very narrow and covers only a tiny fraction of the available phase space, allowing us to safely neglect such effects

conditions. The higher the threshold, the more biased is the trigger (i.e. more selective to events with higher multiplicity, and ultimately to more "central" events). We should note, however, that the overall "centrality", or bias, of the trigger, depends also on the bias introduced by the "hits in the spectrometer" requirement – obviously the probability to detect a track in the rather narrow NA44 acceptance depends on how many particles are produced in an interaction, i.e. on the event multiplicity. Depending on the beam energy, spectrometer setting and the projectile+target system, the relative bias due to the T0 threshold and the hits requirement can be different. The trigger conditions chosen to take the data presented here were such that, in the S+Pb data sample, the trigger was moderately biased towards central events, as will be discussed in detail in chapter 5. On the other hand, the multiplicities characterizing the p+Pb collisions are much lower (see discussion of the geometrical factors in chapter 1), and the "hits" requirement is likely to introduce a very strong bias towards central events. This was confirmed in the off-line analysis (see chapter 5).

When a trigger arrives, an appropriate gate, 50 ns, is generated for the ADC and TDC modules. In terms of the possible pile-up situation, there exist the following possibilities:

- during that time, there is an interaction of another beam particle in the target
- there was a recent interaction in the target and there are still transient

processes in some of the detectors and/or electronics

To prevent such "corrupted" events from getting into the data stream, there was an auxiliary gating scheme, called "before" and "after" protection, with the gate duration of about 100 ns. During that time, the data acquisition system could not accept any new triggers.

3.4.2 Readout electronics

The primary CAMAC modules used are 11 bit, 50 ps/channel Lecroy 2228 TDC's (8 inputs per module), 11 bit charge integrating Lecroy 2249 ADC's (16 inputs per module) for the assorted target area counters, 12 bit charge integrating Lecroy ADC 2280 system (with a special crate control module) for UCAL readout, with a very long conversion time of about 1.5 ms. Peak sensitive ADC's are used to instrument the silicon detector. Several 24 bit scalers are used primarily for normalization in the measurement of single particle cross sections.

3.4.3 On-Line Data Acquisition

Despite the fact that the NA44 Data Acquisition System (DAQ) was developed on the technological base that existed in the late eighties, before "client-server" and "distributed computing" really became buzzwords, it is interesting to see how it actually incorporated these concepts. The DAQ is based on CAMAC readout and a VME bus network interfaced with a few control and monitoring computers. In the configuration that existed in 1991-1994, the control functions were performed by a Macintosh II FX[15], based on a Motorola 68040 chip running at 40 MHz. The DAQ software was derived from a Fortran-based SPA^{3}W package developed at CERN. The package itself had been created in the framework of MacUA1 programming environment, developed initially for use in the experiment UA1, that included a proprietary RTF compiler (Real Time Fortran) optimized for speed and featuring additions like pointer arithmetic and in-line assembler, both rather important for on-line systems.

The basic idea behind the DAQ architecture of NA44 is the use of shared memory, that is implemented as VME RAM (buffer) that is accessible, independently, to both control and monitoring computers. A diagram of the DAQ system is shown in fig 3.7. The detector electronics (primarily ADC's, TDC's and scalers) resides in CAMAC crates and appears in the address space of the so-called DAQ Macintosh. This is accomplished via a 16 bit bus that connects a MICRON card occupying a nuBUS slot of the Macintosh with MacVEE modules sitting in the VME crate, and by means of the VME-resident branch driver modules. This computer is the principle run-control machine and is responsible for reading the events out from CAMAC, transferring the data into the VME buffer and writing it on tape, which is done "out of burst" so as to not slow down the DAQ. The tape system used is the IBM 4280 cartridge drive (industry standard) with 200 kB/sec capability, enough to accommodate the maximum DAQ rate.

[15]The DAQ has been upgraded in 1995 and now incorporates a VME processor for control purposes and a HP workstation for monitoring and user interface

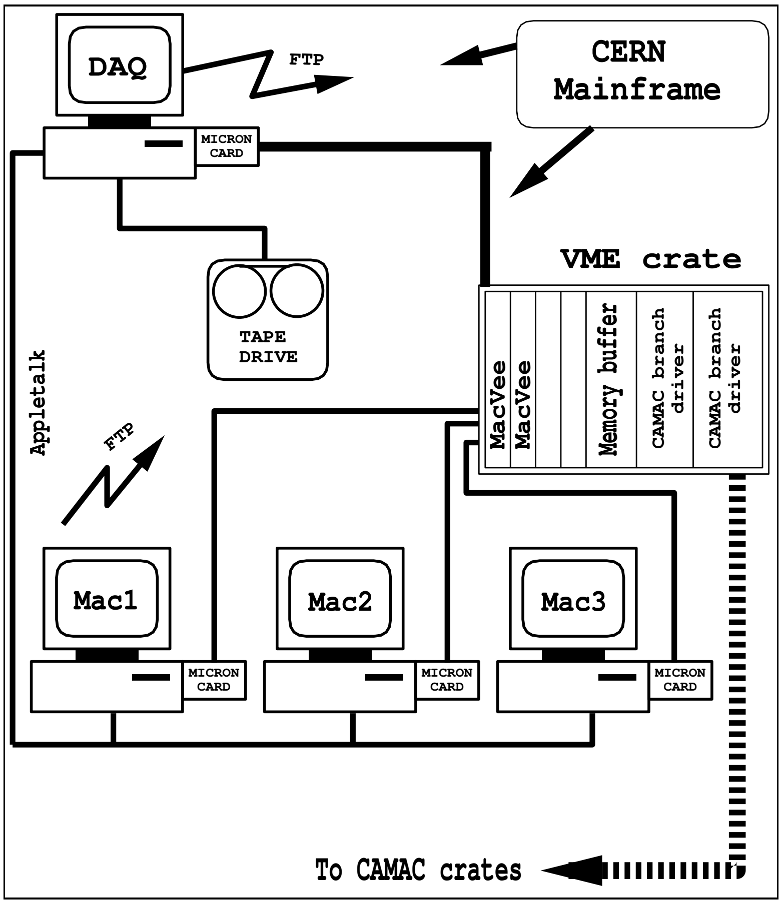

Figure 3.7: The diagram of the NA44 data acquisition system

The VME buffer could be accessed, asynchronously, by a number of different applications running on other computers. This makes for a transparent and flexible multiprocessor architecture. In the beginning of every run, the DAQ Macintosh handles the initialization stage, where trigger and various data-taking choices are made via a graphics user interface, and magnet currents are checked. A data file with complete running conditions is recorded and automatically transferred via the FTP link to an off-line computer (CERN VAX cluster) for insertion into the database.

Three other Macintosh computers are used for detector monitoring and various subsystem-specific programs. Mac1 is the primary histogramming monitor and is also used for low level debugging of the on-line data stream. Mac2 served as an event display terminal and also for controlling the programmable high voltage supply of the hodoscopes and the uranium calorimeter. Mac3 performs continuous monitoring of all detectors and checks on basic detector performance and some critical run parameters, such as dangerously high beam intensities. At the end of each run, it computes certain detector performance parameters and automatically transfers a set of histograms, via FTP, to the CERN VAX cluster, where a continuously active server program performs some simple formatting and prints out summary histograms on the printer located in the NA44 control room, where they are placed in the permanent log.

Chapter 4

The Data

4.1 Introduction

In this chapter we are going to discuss

- general features, quality and quantity of the experimental data
- calibration of the detector subsystems important for this analysis
- data flow in the analysis
- the event selection mechanism used to produce a sample of proton pairs from the raw data, with emphasis on the particle identification
- construction of the correlation function
- stability of the data with respect to the criteria applied during event selection
- sensitivity of the measured correlation function to the event centrality

4.2 The Experimental Data

The data sample analyzed in this thesis was taken in the 6 GeV Horizontal Setting (see chapter 3). It encompasses four data-taking periods from 1991 to 1993, and was recorded on a total of about 180 IBM magnetic tape cartridges (very roughly, 35 GB of information), which translates into $\approx 6 \times 10^6$ events divided between S+Pb and p+Pb data (see table 4.1). As can be seen from this table, the fraction

Table 4.1: The Data Sample

System	Number of tapes written	Number of triggers	Fraction of events with 2 valid tracks
p+Pb	83	2.5×10^6	$\approx 8\%$
S+Pb	96	3.5×10^6	$\approx 4\%$

of validated double-track events is rather low (that selection happens during the track reconstruction, described in detail later in this chapter). This has to do with the relative simplicity of the trigger, which required two hits, regardless of their positions, on each of the three hodoscope planes (see section 3.4.1). The background conditions in the spectrometer during actual running were not very favorable, and caused a number of events that contained "garbage" hits, i.e. hits produced in the hodoscopes by the background particles, in particular neutrons, coming from the beam dump and/or leaking through the shielding. However, according to Monte Carlo studies, such hits have extremely small reconstruction probability and don't contaminate the final sample, though they cost in terms of statistics. Another immediate factor reducing the available statistics, which has to do with the particle identification scheme in the experiment, is a factor of 4 coming from the fact that due to the trigger conditions (Čerenkov settings) both kaons and protons were accepted, and since the abundances of these particles in the given kinematic regime happen to be about the same [1], the successfully reconstructed pairs are pp, Kp, pK, KK, in equal proportion. Hence even the background-free data contains only 25% of proton pairs. The details of the data reduction will be discussed later, but for now we note that one ends up with a rather clean pp sample of $\approx 30k$ events coming from S + Pb interactions and $\approx 15k$ for p+Pb data. That sample is subject to relatively small further reduction as a few more stringent cuts are applied.

4.3 Calibration

To be able to translate the raw data into physically meaningful quantities, one has to calibrate each measurement chain, that may include, for example, a photomultiplier tube, cable carrying the signal to the electronics racks and the electronic circuitry itself. To perform a calibration means to establish a transformation, with certain characteristic parameters ("calibration constants"), of the raw digitized data into some physical observable, such as energy, time, etc.

The major detector subsystems that required calibration were the hodoscopes and the Silicon Pad Detector [2]. The large amount of data being handled in the

[1] partially due to the acceptance of the detectors for these particles, in this particular setting

[2] there were also calibrations for the Uranium Calorimeter, but, since it was not used in this analysis, it is omitted here

experiment (thousands of tapes) warrants creation of an organized database of calibration constants with a high degree of automation. This was implemented as a random access RZ database based on `ZEBRA`, that provided storage of information in an N-tree with branches corresponding to running periods, detector subsystems, specific calibration periods etc. The software was capable of picking up the right calibrations for the given run. The portable `ZEBRA` file format was used to transfer the database and use it on different computers.

4.3.1 The hodoscopes

Since the hodoscopes are the principle particle identification tool in NA44, based on time-of-flight measurement, they require the most careful and continuous calibration, in order to achieve an adequate time resolution (of the order of 100 ps) and equalize all channels. Also, the amplitude information is important and needs to be calibrated as well; it was used for (a) the so-called "slewing correction" described below (b) rejection of events containing more than one track passing through a hodoscope slat (c) rejection of background, such as neutrons leaking from the shielding, characterized by a small signal amplitude [3].

The calibrations were done continuously, using real physics events as well as dedicated "finger" counter runs[4] used to calibrate the y coordinate measurement, and were organized in 4 stages, referred to as passes, with necessary iterations

[3] the latter two items are discussed in section 4.4.1
[4] see section 3.3.3

and refinement of calibrations constants; each pass involved “respinning” of a data tape. Here’s a brief synopsis of what is going on in each pass:

- PASS1: the pedestals are found for all hodoscope ADC’s and also for CX and T0 counters. After subtraction of these, “true” ADC counts are obtained. Also calculated is the crude TOF offset of each slat, obtained by subtraction of the start time value from TDC counts for each slat. Finally, the constants for the vertical coordinate measurement were obtained, using the linear parametrization

  $$y = y_{gain} \times (TDC_{bot} - TDC_{top} + y_{offset})$$

  and information from the “finger counters” that served as a y-reference.

- PASS2: Slewing correction – since the actual timing of the discriminator depends on the amplitude of the signal (the larger the signal, the sharper its leading edge and the faster the discriminator fires), an attempt was made to correct for this effect. In short, the TOF response was parametrized with the following form:

  $$TOF = A + B\sqrt{(ADC)}$$

- PASS3: further refinement of the slewing corrections calculated in PASS2

- PASS4: now, using the final values of slewing correction constants, the TOF offset and the vertical offset values are calculated again. The TOF offset was defined in such a way that, for dominant particle species, in our case

p and K, the particle with the shorter time of flight (K) would produce a peak located at zero on the TOF scale, in each slat. Thus all slats were equalized and the separation of particle species could be done, effectively, by placing an appropriate cut on the square of the mass that is a function of the TOF and the particle's momentum (see Fig. 4.10 and discussion further in this chapter). Finally, the ADC gains in each channel were normalized.

Using this rather sophisticated calibration chain, it was possible to achieve an adequate stability of the detector response. As an example, in Fig. 4.1 we present a scatterplot (with contour option) of the difference between the time-of-flight of protons and kaons, in TDC channels, as measured with hodoscope #3, versus the run number, for two different running periods; also, Fig. 4.2 shows the scatterplot of the ADC signal from a track in hodoscope #2 versus the run number. In both cases, the data are very stable in time, with the TOF difference between K and p remaining constant within 2% throughout the data-taking period and the ADC signal within 1%.

4.3.2 The Silicon Pad Detector

As already discussed in chapter 3, this detector is used for measuring event multiplicities with 2π acceptance in ϕ and fiducial pseudorapidity range $1.5 < \eta < 3.3$. The sizes of the pads are such that, under the trigger conditions used when taking the actual data, average occupancy of a given pad is, very roughly, ≈ 0.7 during

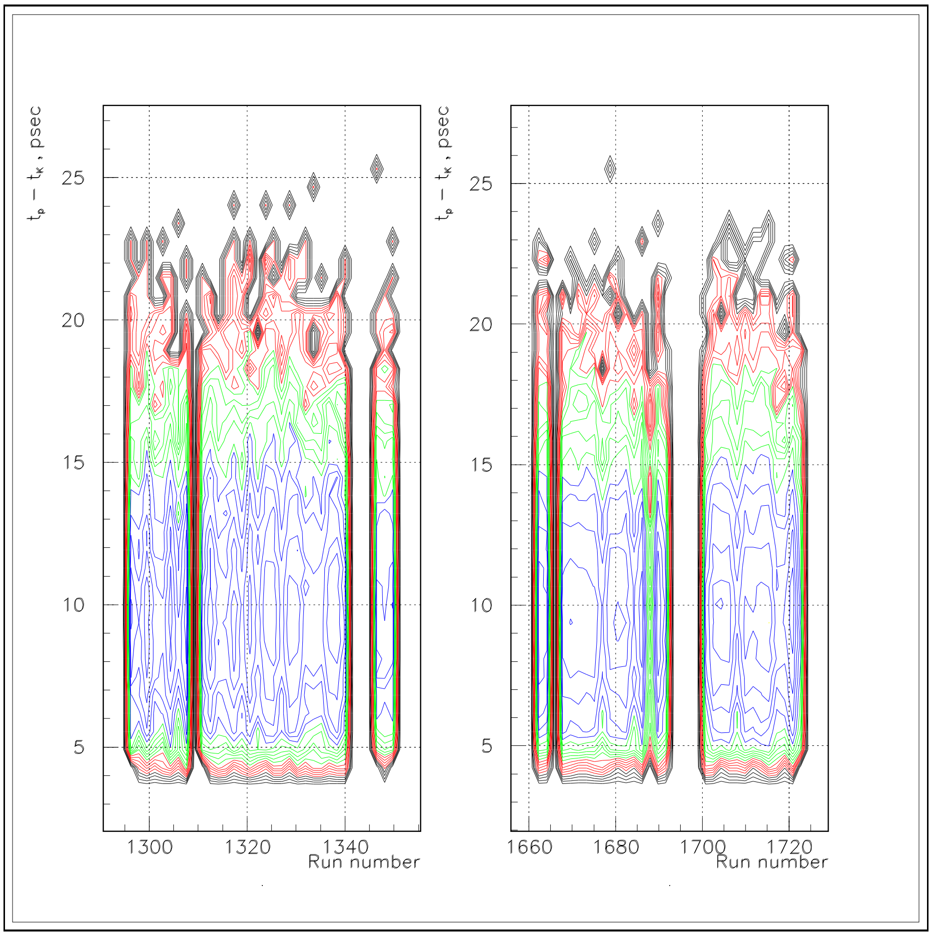

Figure 4.1: Stability of the time-of-flight measurement : the distribution of the calibrated TOF difference (TDC counts) between p and K remains constant throughout the running period

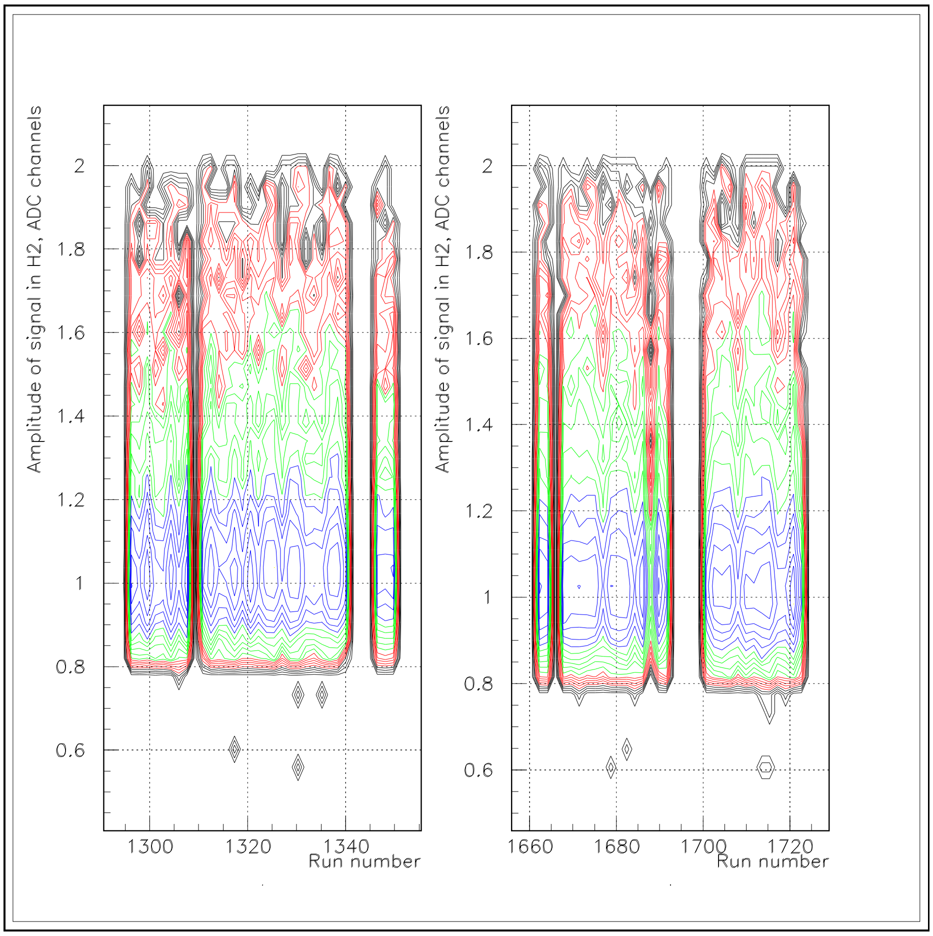

Figure 4.2: Stability of the dE/dx measurement : calibrated ADC response of Hodoscope #2 (normalized units) remains constant throughout the running period

S+Pb running, and ≈ 0.1 during p+Pb running [5]. The question of multiple occupancy of pads and the way the silicon detector data were treated will be discussed later in this chapter.

The calibrations were rather straightforward and included gain equalization of all channels and subtraction of the ADC pedestal that was determined by a fitting procedure.

4.4 Analysis

4.4.1 The Data Summary Tapes Production

The Flow Of Data in the Off-Line Analysis

The flow of data in the off-line analysis is presented in Fig. 4.3. Having obtained "raw" data and a complete set of calibrations, one can further use an off-line program to create a reduced data sample, free of some more obvious types of background, that contains information in a format that is easy to understand and use, for example, the momenta of particles in GeV/c, calibrated time of flight, xyz position of tracks in various parts of the detector in centimeters etc. In our case, we were selecting a class of events with two successfully reconstructed tracks. For historical reasons, such data sample is called *DST*, for Data Summary Tape, and the software used to create it is routinely referred to as "DST program".

One of the principal functions of the DST program is to perform the track

[5] the charged particle multiplicity depends on the trigger conditions (as discussed in chapter 3) and the projectile–target system

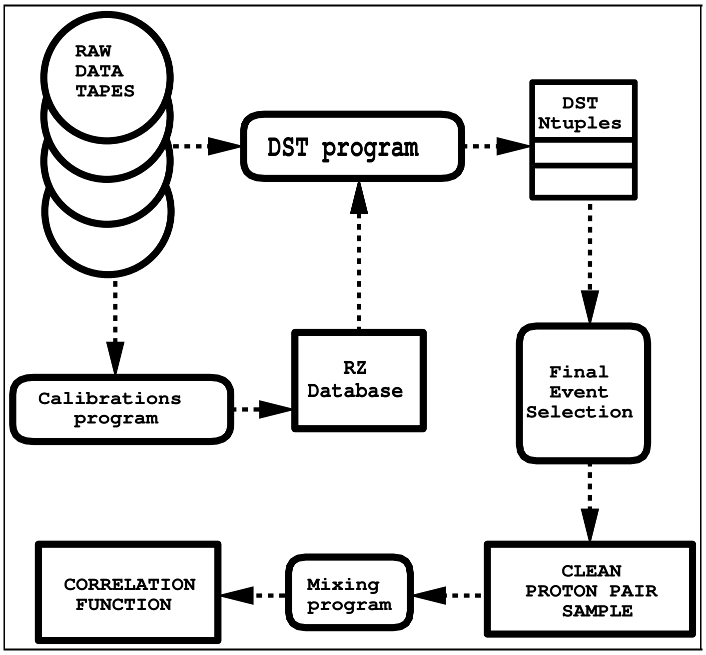

Figure 4.3: Data flow in the NA44 proton correlation analysis

reconstruction, i.e. to establish the presence of valid tracks in the recorded data and their respective momenta. Because of the importance of that procedure we will discuss it now in detail.

Momentum Reconstruction

The particle momenta are calculated based on the xyz coordinates of the hits in all three hodoscope planes. The x and z coordinates are defined by position of the hit slats, and y is calculated from the timing information coming from the top and bottom PM tubes:

$$y = y_{gain} \times (TDC_{bot} - TDC_{top} + y_{offset})$$

Due to the focusing properties of the magnets, it is impossible to limit the pattern recognition procedure to just projection of candidate tracks onto the target. Instead, it is done in the following way: The passage of charged particles through the detector is simulated using `TURTLE` package [42], initially designed for magnetic beam transport systems.[6]

This software takes into account effects of non-linearities and aberrations in the magnetic fields. Based on the known field maps of all the magnets, `TURTLE` propagates a charged particle through the spectrometer, keeping track of the hit positions. With sufficient statistics, it is possible to create a list of all valid slat combinations that a track may hit (many of the $50 \times 60 \times 50$ possible combinations of hits are not permissible due to the geometry of the apparatus)[7], and one ends up with a slat coincidence matrix. Also, based on the momenta and coordinates of the simulated tracks, the measured momentum is parametrized as a polynomial in xyz coordinates of the hits.

During analysis of the data, the reconstruction program sweeps through the acceptance and registers slat hits with ADC values above a threshold. Then it checks if the hits form valid combinations, via a lookup mechanism based on the slat coincidence matrix, and evaluates compatibility of hits in terms of their y coordinates. For each combination of hits thus formed, a straight-line fit is made and a χ^2 cut is applied, effectively eliminating wrong combinations. According-

[6] reflection of the fact that NA44 magnet system is similar to a typical beam line

[7] when a particle leaves the magnet system of the detector and is being measured by the hodoscopes, its trajectory is straight (see Fig. 3.2)

ing to the fitted track positions, momenta are calculated, using the polynomial parametrization obtained as explained above.

As is often the case when measuring pairs of particles with low relative momentum, there is a certain difficulty in resolving nearby tracks. As explained in chapter 3, hodoscope #1 was positioned at a sharp angle with respect to the optical axis of the spectrometer, meaning that it was possible (and in fact, very likely) that a track would hit not just one but two adjacent slats (see a schematic illustration in Fig. 4.4).

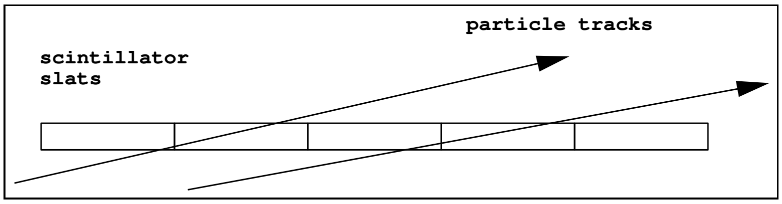

Figure 4.4: A schematic representation of tracks crossing Hodoscope 1

Since calibrated ADC information was available, it could be used to reduce the coordinate measurement uncertainty by weighing the position of the track according to dE/dx deposited in the adjacent hit slats, thus actually improving the momentum measurement accuracy. The grouping and weighing of the ADC signals in the NA44 tracking software is often referred to as "clustering algorithm". However, this procedure leads to a loss of accuracy when two tracks are sharing a slat[8]. It is easy to see that this is possible when the tracks are passing through two

[8] apart from loosing the spatial measurement accuracy, the pulse height information is distorted and affects the slewing correction important for the time-of-flight measurement; the primary timing itself is also affected [35]

adjacent slats in Hodoscope 1. We decided to exclude such events from the final data sample, and the corresponding cut is referred to in the text as the "slat cut" (section 4.4.2). The cut was implemented at the point when the DST Ntuples were converted into the final proton pair sample.

Since there is a correlation between the spatial separation of tracks and their relative momentum, such cut inevitably leads to a lower overall reconstruction efficiency for pairs with low q_{inv}. However, the Correlation Function is defined in such a way that this effect effectively cancels out (see section 2.2.1) since the incurred inefficiency affects the 'real' and 'background' spectra in the same manner. This has been confirmed by a number of Monte Carlo studies.

Slat cut in hodoscopes 2 and 3, defined as rejection of tracks passing through *the same slat* was implemented essentially at the stage of tracks reconstruction, as the lookup mechanism wouldn't recognize such a pattern.

The Performance of the NA44 Tracking System

Since the goal of the measurement that we are considering is determination of the identified particles' momenta, we need to discuss the performance of the NA44 tracking system. To this end, we studied, by means of a Monte Carlo calculation, tracking characteristics such as single particle momentum resolution, resolution in q_{inv} and efficiency of pair reconstruction. In Fig. 4.5 we present distributions of the difference between the reconstructed and "true" (Monte Carlo) values of the particles momenta and their components[9]; the width of such distributions is the essential characteristic of the single-particle performance of the tracking system. As a straightforward estimate, we fitted these histograms with gaussian curves, as can be seen in Fig. 4.5, and list the corresponding σ's in table 4.2.

Another relevant value, and more immediately connected with our correlation

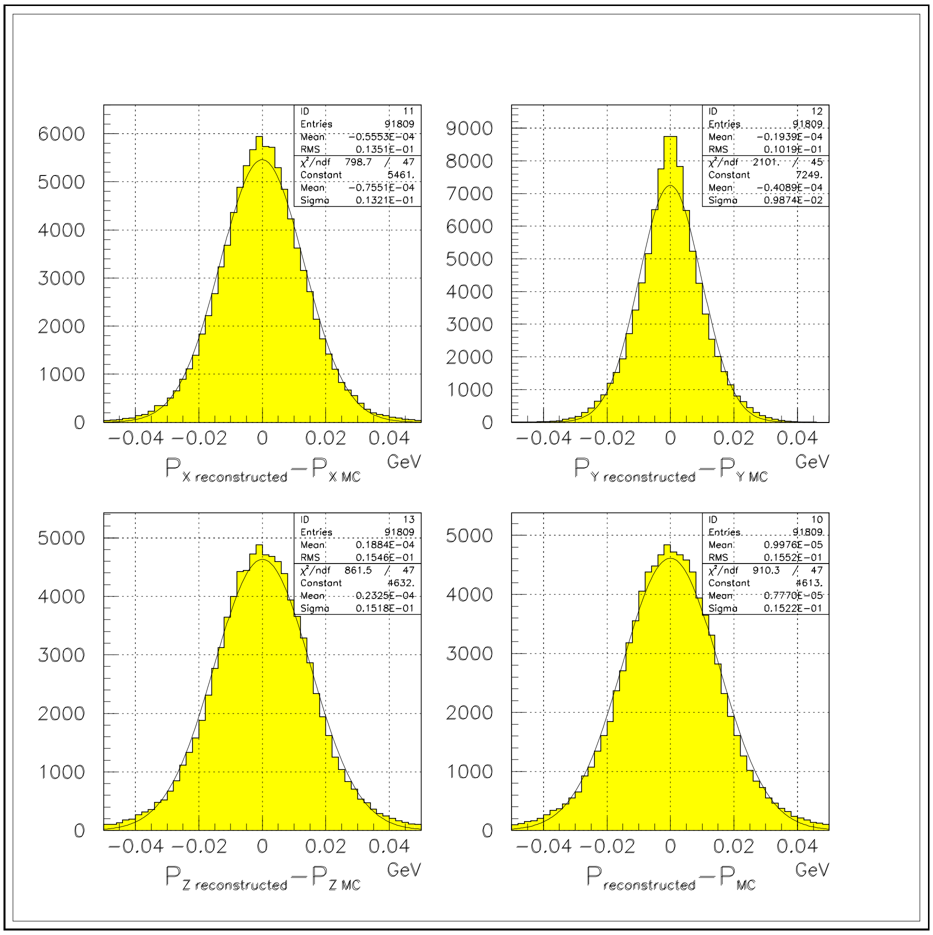

Figure 4.5: Single particle tracking performance: variation of the reconstructed momenta and their components with respect to their "true" MC values (assuming 5 mm Pb target)

[9] in this particular calculation we assumed a Pb target of 5 mm thickness – like the one actually used in the S+Pb measurements

Table 4.2: Single Particle Tracking Performance: σ's of the Reconstructed Momenta, in MeV (assuming 5 mm Pb target)

$\sigma(p_x^{rec} - p_x^{MC})$	$\sigma(p_y^{rec} - p_y^{MC})$	$\sigma(p_z^{rec} - p_z^{MC})$	$\sigma(p^{rec} - p^{MC})$
13.2	9.9	15.1	15.2

study, is the resolution of the apparatus in terms of q_{inv}. The distribution of $q_{inv}^{reconstructed} - q_{inv}^{MC}$ is shown in Fig. 4.6, with corresponding $\sigma(q_{inv}^{reconstructed} - q_{inv}^{MC}) = 7.1MeV$. It obvious from this curve that its shape is not quite gaussian (hence the fit is not a good one), however, here it only serves to illustrate the scale of the momentum resolution and the need to carefully take it into account – the q_{inv} scale of important features of the proton correlation function that we are studying is $\approx 20MeV$ (see chapter 2). As will be explained in chapter 5, a detailed Monte Carlo calculation was performed for that purpose, without any gaussian parametrization. In Fig. 4.7 we plot the efficiency of the pair reconstruction as a function of q_{inv} of the pair, as calculated in Monte Carlo (the solid line, which is a polynomial fit, is to guide the eye). We conclude that the pair detection efficiency is adequate for the purposes of this study.

During the experiment, there are sources of ionizing particles present in the immediate vicinity of the detector (such as the beam dump, see chapter 3) that cause "random" signals to be registered in the hodoscopes. These random hits can, in principle, combine in such a way that the pattern recognition program reconstructs a "fake" track that actually didn't exist. However, a Monte Carlo study based on actual random hit patterns showed that fraction of events with

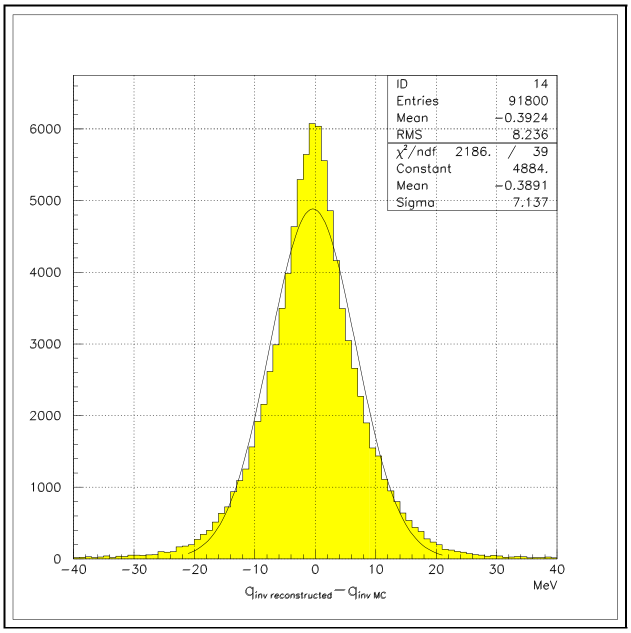

Figure 4.6: Two-Particle Tracking Performance: variation of the reconstructed q_{inv} with respect to its "true" (MC) value

"fake" tracks is quite negligible[10].

Contents of the DST

Events that have hodoscope hit combinations not allowed by the optics of the apparatus are effectively rejected at the stage of momentum reconstruction. Also eliminated are events that have the dE/dx signal values that are likely to be caused by background particles [11]. Such background hits may be due to either slow neutrons leaking from the shielding, producing low-amplitude signal in the hodoscopes, or multiple hits in one slat, causing large signals.

[10] even without the time-of-flight cuts the probability of reconstruction of such a track is at about 1% level; without any doubt, the TOF cuts will make this number vanishingly small

[11] "good tracks", on the other hand, are essentially Minimum Ionizing Particles (*MIPs*), therefore we require the ADC signal to be consistent with a *MIP*

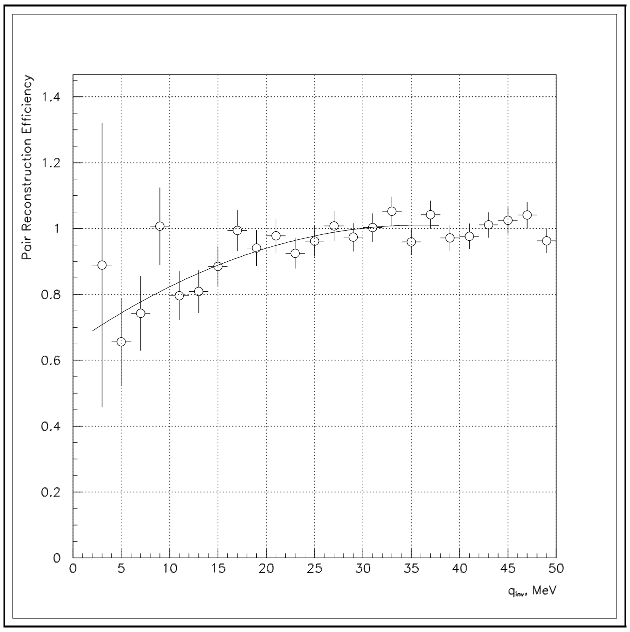

Figure 4.7: Two-Particle Tracking Performance: the efficiency of the pair reconstruction (MC) as a function of q_{inv} (errors are statistical, the solid line is a polynomial fit)

The volume of information in the DST is reduced roughly by a factor of 60 to 70 as compared to the raw data tape. The output data stream contains the following items relevant to the analysis presented here (we will discuss them in more detail in section 4.4.2):

- The reconstructed momenta of the two tracks
- χ^2 fit values of the tracks
- Indices of the hit slats
- Coordinates of tracks on the hodoscope planes
- Time-Of-Flight for each track
- dE/dx signal for each track, in ADC counts, in all 3 hodoscopes
- ADC counts in Čerenkov and all of the Target Area counters
- Information from the Silicon Detector (number of hit pads)

The DST data format is Ntuple [43] that allows to use the interactive `PAW` package to examine data from individual detector subsystems, possible correlations in such data, and set forth criteria ("cuts") that later are used to obtain the final clean sample of proton pair events. As will be explained in the following section, this final selection was done by means of a standalone `FORTRAN` program.

4.4.2 Event Selection

At this point the data is further reduced, from the DST set of events with two successfully reconstructed tracks, to the actual *proton pair* sample. The criteria ("cuts") applied at this stage of selection can be logically subdivided in two categories:

1. Cuts that reject pile-up events and various other sources of "trivial" background
2. *Particle Identification Cut*, whose primary mission is to separate protons from kaons, although it also acts as a filter against other sources of background

The latter is very important and more complex than other cuts and will be discussed in detail in section 4.4.3. The cuts from the first group, with a brief explanation of their purpose, are listed in tables 4.3 and 4.4, for the S+Pb and p+Pb data. Their application, for the S+Pb sample, is illustrated in Fig. 4.8. In particular, we can see how by establishing cuts on the amplitude of the Čerenkov and beam counter signals[12] we reject events in the tail of the distribution, that are essentially pile-up events [13], where a second interaction in the target happened during the ADC gate. Peaks corresponding to multiple particles in the Beam Counter distribution are also clearly seen, and such events are also rejected on

[12] that are equal, respectively, to 70 and 210 ADC channels – see table 4.3 for details

[13] note that in this measurement, these counters were used in the trigger in veto mode, so "good" events simply can't have large amplitude Čerenkov signals

similar grounds. In these plots, the limits on each value are represented by solid a vertical line and an arrow.

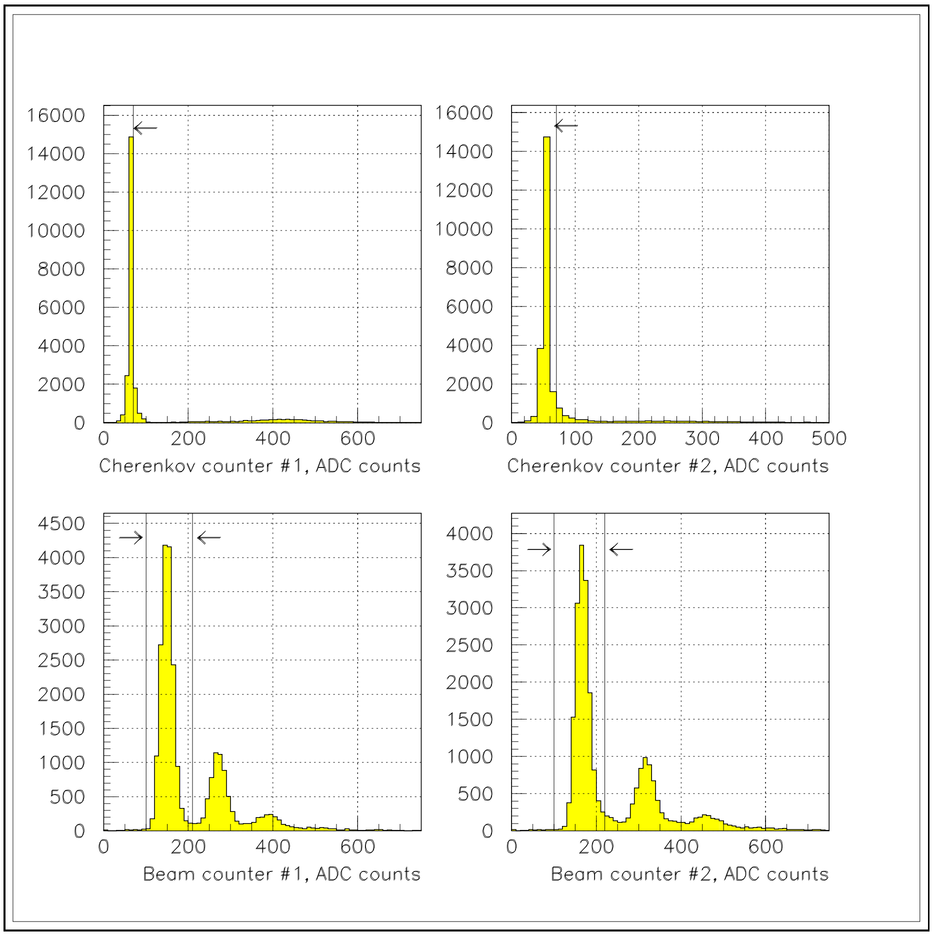

Figure 4.8: Čerenkov and Beam Counters spectra, from the DST data, with corresponding cuts (S+Pb data)

The "slat cut" has to do with the way the tracking software worked and is explained in section 4.4.1.

Table 4.3: Cuts Applied to the S+Pb Data

Type of Cut	Limits	Purpose
$\check{C}_1$	<70	Rejection of e,π and double beam
$\check{C}_2$	<70	– " –
Difference in timing between top and bottom channels of T0	< 10	Selection of events with correct timing
Beam Counter #1	$>100,<210$	Rejection of double beam events
Beam Counter #2	$>100,<220$	– " –
Beam Counter Veto #1	<120	Rejection of beam halo
Beam Counter Veto #2	<100	– " –
Hit Multiplicity in the Hodoscopes	$=2$	Rejection of events with spurious hits
Normalized ADC signal amplitude in Hodoscope #1	$>0.90,<2.20$	Rejection of events with spurious hits
Normalized ADC signal amplitude in Hodoscope #2	$>0.85,<1.40$	– " –
Normalized ADC signal amplitude in Hodoscope #3	$>0.95,<1.40$	– " –
Mass-Squared (particle #1), GeV^2	$>0.60,<1.20$	Particle ID (see text for details)
Mass-Squared (particle #2), GeV^2	$>0.75,<1.20$	Particle ID (see text for details)
"Slat cut" in H1	$\Delta slat > 1$	To remove tracking ambiguity
"Slat cut" in H2	$\Delta slat > 0$	– " –
"Slat cut" in H3	$\Delta slat > 0$	– " –

Table 4.4: Cuts Applied to the p+Pb Data

Type of Cut	Limits	Purpose
$\check{C}_1$	<70	Rejection of e,π and double beam
$\check{C}_2$	<70	– ” –
Difference in timing between top and bottom channels of T0	$> -20, < -2$	Selection of events with correct timing
Beam Counter Veto #1	<100	Rejection of beam halo
Beam Counter Veto #2	<100	– ” –
Hit Multiplicity in the Hodoscopes	=2	Rejection of events with spurious hits
Normalized ADC signal amplitude in Hodoscope #1	>0.90,<2.20	Rejection of events with spurious hits
Normalized ADC signal amplitude in Hodoscope #2	>0.85,<1.40	– ” –
Normalized ADC signal amplitude in Hodoscope #3	>0.95,<1.40	– ” –
Mass-Squared (particle #1), GeV^2	>0.68,<1.25	Particle ID (see text for details)
Mass-Squared (particle #2), GeV^2	>0.72,<1.25	Particle ID (see text for details)
“Slat cut” in H1	$\Delta slat > 1$	To remove tracking ambiguity
“Slat cut” in H2	$\Delta slat > 0$	– ” –
“Slat cut” in H3	$\Delta slat > 0$	– ” –

4.4.3 The Particle Identification Cut

The Efficiency and the Kaon Rejection Power of the Cut

As already discussed in section 3.4.1, two Čerenkov counters of the NA44 detector played an important role in the particle identification scheme. They were incorporated in the trigger logic in veto mode, essentially eliminating all particles lighter than kaons [35]. Time-of-flight (TOF) measurement is the principal tool to provide additional particle identification and to allow efficient separation of heavier particles. In the case we are interested in, we must separate protons and kaons, which are present in the DST data in roughly equal proportion. To do this, we calculate the value of the square of mass of the particle based on the known particle momentum and β, that is defined by the time-of-flight over the known flight path, using

$$p = m\beta\gamma \longrightarrow m^2 = \frac{p^2}{\gamma^2\beta^2} \longrightarrow m^2 = p^2(\frac{t^2c^2}{z^2} - 1) \tag{4.1}$$

where m is the mass, p is the momentum, t is the measured time of flight, and z is the known flight path (obviously, $\beta = z/tc$). The question of accuracy of such measurement is rather important; propagation of errors [35] gives

$$(\Delta m^2)^2 = 4p^2(\frac{1}{\beta^4}(\frac{\Delta t}{t})^2 + \frac{1}{\beta^4}(\frac{\Delta z}{z})^2 + (\frac{1}{\beta^2} - 1)^2(\frac{\Delta p}{p})^2) \tag{4.2}$$

Analysis of the factors in the above formula that contribute to the m^2 resolution indicates that $\Delta t/t$ is the main source of error. It is because of the finite time resolution that we chose to consider m^2 and not m itself (which can be negative).

The actual conversion between the time-of-flight and m^2 (S+Pb data), using equation 4.1, is illustrated by Fig. 4.9. The m^2 distributions for S+Pb and p+Pb

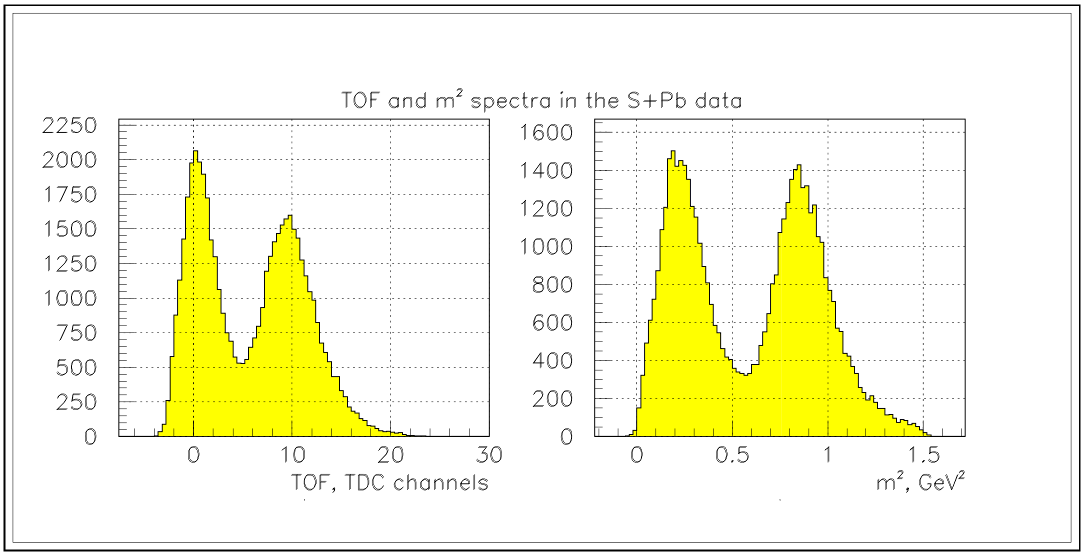

Figure 4.9: Conversion of the Time-Of-Flight to m^2 in S+Pb data

data are presented in Fig. 4.10 and Fig. 4.11.

There are two peaks, corresponding to kaons and protons [14]; there are virtually no pions in this data sample since, as already mentioned, they were vetoed in the trigger (and in the off-line analysis) based on the signals from the Čerenkov detectors. As can be seen, the peaks in the p+Pb distribution are somewhat broader due to a worse time resolution of the T0 counter that was used to generate the start signal for the time-of-flight system when running with proton beams.

[14] according to PDG, m_K^2=0.244 GeV^2 and m_p^2=0.879 GeV^2. Typical fitted positions of the peaks in our measurements are in the range 0.20-0.30 and 0.84-0.90 GeV^2, respectively; this spread includes a systematic difference between p+Pb and S+Pb running periods that was due to slight variations in the TOF calibration. As we will see, however, we only concern ourselves with *separation* of the p and K peaks and not with their absolute position on the m^2 scale.

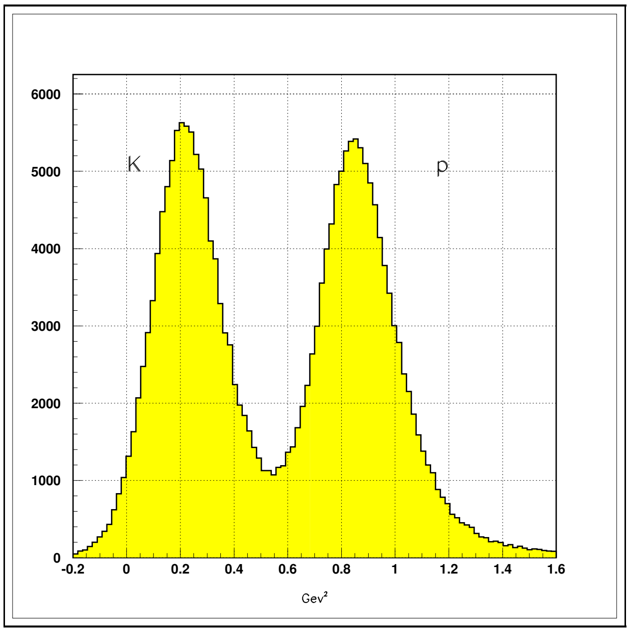

Figure 4.10: The Square of Mass distribution in the pre-selected K and p sample, S+Pb data.

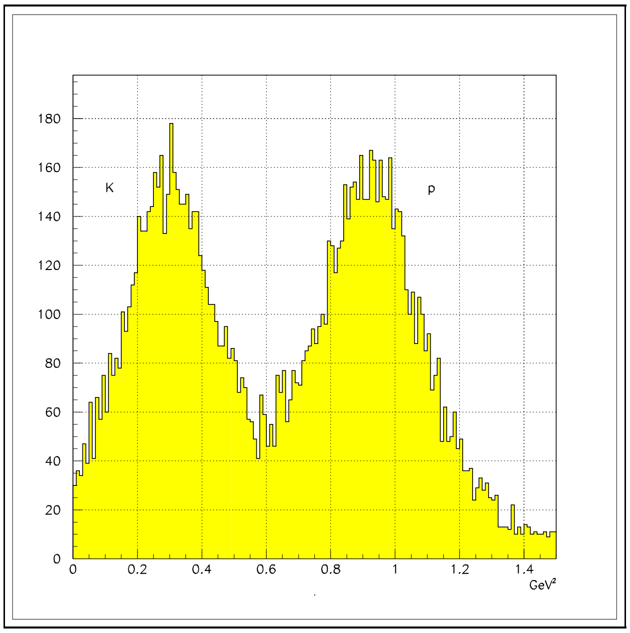

Figure 4.11: The Square of Mass distribution in the pre-selected K and p sample, p+Pb data.

Imposing a requirement (cut) on the m^2 value effectively constitutes particle selection. To make a sensible cut we should attempt to determine how the efficiency of proton selection and contamination by kaons depend on the m^2 threshold (in other words, the rejection power of the cut). This has been done by fitting this distribution with a sum of gaussian curves (in one case three gaussians were needed to obtain a good fit; we note that there is no a priori reason for any of these peaks to be exactly gaussian, so the procedure is more like parametrization), and then studying the relative area of the proton peak and its overlap with the kaon peak. The results of this exercise are shown in Figs. 4.12 and 4.13 for the S+Pb data and in Figs. 4.14 and 4.15 for p+Pb. For a given m^2 cut value we can thus estimate

1. the abundance of protons in the selected sample, relative to kaons

2. the fraction of particles that survive the cut

As was the case with other NA44 data samples (in particular, HBT studies with pion and kaon pairs), we chose to keep contamination of the pp sample by Kp and KK pairs at $\approx$ %1 level. On the one hand, it allows us to keep 80 to 90% of the pairs and thus provide reasonable statistics, on the other hand, as we will discuss in chapter 5, this kaon contamination is small compared to other sources of systematic uncertainty in this measurement[15]. Note that there are two sets of curves, for particle 1 and 2. This numbering is, of course, arbitrary, and has to do

[15]the accepted values for the m^2 cut can be found in tables 4.3 and 4.4

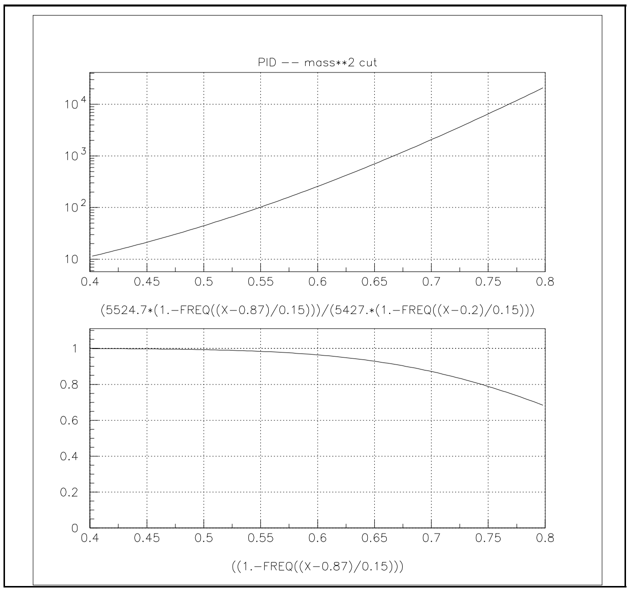

Figure 4.12: p/K ratio and p efficiency as functions of the m^2 cut, particle 1,S+Pb data; the chosen cut is 0.60 GeV^2

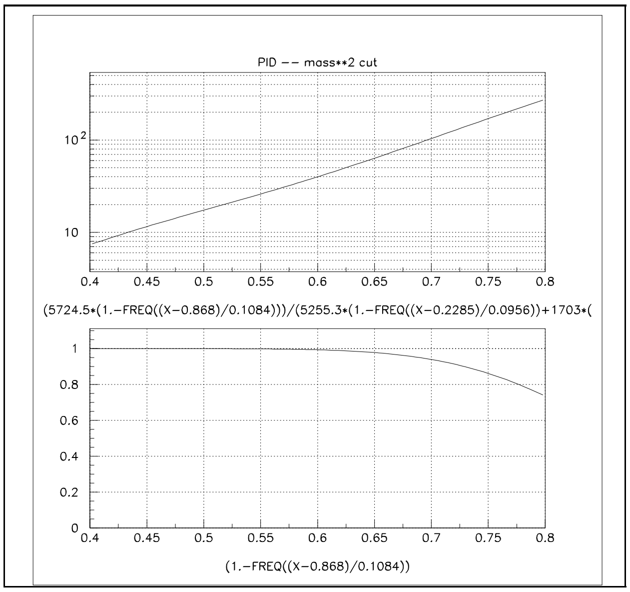

Figure 4.13: p/K ratio and p efficiency as functions of the m^2 cut, particle 2,S+Pb data; the chosen cut is 0.75 GeV^2

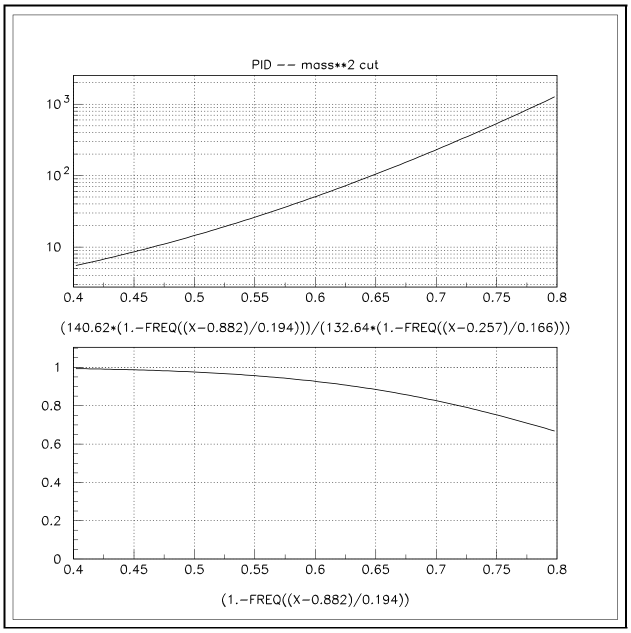

Figure 4.14: p/K ratio and p efficiency as functions of the m^2 cut, particle 1, p+Pb data; the chosen cut is 0.68 GeV^2

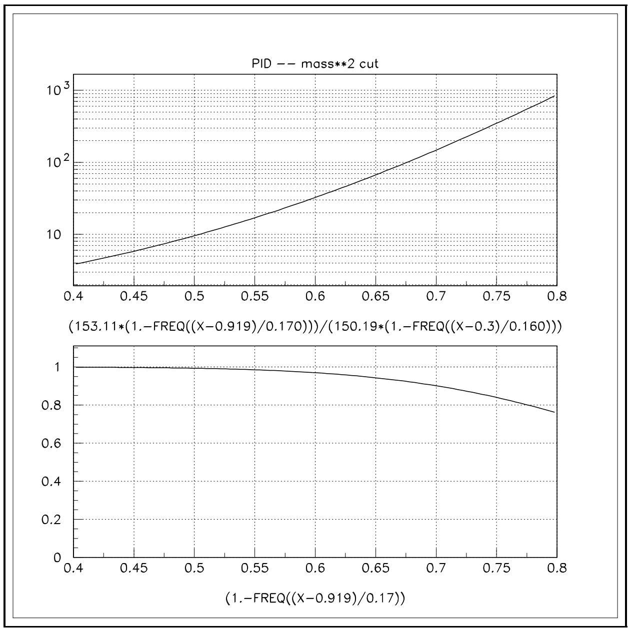

Figure 4.15: p/K ratio and p efficiency as functions of the m^2 cut, particle 2, p+Pb data; the chosen cut is 0.72 GeV^2

with the way the tracking software works – track 1 is picked first and in general has higher momentum. Difference in the momenta means that the shapes of the m^2 distributions are different and we can optimize the PID by using slightly different values of the m^2 cut for particles 1 and 2. For example, as can be seen from the presented curves for S+Pb, cutting at 0.60 GeV^2 for particle 1 provides 3×10^2 p/K ratio and efficiency of 95%. For particle 2 we chose to put our threshold at 0.75 GeV^2, corresponding to $p/K \approx 2 \times 10^2$. We conservatively state that contamination of the final proton pair sample by pK pairs is at levels of about 1% or less.

This procedure was repeated for the p+Pb data sample (for m^2 spectra see Fig. 4.11). The m^2 resolution for these data, as can be seen, is somewhat worse, due to less precise timing of the T0 counter.

Two final comments on the PID cut seem in order. As we already mentioned, there was a small difference in the absolute scale of the m^2 spectra of the S+Pb and p+Pb data – this should be kept in mind when comparing the efficiency and rejection curves presented above. Also, the method used to produce this curves has its limitations: the shape of *the tails* of the m^2 distributions might have been somewhat different from the gaussian prescription. Later in this chapter, we will address the issue of the stability of the measured correlation function with respect to the PID cut and demonstrate that the procedure is essentially robust.

4.4.4 Application of the Final Selection Cuts

All the cuts, including the PID, are integrated in a `FORTRAN` routine callable from `PAW`, that is used on the DST Ntuples. The result is a file written in the following format:

1. A tag field containing the run number and the event number, for bookkeeping purposes

2. P_x, P_y, P_z of the two tracks, along with the numbers of slats associated with these tracks

The information about the slat numbers was necessary to keep because we needed to make consistent slat cuts[16] in both *Actual* and *Background* spectra during the construction of the Correlation Function (as explained in the following section).

4.4.5 The Correlation Function

At this point we are ready to construct the Correlation Function itself, and this is done by a standalone `FORTRAN` program in the following way:

1. The file with the track information is read in and a histogram is filled with q_{inv} values

2. The track information is also stored in an internal array

[16] see section 4.4.1

3. The *Background* q_{inv} spectrum is formed using the event mixing technique,[17] whereby two tracks are randomly pulled from the existing array and are treated in exactly same way as the *Actual* pairs. This includes the requirement that the tracks never share slats in hodoscopes 2 and 3, and are separated by at least one slat on H1 ("slat cut", see tables 4.3 and 4.4, and sections 2.2.1 and 4.4.1). The number of such formed *Background* pairs should be much larger than the number of the *Actual* pairs, in order to guarantee that the background does not contribute, in any significant way, to the overall statistical uncertainty of the correlation function; in this particular calculation we generated 10^6 background pairs.

4. The *Actual* q_{inv} spectrum is divided by the *Background*

5. The resulting distribution is multiplied by a normalization factor which is the ratio of the number of events in the *Background* and *Actual*

The results for both S+Pb and p+Pb systems are presented in Figs. 4.16 and 4.17. We defer the discussion of the comparison between the data and predictions of the `RQMD` event generator till chapter 6, and here just comment on general features of the observed correlation curves:

1. Both correlation functions, S+Pb and p+Pb, exhibit an enhancement in the low q_{inv} region, signaling the presence of correlation between two protons emanating from the reaction volume

[17] see section 2.2.1

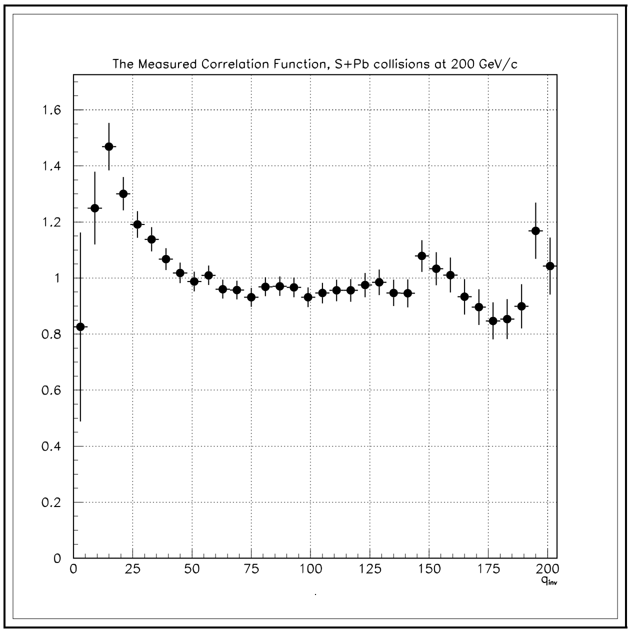

Figure 4.16: Proton Correlation Function, S+Pb collisions at 200 GeV/A (statistical errors only)

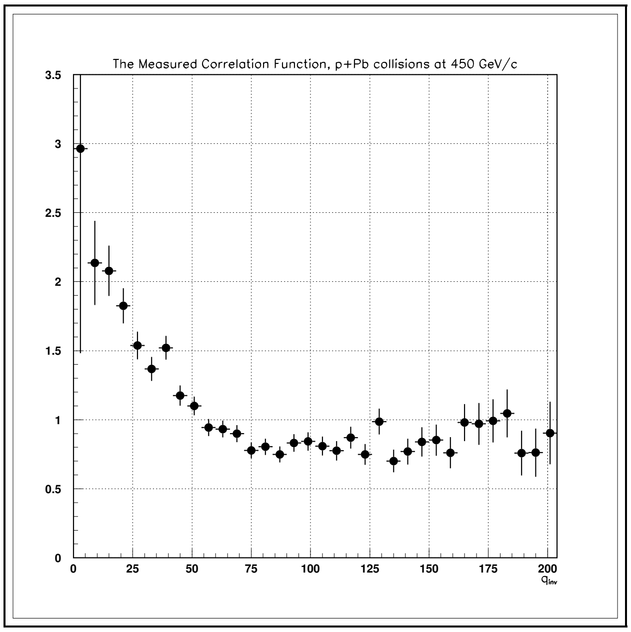

Figure 4.17: Proton Correlation Function, p+Pb collisions at 450 GeV (statistical errors only)

2. Within the statistical errors, both curves are compatible with a maximum (peak) at $q_{inv}\approx$20 MeV (which is expected – see chapter 2 for explanation)

3. The amplitude of the enhancement is larger in case of p+Pb system, which can be interpreted, qualitatively, as an indication of a smaller particle source. That also should be expected based on the geometrical picture of a heavy-ion collision drawn in chapter 2

Based on the behavior of the data points in the high q_{inv} region (120–200 MeV), one might speculate that there appears to be a deviation of the correlation function from the constant asymptotic value. However, a χ^2 analysis confirms that the data points in this region are spread out in a manner consistent with statistical fluctuations.

4.4.6 Stability of the Data with Respect to the Applied Cuts

To assure quality of the data, it is necessary to study its behavior with respect to the cuts applied during the event selection. The general approach was to keep constant all cuts but one, and vary that cut, observing resulting changes in the correlation function. This way we make sure that the data are stable under the cut in question and no artifacts are introduced by applying it. As an example, in Fig. 4.18 we present a comparison of the proton correlation function, constructed with and without the hodoscope hit multiplicity cut, for the S+Pb data. The cut required that there be two and only two hits in each of the three hodoscopes, thus reducing the probability of a background hit being reconstructed. As follows

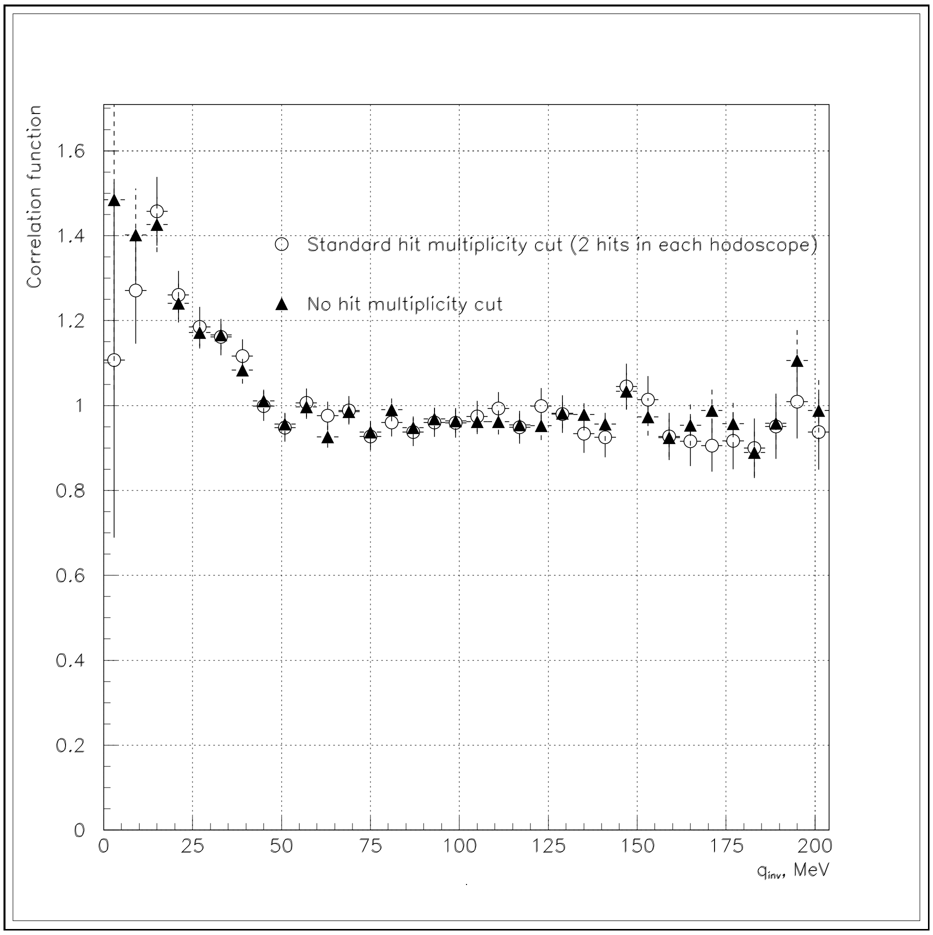

Figure 4.18: Correlation Function (S+Pb) constructed with and without the hodoscope hit multiplicity cut

from that plot, the correlation function is rather stable with respect to this cut: beginning with the third bin in the histogram, the changes in the shape of the curve are much smaller than statistical errors. However, the first two bins exhibit a tendency to decrease under this cut, which is probably due to the fact some background events are rejected when it is applied[18].

Stability of the Data with Respect to the m^2 Cut

The stability of the data with respect to the m^2 cut was checked in the following way: suppose the m^2 cutoff values for particles 1 and 2 are $m_{cutoff1,2}$. Fixing $m_{cutoff2}$ at the "standard" value, we then vary $m_{cutoff1}$ and observe the corresponding changes in the correlation function[19]. The procedure is then repeated with $m_{cutoff1}$ fixed and $m_{cutoff2}$ varying. The margin of variation was chosen such that in either case the estimated level of kaon contamination was changed by a factor of 2, up or down. As can be seen in Figs. 4.19 and 4.20 (S+Pb data) and Figs. 4.21 and 4.22 (p+Pb data), the measured correlation function does not exhibit any systematic shift under such changes of the m^2 cut.

To illustrate the influence of kaon contamination, we have also calculated the correlation function for a data sample with a large, up to 40%, admixture of Kp pairs, obtained by moving $m_{cutoff1}$ down to the appropriate level – see Figs. 4.23 and 4.24.

In general, we expect the correlation function to become more flat as the fraction of the (uncorrelated) Kp pairs in the sample increases, although, of course, the contribution of KK pairs to the enhancement of C(q_{inv}) at low q_{inv} itself becomes non-negligible. In any case, the data behave according to our expectations.

[18] the low q_{inv} bins are most sensitive to background since the number of events (statistics) in these bins is the lowest, hence even a small number of background events would make a difference

[19] all other cuts fixed at their "final" values

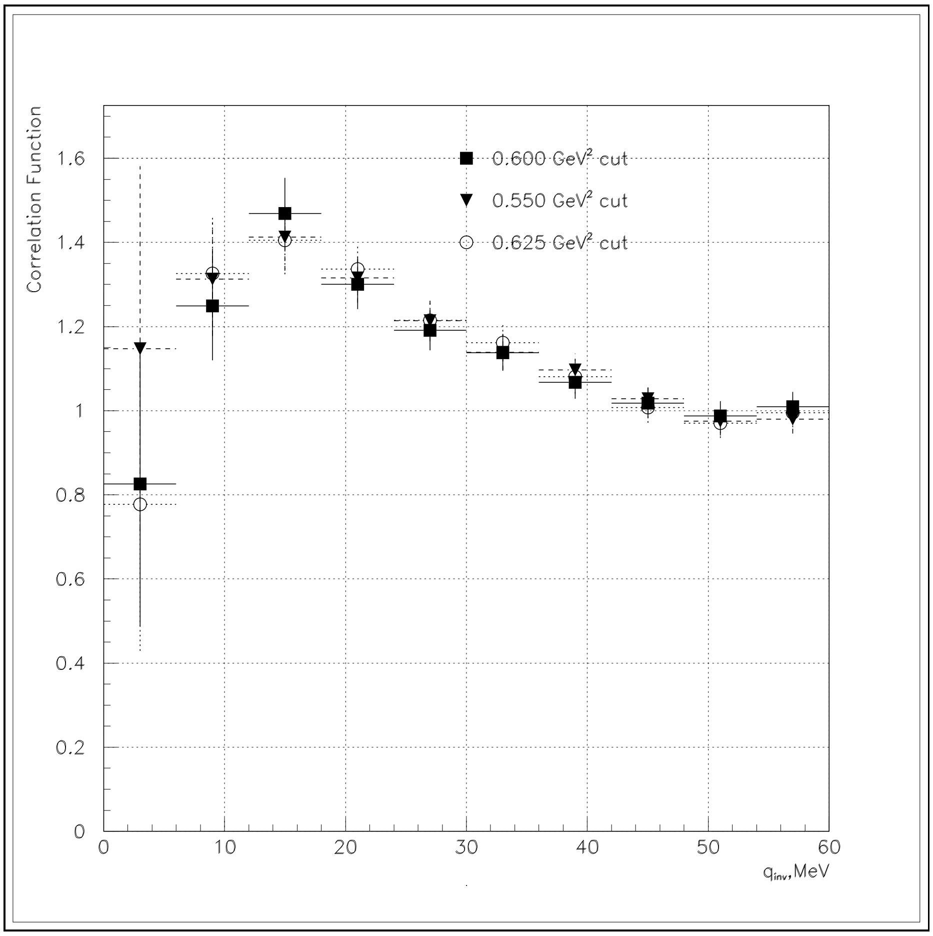

Figure 4.19: The Correlation Function Stability with Respect to the m^2 Cut on Particle 1, S+Pb data. Contamination by Kp pairs is estimated as 1% for 0.600 GeV^2 cutoff, 0.5% for 0.625 GeV^2 and 2% for 0.550

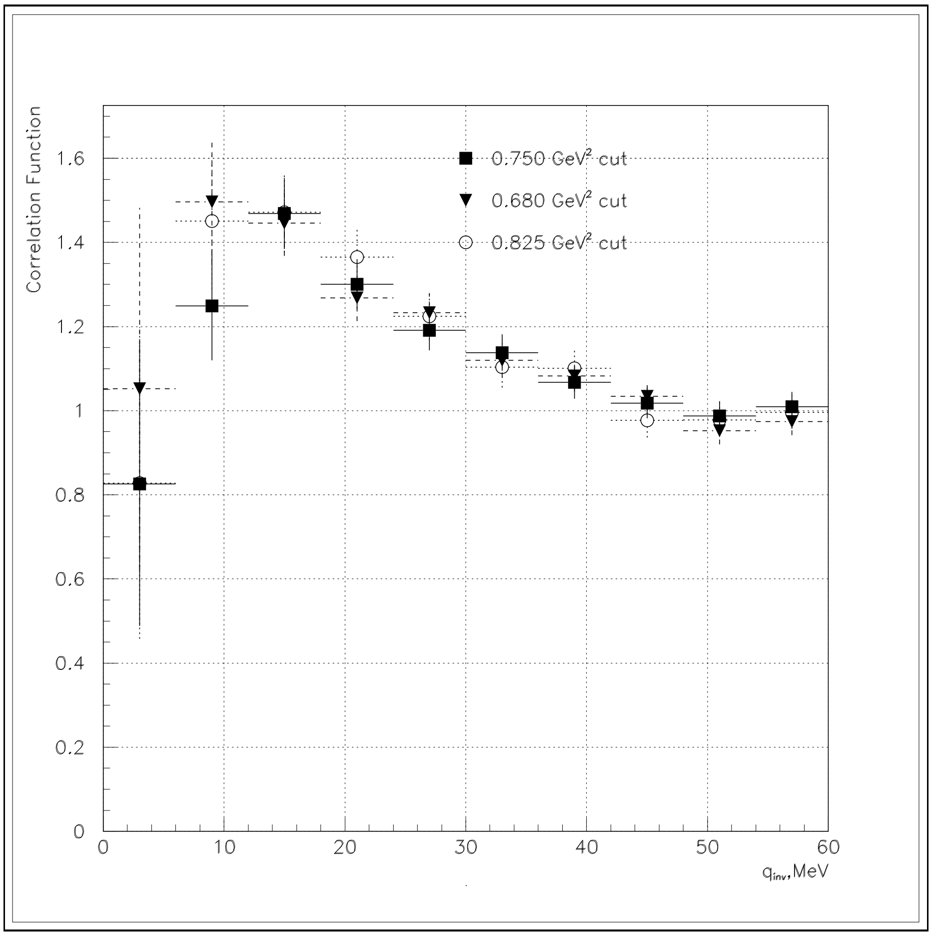

Figure 4.20: The Correlation Function Stability with Respect to the m^2 Cut on Particle 2, S+Pb data. Contamination by Kp pairs is estimated as 1% for 0.750 GeV^2 cutoff, 0.5% for 0.825 GeV^2 and 2% for 0.680

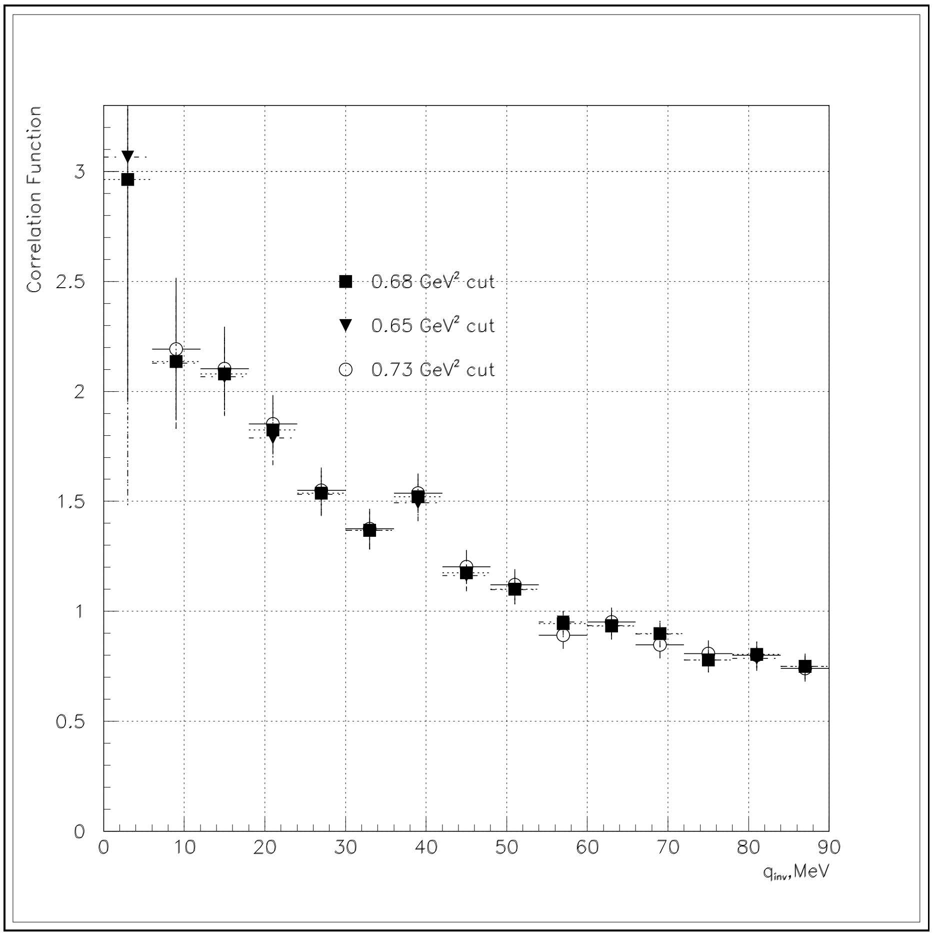

Figure 4.21: The Correlation Function Stability with Respect to the m^2 Cut on Particle 1, p+Pb data. Contamination by Kp pairs is estimated as 1% for 0.68 GeV^2 cutoff, 0.5% for 0.73 GeV^2 and 2% for 0.65

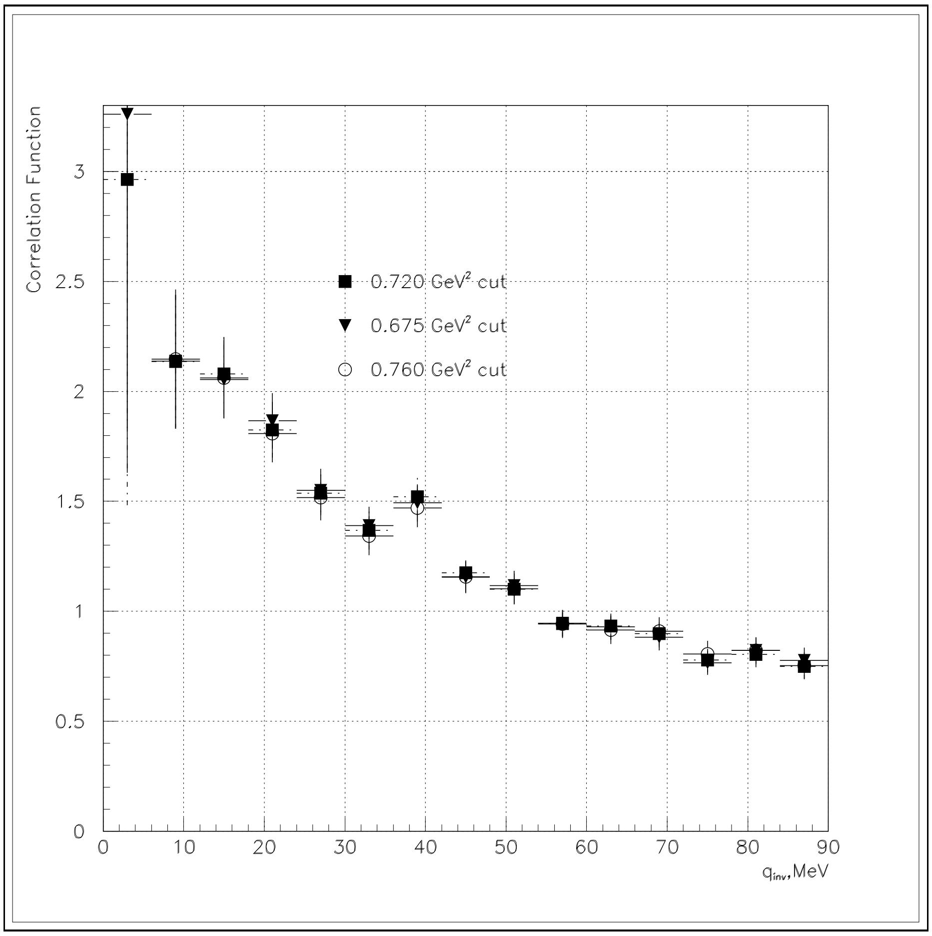

Figure 4.22: The Correlation Function Stability with Respect to the m^2 Cut on Particle 2, p+Pb data. Contamination by Kp pairs is estimated as 1% for 0.720 GeV^2 cutoff, 0.5% for 0.760 GeV^2 and 2% for 0.675

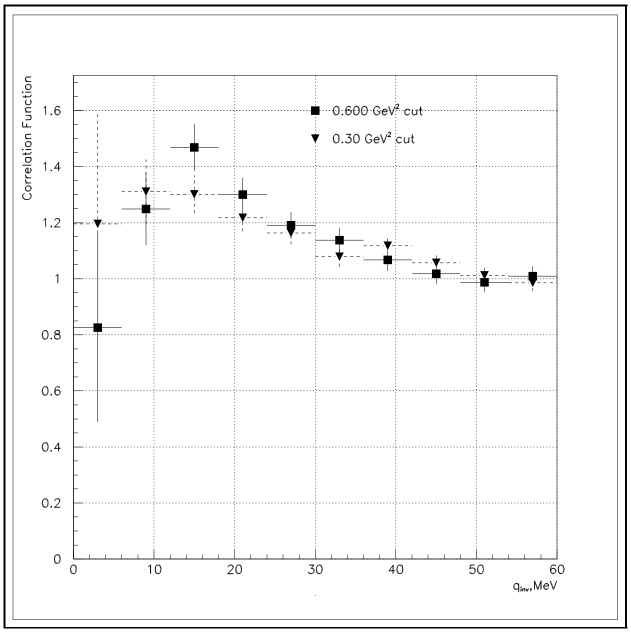

Figure 4.23: Correlation Function for a Data Sample with Large Kaon Contamination, S+Pb data

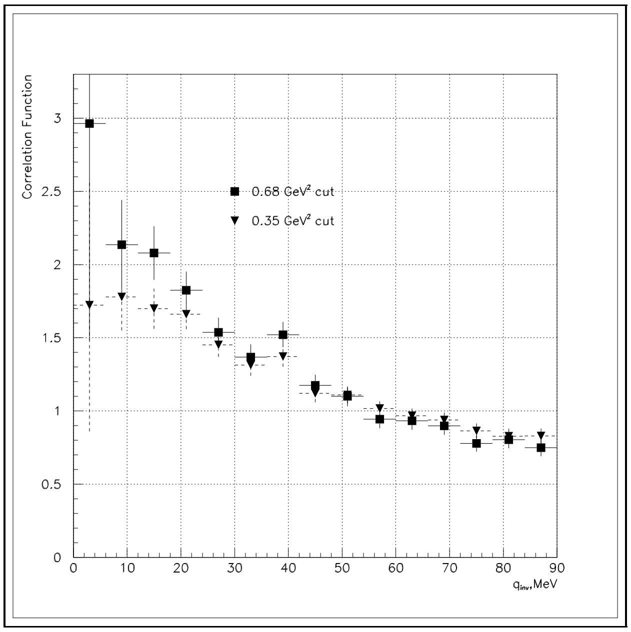

Figure 4.24: Correlation Function for a Data Sample with Large Kaon Contamination, p+Pb data

The Momentum Dependence of the m^2 Cut Efficiency

As already mentioned, the m^2 distributions are momentum dependent (this can be seen in equation 4.2), meaning that in general we can expect somewhat worse TOF resolution for particles with higher momentum. It is rather well illustrated by Figs. 4.25 and 4.26, where we plot the m^2 distributions in different momentum bins, from 5.0 to 7.5 GeV.

It is obvious that for a fixed m_{cutoff} value, due to the different widths of the peaks in these distributions, different fractions of protons will be actually accepted when the m^2 cut is applied. This means that the efficiency of the cut becomes momentum-dependent. This trend is present in both S+Pb and p+Pb data and is illustrated in Figs. 4.27and 4.28, where we plot the efficiency of the m^2 cut as a function of the particle's momentum, for both S+Pb and p+Pb data. To take it into account, we may choose one of two options:

1. Introduce a momentum-dependent m^2 cut, such that its efficiency is independent on the particle's momentum (note that it would mean *variable level of kaon contamination*)

2. Use the m^2 distributions (Figs. 4.25 and 4.26) to actually define the cut efficiency as a function of momentum. This is done in a way similar to the one explained above, by performing gaussian fits of the m^2 distributions in each individual momentum bin and using thus obtained parametrization in

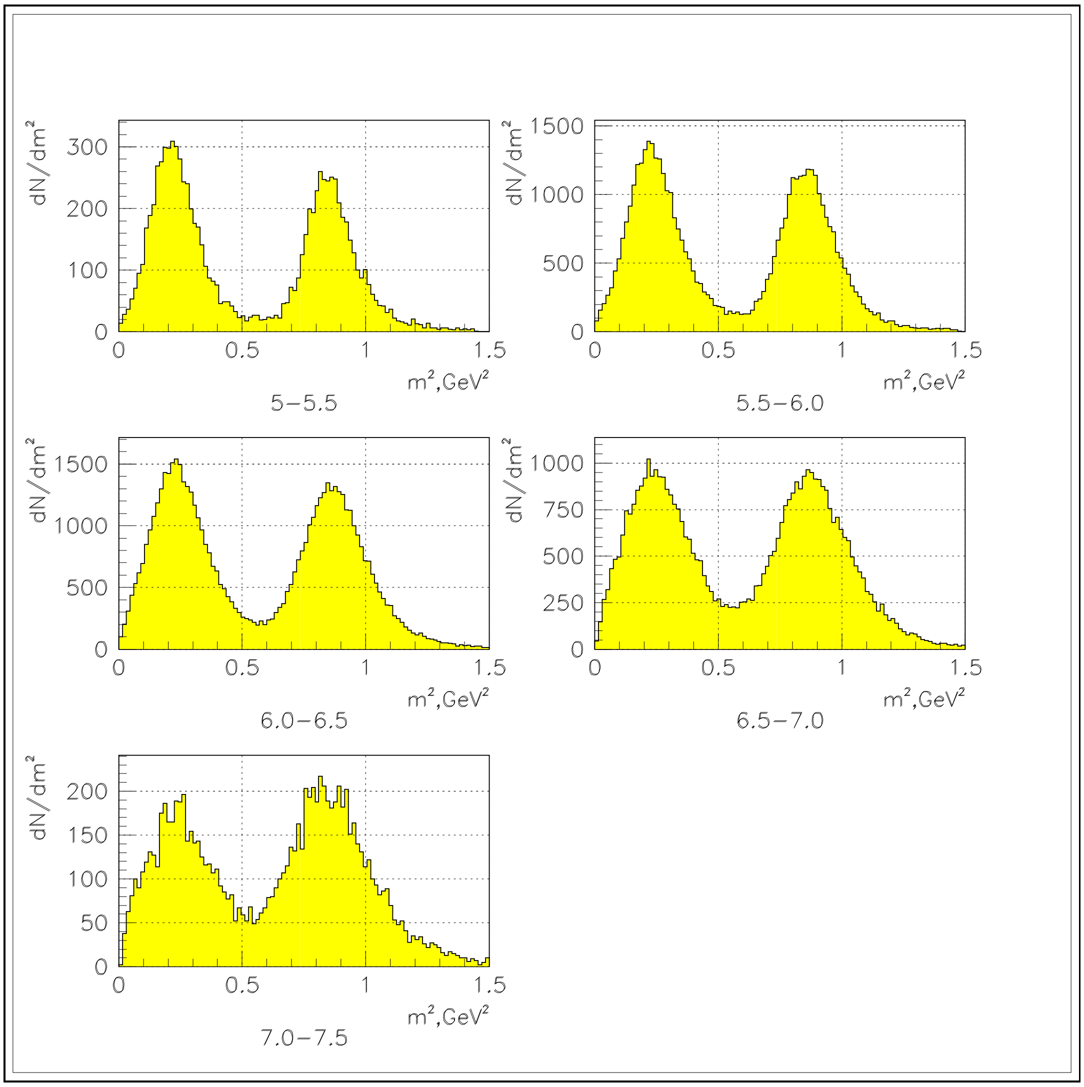

Figure 4.25: Mass-squared distributions in different momentum bins, from 5.0 to 7.5 GeV, S+Pb data (see labels under each plot)

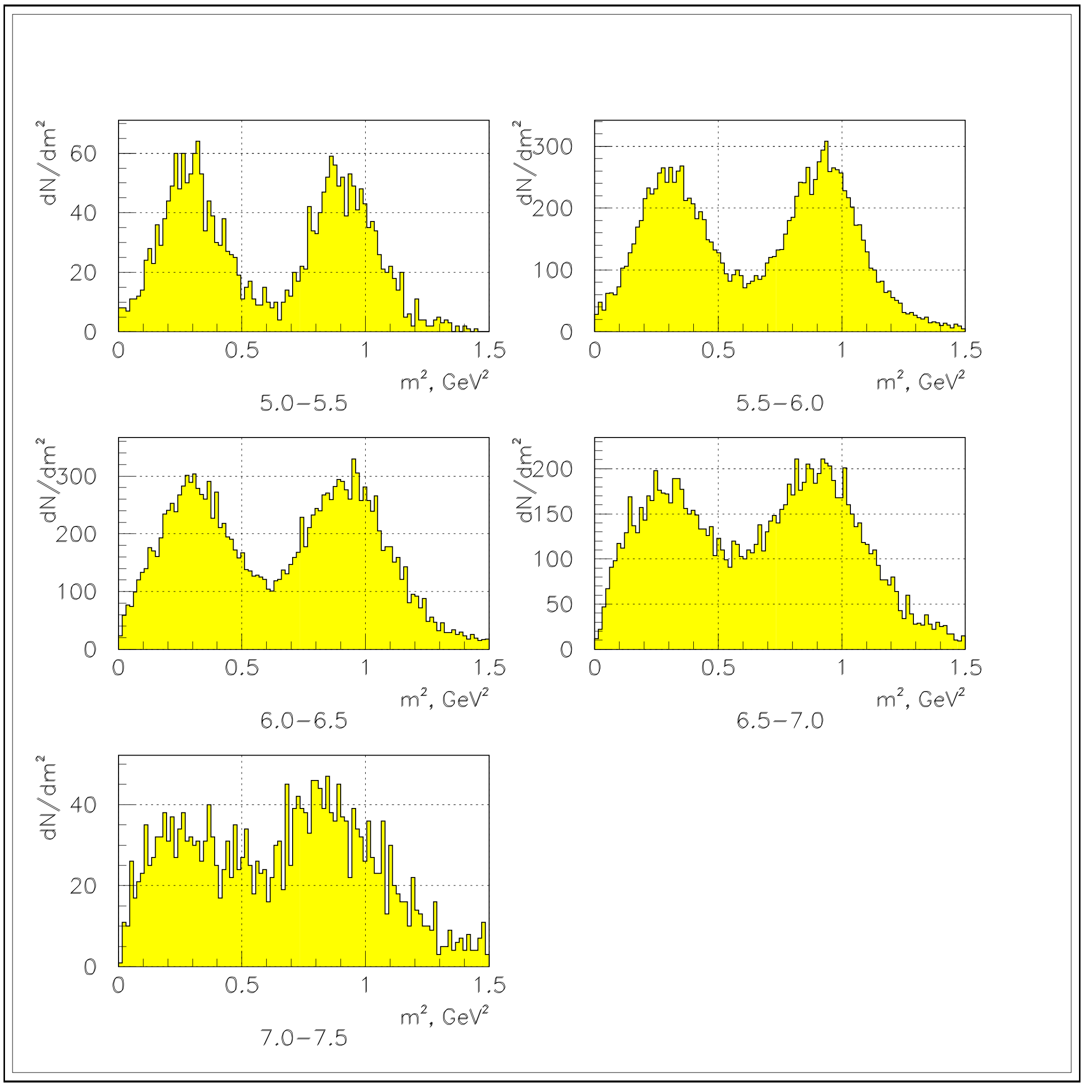

Figure 4.26: Mass-squared distributions in different momentum bins, from 5.0 to 7.5 GeV, p+Pb data (see labels under each plot)

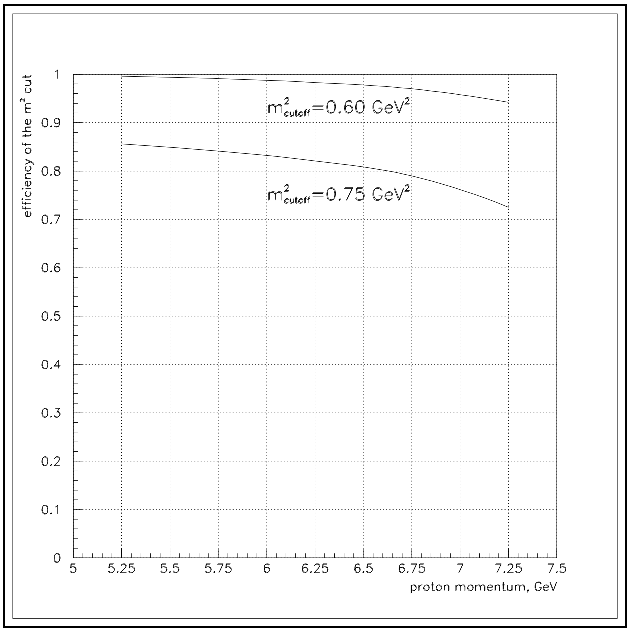

Figure 4.27: Efficiency of the m^2 cut as a function of the particle's momentum, S+Pb data

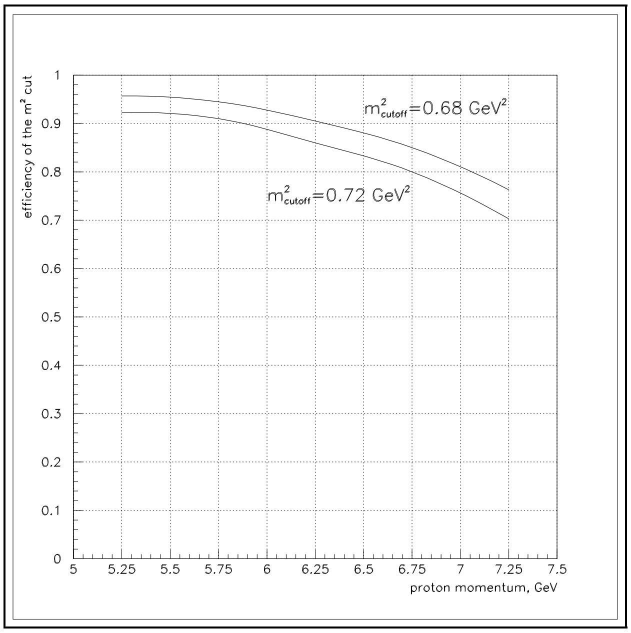

Figure 4.28: Efficiency of the m^2 cut as a function of the particle's momentum, p+Pb data

the Monte Carlo[20], in order to determine the probability that a particle will pass the m^2 cut. Such a probability can then be used as a multiplicative weight factor characterizing the event.

The first choice would mean rejecting a larger fraction of the lower-momentum tracks, that actually have a better measured TOF. As will become clear in the discussion presented in chapter 5, the second option fits with the rest of the Monte Carlo calculations scheme rather well, therefore, we chose it as the way to take the momentum dependence of the m^2 cut into account (see chapter 5).

4.5 The Effect of the Event Centrality on C(q_{inv})

4.5.1 Event Multiplicity and Centrality

As already mentioned in chapter 1, the impact parameter of a collision between two nuclei can be expected to have a direct effect on the reaction volume. We used our correlation measurements, which are sensitive to the particle source size, to determine experimentally if the source size depends on the initial reaction volume, by studying two proton correlations in different centrality regimes.

For the purpose of this study we can use the Silicon Pad Detector to define centrality cuts (effectively grouping the data according to different impact parameter bins) and see if the observed shape of the correlation function shows any dependence on such cuts. This is possible because the number of produced sec-

[20]as discussed in chapter 2, in this study we compare the data and the theoretical correlation function by applying all relevant corrections in the Monte Carlo

ondaries depends on the geometry of the collision (see chapter 1; a discussion of experimental data on $dN_{ch}/d\eta$ can be found in [3]), therefore, the grouping of events can be based on the charged particle multiplicity [21].

4.5.2 The Silicon Detector Data

The Silicon Detector information is processed in a way similar to to other data components, but the results are stored in separate histograms that are used later for the event centrality estimate (see chapter 5). A typical calibrated ADC spectrum obtained from an individual pad of the Silicon Detector (S+Pb data) is shown in Fig. 4.29, on two different scales: the upper plot shows the pedestal and ionization peaks. The lower plot actually reveals a problem in this measurement: the long tail that is clearly seen in this plot is due to pile-up events – in a separate study, it was established that this tail is strongly dependent on the intensity of the beam and the rate of interactions, whereas the position and relative amplitude of the peaks are stable and do not show any noticeable rate dependence[22]. In such pile-up events, the time elapsed between adjacent events was not sufficient for the pad to recover, leading to signals with large amplitude, not correlated with the actual ionization signal. We will return to the pile-up problem shortly.

[21] the detector was used for measuring charged particle multiplicities with 2π acceptance in ϕ and pseudorapidity range $1.5 < \eta < 3.3$

[22] it is worth mentioning that this pile-up is specific to the Silicon Detector and did not affect other spectrometer subsystems

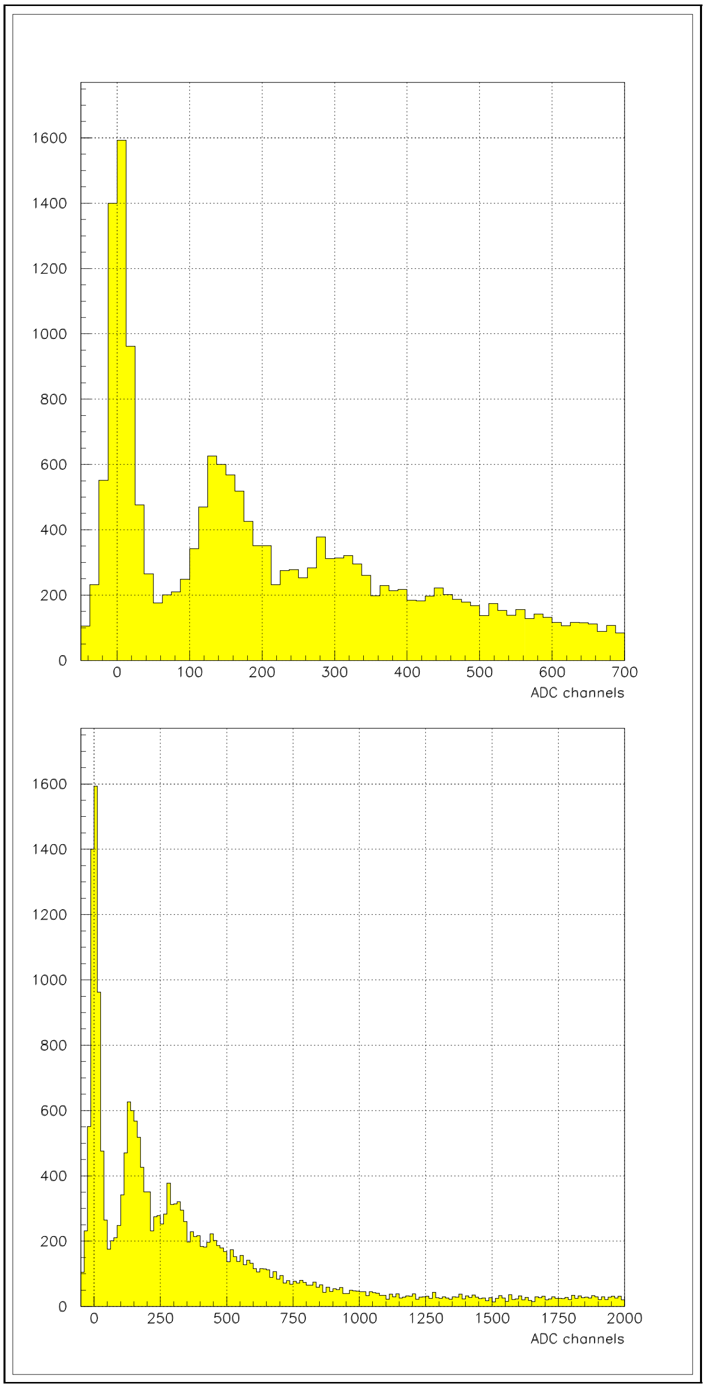

Figure 4.29: Typical calibrated ADC spectrum of signals from an individual pad of the Silicon Detector (S+Pb data), shown on two different scales: the upper plot shows details of the pedestal and ionization peaks; the tail due to the pile-up events is clearly seen in the lower plot

The ADC Signal Spectra

In Fig. 4.29, the pedestal peak (around zero) corresponds to an "empty" pad (no particles); peaks corresponding to a single, double, etc ionizing particles are visible and separated from the pedestal peak. This information can actually be used for the multiplicity measurement in a number of ways:

1. we can calculate the so-called *ADC sum*, i.e. the sum of signals from all pads, that is correlated with the charged particle multiplicity in the fiducial volume of the detector

2. it is possible to perform a fit of the ADC signal distributions, for each pad, with a sum of curves (e.g. modified Landau distributions) corresponding to zero, one, two etc particles; based on the fit results and the pad signal amplitude (in ADC counts) in a particular event, we can then estimate the effective multiplicity in the pad, for each event, and calculate the total charged particle multiplicity for the whole detector

3. we can discriminate signals with amplitude below a certain threshold and count the number of pads with signals in excess of the pedestal (i.e. pads that "fired"); such pads have *one or more particle tracks passing through them*

Application of methods (1) and (2) is difficult because they rely on precision of the dE/dx signal measurement and thus are rather sensitive to the electronics noise and pile-up effects in the detector (discussed above). As can be seen in Fig. 4.29, the ionization peaks are somewhat diffuse[23].

As will be discussed in chapter 5, the basic approach chosen to estimate the event centrality in the present study is to match the results of a complete `GEANT` simulation of the Silicon Detector (with the `RQMD` event generator as input) and the experimental data. From this point of view, method (3) seems particularly attractive as it is based on a rather clean-cut definition of a hit pad and does not concern itself with either precise measurement of the dE/dx signal or separation of dE/dx peaks corresponding to multiple particles. We chose method (3) for our event centrality study. Its implications and potential difficulties are discussed later in this section.

Inspection of the individual pad dE/dx spectra like one shown in Fig. 4.29 leads to the conclusion that signals with amplitude below 800–1000 ADC channels are, by large, not affected by the pile-up in a drastic way[24], whereas signals above that value are mostly due to pile-up effects. This creates a possibility to correct the problem in the following way: when counting the pads that "fired", we ignore those with large amplitude and keep track of their number as well[25]. It may then be treated as "variable inefficiency", meaning that the number of active pads in the detector is varying from event to event and the thus measured

[23]in chapter 5 we will consider "ideal" dE/dx spectra in the silicon pads, which are much sharper

[24]one indication of that is the fact that the spectra, in this limited range, can be fitted pretty well with a sum of modified Landau distributions

[25]the number of pads affected depends on the data-taking conditions such as mean occupancy per pad, beam intensity etc., and was of the order 10 for p+Pb and 30 for S+Pb running

silicon detector multiplicity is then corrected, on event-by-event basis, by the corresponding inefficiency factor defined by the number of pads that were ignored ("dynamical correction").

The distribution of thus obtained silicon detector multiplicity is shown in Figs. 4.30 and 4.31 for S+Pb and p+Pb data, respectively. The obviously dif-

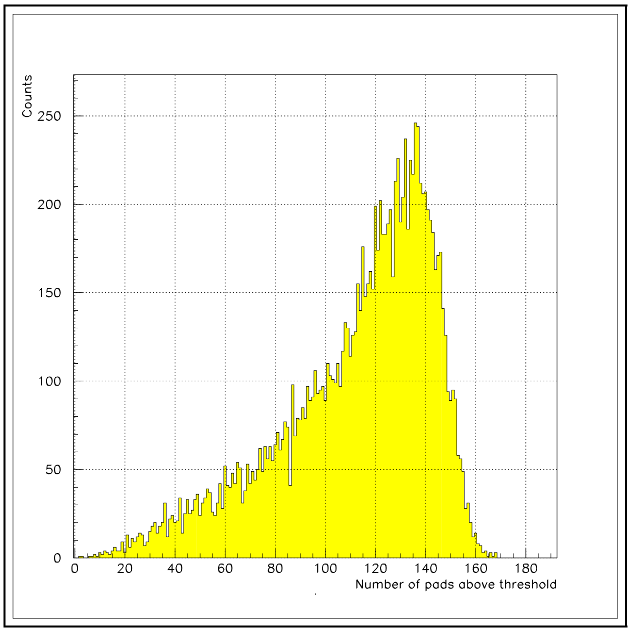

Figure 4.30: Distribution of the number of hit pads in the Silicon Detector (S+Pb data)

ferent shape of these distributions is the result of the difference between the two projectile+target systems and different trigger conditions (trigger bias), as discussed in 3.4.1. These distributions are a starting point in the study undertaken to determine the respective centralities of these data samples (see chapter 5). The pile-up effects and the "dynamical correction" could be a source of systematic

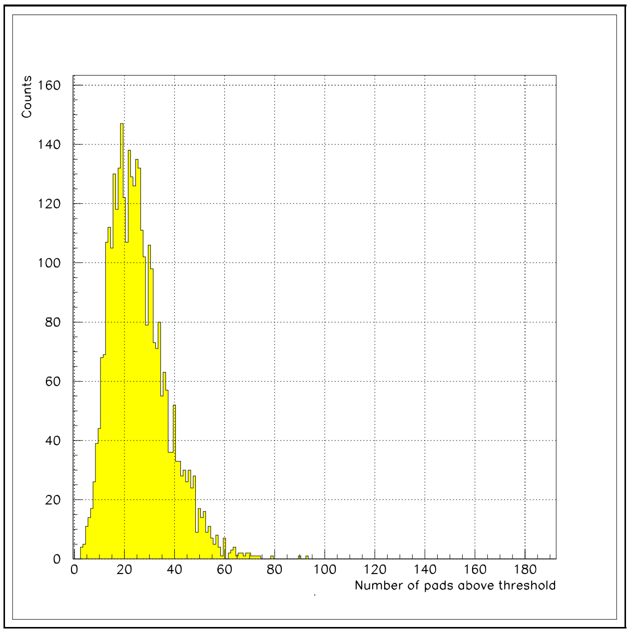

Figure 4.31: Distribution of the number of hit pads in the Silicon Detector (p+Pb data)

error in this study and will be discussed separately in section 5.6.3.

Comments on the Method

As can be seen in Fig. 4.30, the S+Pb data is characterized by a relatively large pad occupancy: in about half of events, more than 50% of all pads in the detector actually "fired", i.e. had *one or more particle tracks* passing through them. Based on this, it may seem that the method we chose to treat the silicon detector data, i.e. count the number of pads that fired, was not very accurate since it is hard to differentiate the events with large multiplicities[26] that may effectively "saturate"

[26]if we assume that the number of hits in a given pad obeys the Poisson statistics with mean value μ, the probability for the pad to fire will be $P(N_{hit} > 0; \mu) = 1 - P(N_{hit} = 0; \mu) = 1 - e^{-\mu}$

the detector. However, as is also obvious from Fig. 4.30, the distribution has a rather long tail extending in the low multiplicity region, signaling significant fraction of peripheral events. In chapter 5 we will demonstrate that the correlation function's sensitivity to the event impact parameter is much greater for the peripheral events and that there are certain physical constraints on the centrality distribution that allow a robust centrality estimate.

4.5.3 The Dependence of the Correlation Function on the Event Centrality

For the purpose of this study, we treat the data in the following way: both S+Pb and p+Pb data samples are subdivided into subsets depending on the event multiplicity, as defined in the previous section. From the S+Pb sample we select 1/3 "most central" and 1/3 "most peripheral" events, based on the distribution presented in Fig. 4.30 (this subdivision was chosen in an attempt to see the possible centrality effect more clearly). The p+Pb data was divided in two halves (due to significantly smaller available statistics) in a similar way. The data from the "most central" and "most peripheral" subsets are further passed through the usual analysis chain and used to construct respective correlation functions. The comparison of these correlation functions is shown in Figs. 4.32 (S+Pb) and 4.32 (p+Pb).

As can be seen, the "central" data points tend to be lower than "peripheral", corresponding to a flatter correlation peak; as discussed in chapter 2, this is an indication that the peripheral events have smaller source size, and conversely, central event are characterized by a larger source. We conclude that the data confirm that the source size depends on the reaction volume.

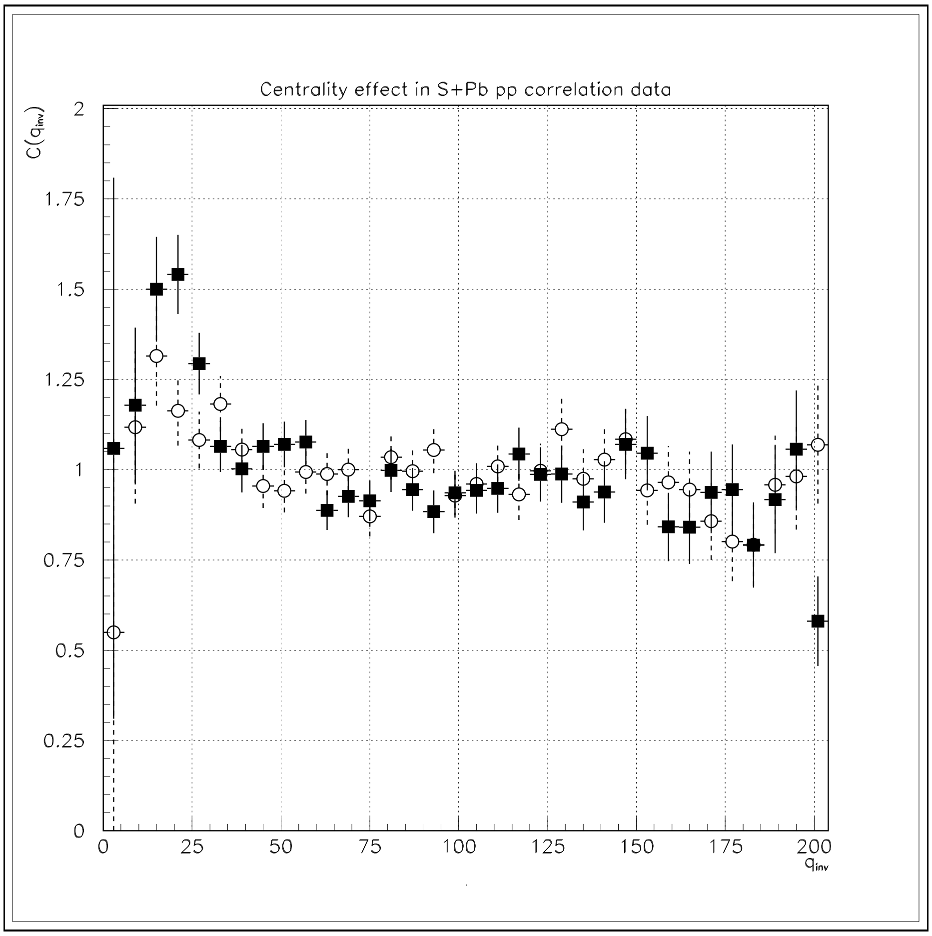

Figure 4.32: Centrality Effect in the Data: Proton Correlation Function (200 GeV/A S+Pb collisions) in two centrality bins. Open circles correspond to more central events, closed squares – to more peripheral events

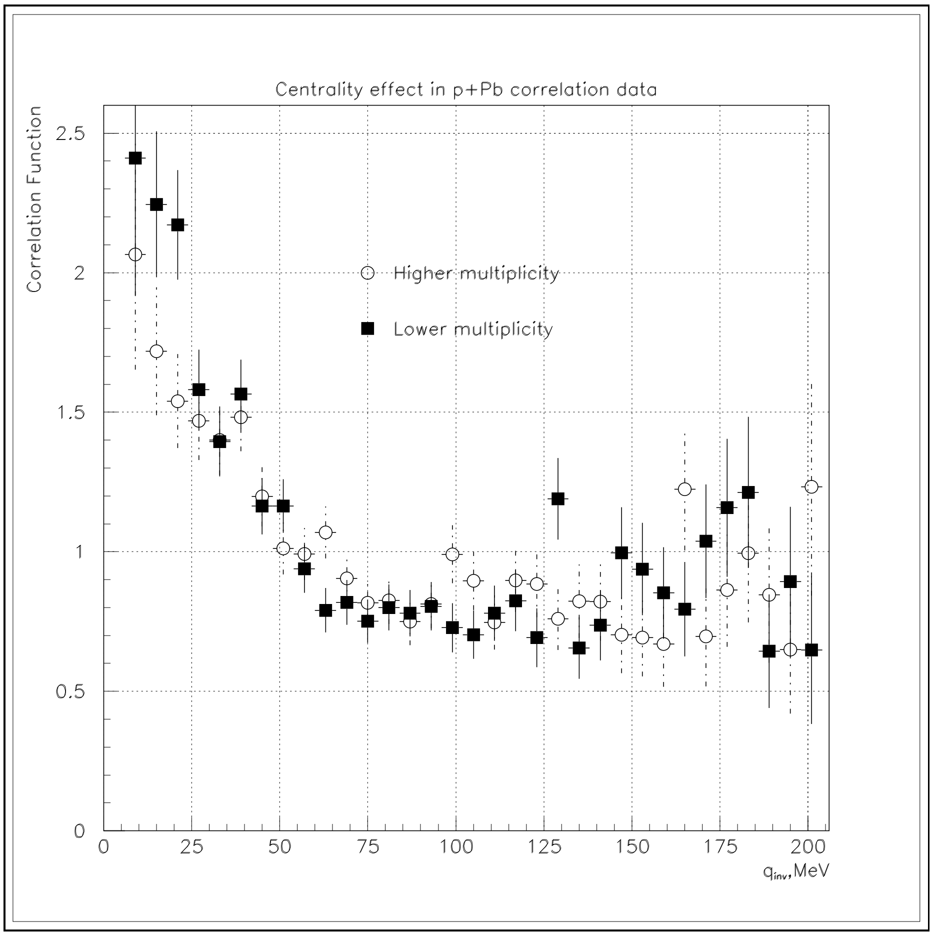

Figure 4.33: Centrality Effect in the Data: Proton Correlation Function (450 GeV/A p+Pb collisions) in two centrality bins

Chapter 5

Monte Carlo (MC)

5.1 Introduction

As discussed in the Introduction (chapter 1), one of the goals of this thesis is to provide a comparison of the analyzed data with a model of heavy-ion collisions. At present, models of *RHIC* that have an adequate predictive power exist primarily in the form of the so-called “event generators”. Typically, such an event generator is a particle-transport computer code that is based, to some degree, on the phenomenological approach. More specifically, this means that concepts of field theory are combined with the quark-parton model of the nucleon, on the one hand, and with characteristics of hadronic interactions that are either known or inferred from experiment, on the other. The latter is important, since it allows to take into account “soft” processes, such as rescattering of hadrons and resonances, that are an important component of the heavy-ion collision.

The existing event generators differ, to one degree or another, in the ways they handle both interaction of partons and rescattering of hadrons. Some of the most widely used models in the field of heavy-ion physics are `ARC`, `FRITIOF`, `RQMD` and `VENUS`, each claiming varying degrees of success explaining different aspects of the available experimental data. In the present study we chose the `RQMD` event generator (version 1.08) as basis for comparison with the measured pp correlations. The model is briefly discussed in 5.2.2.

As discussed in chapter 2, there are several important factors that have to be taken into account when comparing the experimentally measured correlation function to theory. In this thesis, we use the method of Monte Carlo (MC) for the following major purposes

- Simulation of the particle source, using the `RQMD` model (section 5.2.2)
- Simulation of the NA44 detector for the purpose of studying and taking into account factors essential for the study of low relative momentum proton pairs, such as
    1. the single particle acceptance of the apparatus, to determine the phase-space coverage
    2. the two-particle acceptance of the apparatus
    3. momentum resolution of the apparatus (largely defined by multiple scattering)
    4. effects related to the track reconstruction
- Estimation of the trigger bias (event centrality)

- Estimation of the contribution of strange baryon decays to the total proton population

As will be explained in the next section, we are using a relatively sophisticated Monte Carlo scheme, where effects related to the acceptance and resolution of the detector were simulated using a program based on the `TURTLE` software (see 4.4.1, [42]); the charged particle multiplicity in the Silicon Pad Detector (sections 3.3.2 and 4.5.2) was studied using the `GEANT` package. This division of tasks is necessary for several reasons: for example, using the `TURTLE` software makes it a lot easier to implement an interface to the NA44 tracking software, which itself is based on `TURTLE` (section 4.4.1) and speeds up the calculation; only a few (in our case, two) particles are propagated through the detector in each Monte Carlo event, and the physics being simulated is largely confined to the motion of a charged particle in the magnetic field and multiple scattering. On the other hand, `GEANT` provides the tools necessary to process events with $\propto 10^3$ particles in the final state[1], taking into account all aspects of their interaction with various detector parts; a good example is conversion of photons into e^+e^- pairs in the target and subsequent development of electromagnetic showers in the target and other adjacent detector elements[2]. Clearly, such effects are crucial for correct simulation of the detected multiplicity distributions and in this respect `GEANT` was indispensable.

In the following, we will discuss how the "theoretical" Correlation Function is

[1] typical of a central S+Pb event, counting γ conversions in the target

[2] the thickness of the target was quite significant in both S+Pb and p+Pb measurements, 5 and 10 mm of lead, respectively

calculated. We will explain how this calculation is structured as a set of separate tasks and how these are related to each other.

The chapter will conclude with the analysis of systematic uncertainty of the final Monte Carlo result, crucial for meaningful comparison with experimental data.

5.2 The MC Proton Correlation Function

5.2.1 Construction of the MC pairs sample

As mentioned in chapter 2, the basic approach chosen for comparison of the data with model predictions was not to correct the data, but instead try to faithfully reproduce various effects of the actual measurement by simulating the apparatus in software. In fact, what happens in calculation closely resembles what happens in the actual experiment; this correspondence is illustrated in table 5.1.

A complete diagram of all parts of the Monte Carlo simulation chain is presented in Fig. 5.1. In the following discussion, we will assume that we work with S+Pb system (proton-lead collisions were treated in a very similar manner). We will now discuss some of these steps in more detail.

5.2.2 The `RQMD` event generator

The `RQMD` event generator was the starting point (see [27, 28, 29, 44] and references therein). It owes its name to the *Relativistic Quantum Molecular Dynamics* approach [27], which is based on string excitation and fragmentation with subsequent

Table 5.1: Correspondence between the actual correlation measurement and the Monte Carlo chain

Experiment	Monte Carlo
Particles (protons) are produced in an A+A or p+A collision and populate a certain volume in the momentum space and in space-time	`RQMD` generates coordinates and momenta of particles at their emission point (section 5.2.2)
Due to statistical properties and Final State Interactions, correlations between the particles' momenta arise (chapter 2)	Based on the known interaction between the particles and their statistics, *the statistical weight of each pair* is calculated (see section 5.2.3)
Proton pairs propagate through the detector, leaving dE/dx signals in the hodoscopes	Propagation of proton pairs through the detector is simulated using the `TURTLE` package
Momentum reconstruction is performed using the standard NA44 software	Momentum reconstruction is performed using the standard NA44 software
Successfully reconstructed pairs are recorded in a file	Successfully reconstructed pairs are recorded in a file, with the previously calculated weight
The Correlation Function is calculated	The Correlation Function is calculated

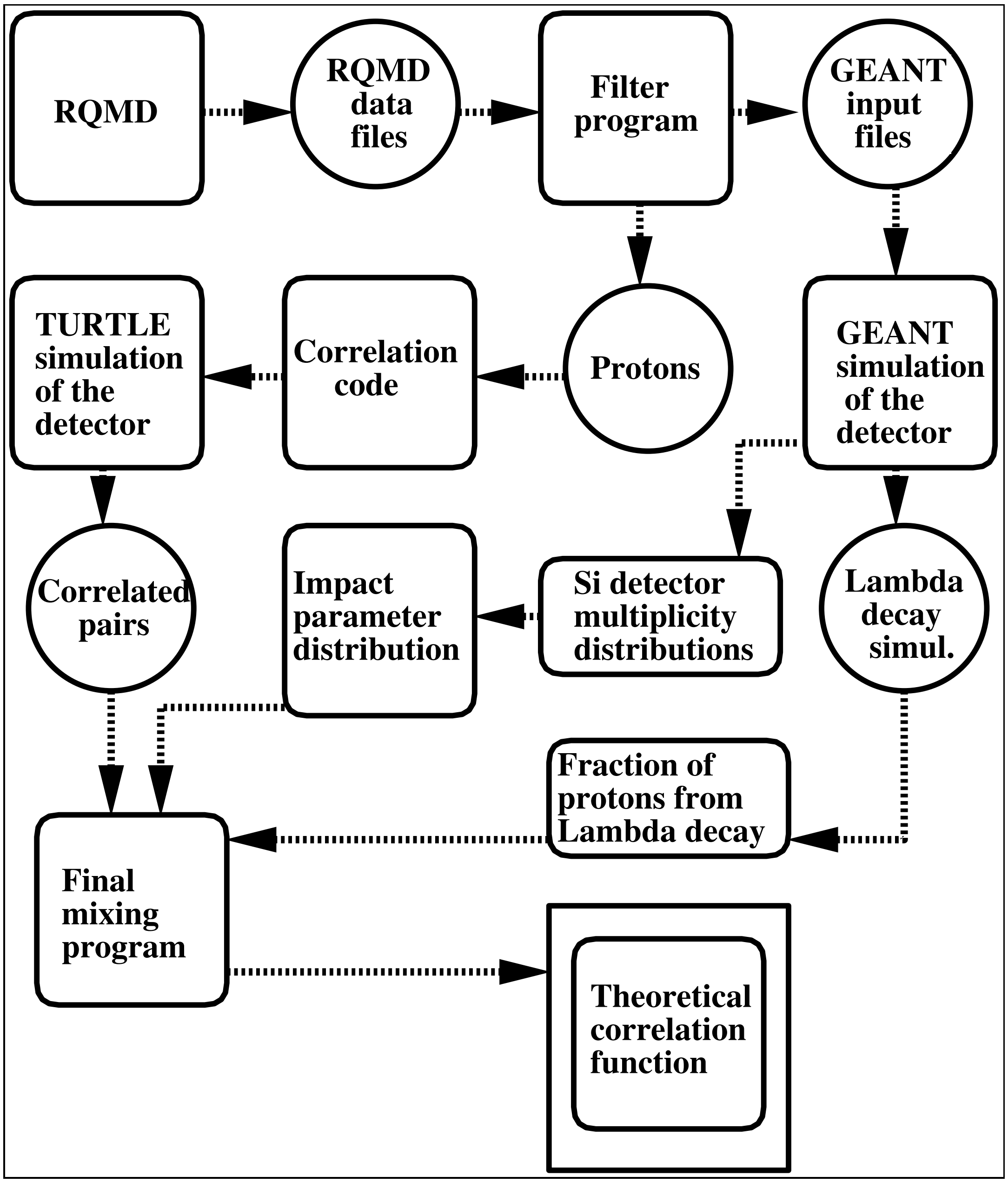

Figure 5.1: The Diagram of the Monte Carlo simulation chain

hadronic collisions.

As described in [44], hadrons and their constituents are propagated in classical phase space, with stochastic interactions, e.g. collisions and decays. In the process of the collision, depending on whether nucleons are within the range defined by the nucleon-nucleon cross section, longitudinal momentum is exchanged, resulting in excitation of the nucleon into a resonance or into a string. In the latter case, the momentum transferred to one of the quarks can further polarize a sea quark pair, and such process may be repeated, employing the same principle. These strings then evolve in space-time and eventually break, producing secondary hadrons. After a certain time, the probability of rescattering of the secondary particle becomes negligible, and strong interactions effectively cease ("freezout"). Space-time coordinates of the last rescattering, which can also be called emission point, and the final values of the particle's momentum, constitute the output of the model[3].

Starting with version 1.08, the `RQMD` event generator had an important new feature – the so-called "color ropes", that are created from overlapping color strings. Their discussion is beyond the scope of this presentation. We note, however, that this component of the model is crucial in the analysis of production of strange baryons and antibaryons (see, for example, [29]). As was verified in a separate `RQMD` calculation, the influence of the color ropes on the "direct" proton

[3]for one event

production[4] is very small and can be neglected for the purposes of this study, however, as we will see later in this chapter, it is important in the analysis of the contribution of the strange baryon decays to the total number of detected protons.

The `RQMD` Proton Source

Since the `RQMD` model serves as a basis for comparison in this study, it is instructive to look at the generated `RQMD` events from the point of view of the configuration[5] of the source. We will first present the configuration of the `RQMD` source without taking into account effects of the restricted acceptance of the apparatus, and then show that the acceptance defines what part of the source we actually see.

Let's first examine the rapidity distributions (dN/dy) of the emitted protons. In Fig. 5.2 we show dN/dy distributions of `RQMD` protons obtained at different values of the impact parameter, in the lab reference frame.

As we go from very peripheral (b=8fm) to central (b=2fm) collisions, the proton yield at mid-rapidity steadily increases, in compliance with the geometrical picture of a heavy-ion collision presented in section 1.2. It can also be seen from this figure that, according to `RQMD`, there are virtually no projectile nucleons that can penetrate the target without losing most of their momentum, i.e. there is a fair amount of stopping.

The spatial distribution of the proton emission points (i.e. points of last re-

[4] meaning protons that are not decay products of strange baryons

[5] i.e. characteristics of the space-time and momenta distributions of the particles emitted

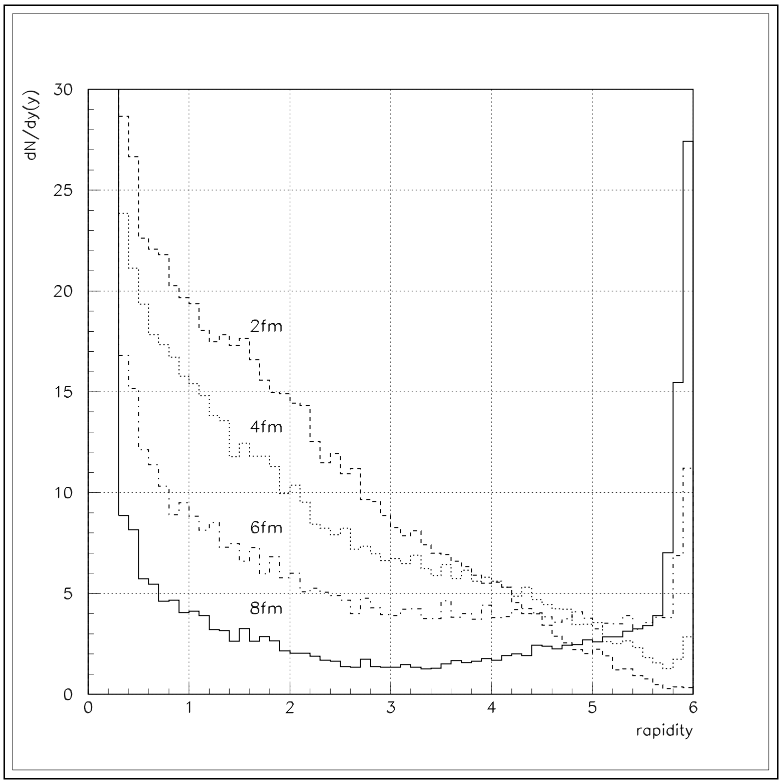

Figure 5.2: dN/dy distributions of the `RQMD` protons for different "b" values (S+Pb collisions at 200 GeV/A). Zero on the horizontal scale corresponds the target rapidity, y=6 corresponds to the projectile nucleons.

scattering) is shown in Fig. 5.3, and the momenta of emitted protons are presented in Fig. 5.4; these data were generated for S+Pb collisions at 200 GeV/A, with impact parameter b=4fm. It is obvious from the rapidity distribution in Fig.5.4 (c.m.s. reference frame) that at this impact parameter the sulphur nucleus is virtually destroyed (obviously, there are very few particles at the projectile rapidity).

One important feature of the model is the presence of correlation between the momenta of emitted particle and the coordinates of the point of their emission; if we look at the such source from a fixed point in space, the particles that we observe would seem to be moving in the direction of the observer, whereas the particles emanating from the "dark side" of the source would be moving away from us and not accessible for observation[6]. Similarly, there's also a strong correlation between the xyz coordinates and the emission time t. These correlations are presented in Fig. 5.5.

Another interesting distribution is shown in Fig. 5.6, which is the scatterplot of a proton's transverse momentum vs rapidity. Apparently, the central rapidity region of the source produces protons with higher p_T. We will now look at what effect the limited acceptance [7] (whose shape in $p_T - y$ is presented in Fig. 3.4) has on these distributions; x, y and y vs x are presented in Fig. 5.7. Apparent bias in the x coordinate distribution is due to the very asymmetric acceptance of the

[6] this can be explained in several different ways, for example, as a consequence of the source expansion or "shadowing"

[7] Here we are using an approximation of the actual acceptance

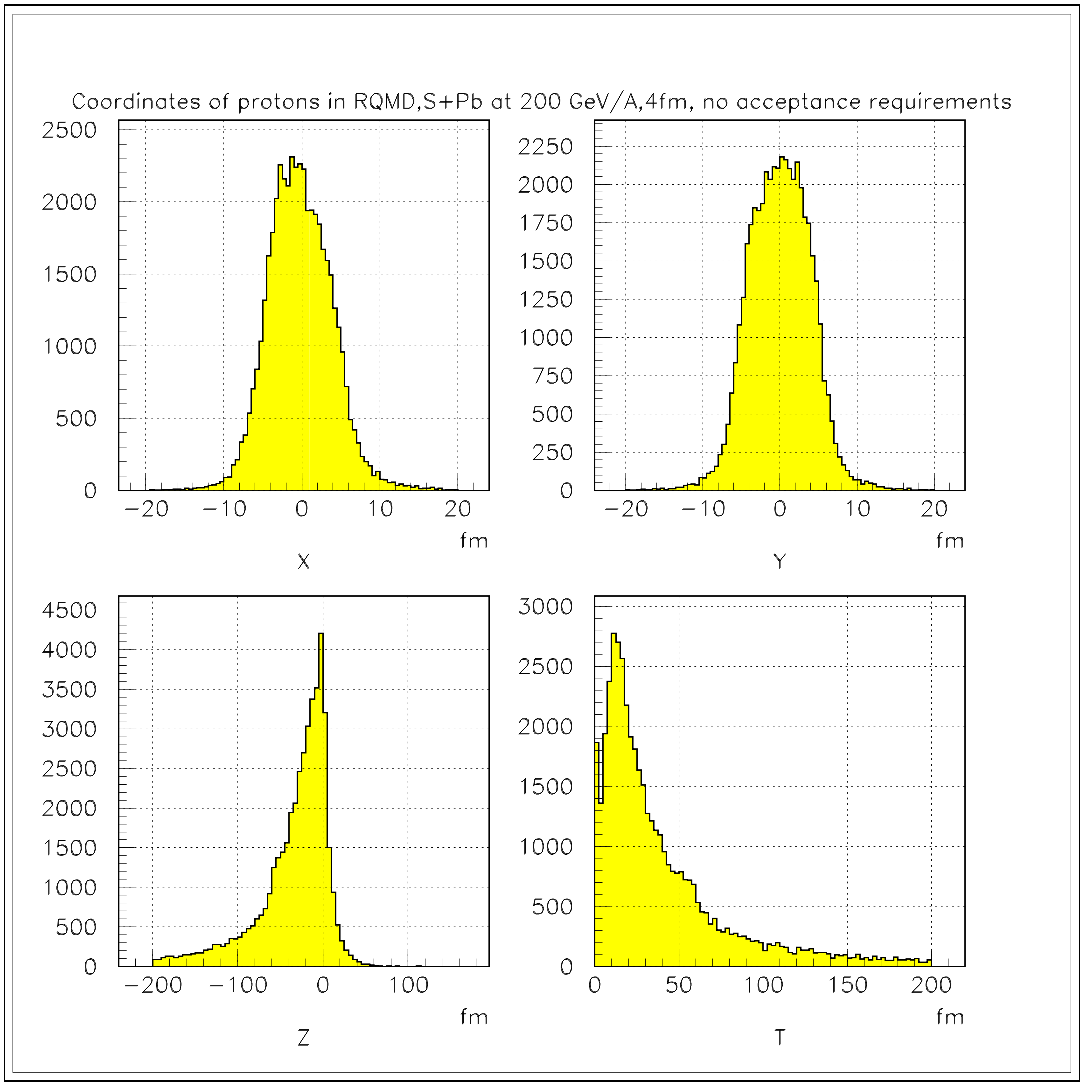

Figure 5.3: The RQMD emission points, S+Pb collisions at 200 GeV/A, b=4fm. Coordinates are in fm. The positive z direction corresponds to the line of motion of the projectile nucleus.

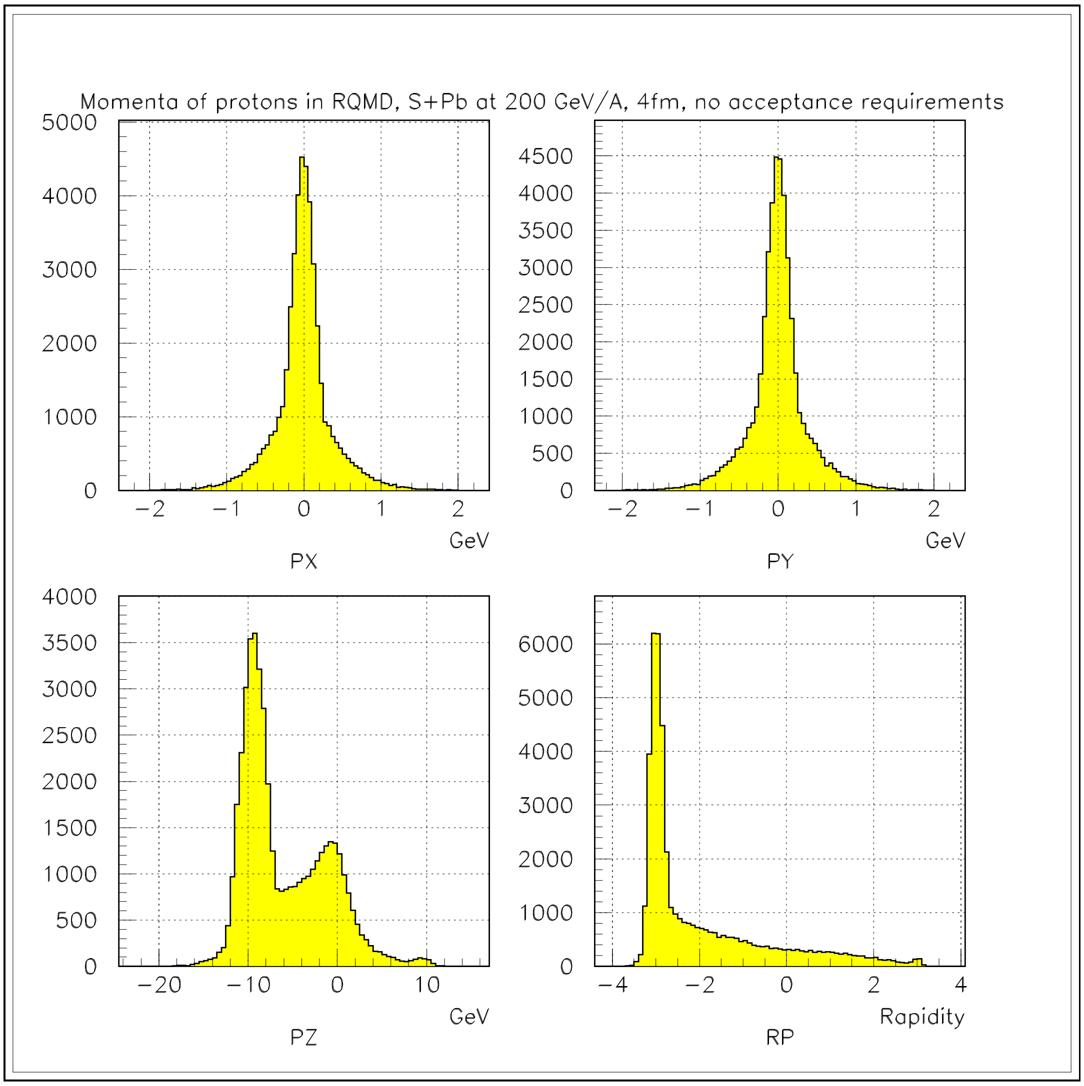

Figure 5.4: The `RQMD` momenta of protons, S+Pb collisions at 200 GeV/A, b=4fm. Momenta are in GeV. The positive z direction corresponds to the line of motion of the projectile nucleus.

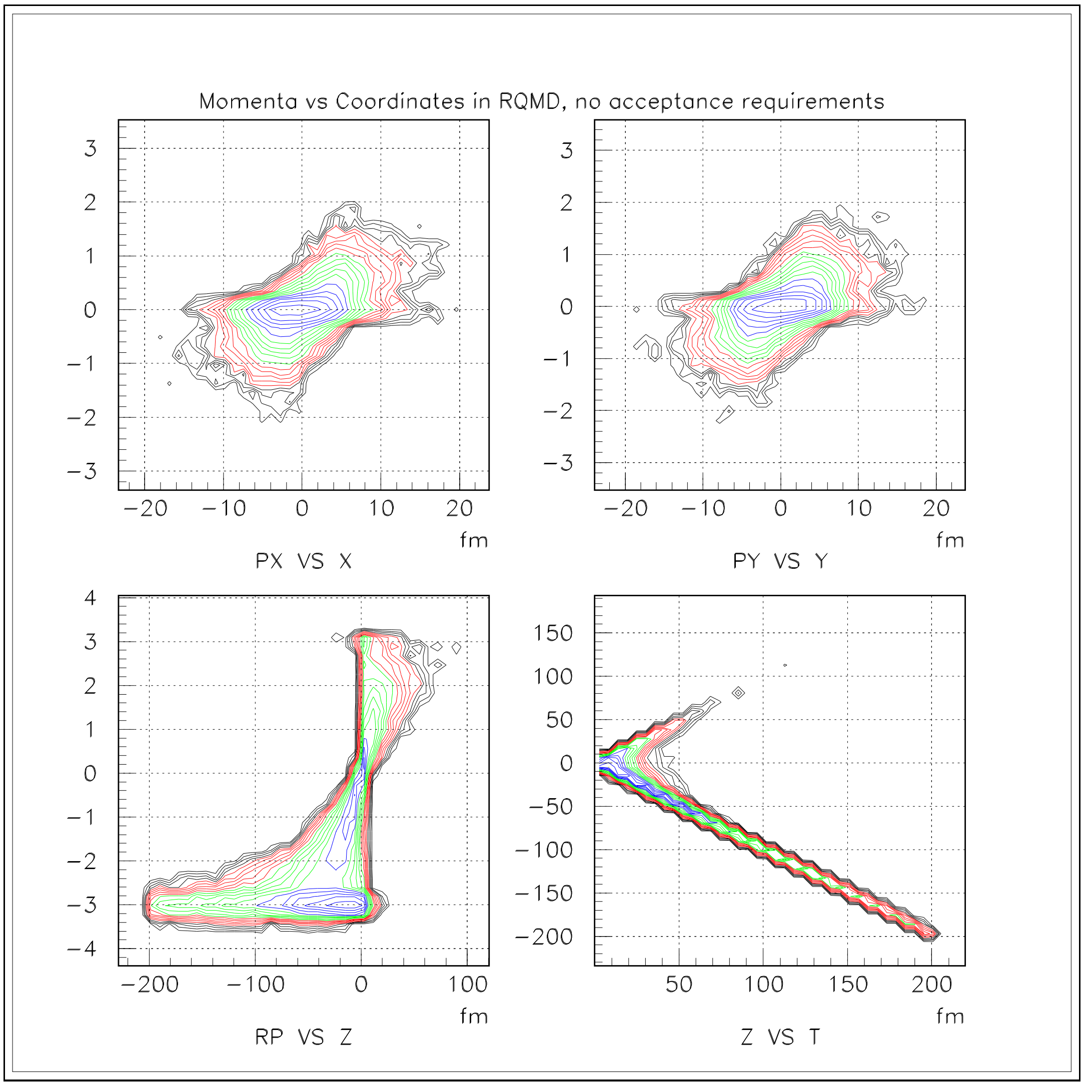

Figure 5.5: Correlation between the momenta and coordinates of protons in `RQMD`, S+Pb collisions at 200 GeV/A, b=4fm. Coordinates and time are in fm, momenta in GeV

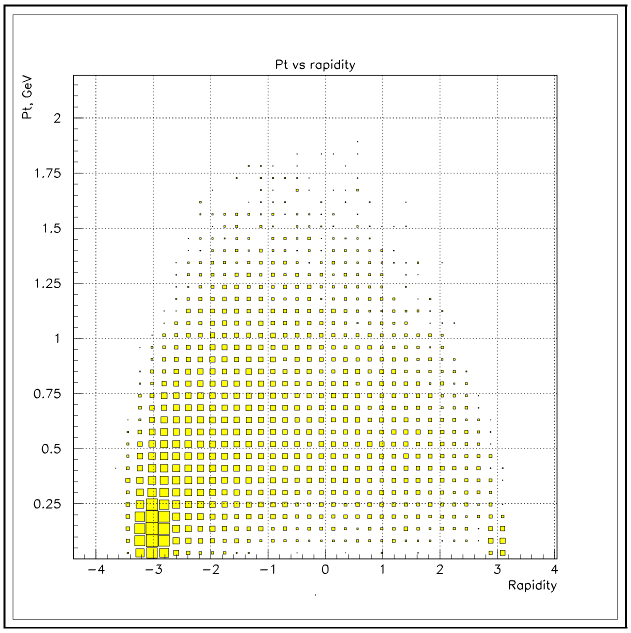

Figure 5.6: Pt vs Rapidity of RQMD protons, S+Pb collisions at 200 GeV/A, b=4fm

NA44 detector in p_x (see chapter 3)[8].

Using the RQMD Data for the Proton Correlation Study

RQMD produces a file, in ASCII format, with information on the type, coordinates and momenta of particles at the time of their last scattering, that effectively constitutes emission. There is a choice of options that a user can specify for a simulation run, such as forcible decay of resonances, reference frame of the produced particles, etc.

Resulting event files were then processed using a program written in C that

[8] note that even before we applied the acceptance requirements, the x distribution was slightly shifted due to the way the RQMD events were generated (before the collision, the lines of motion of the target and projectile nuclei are separated by distance b along the x axis), see Fig. 5.3

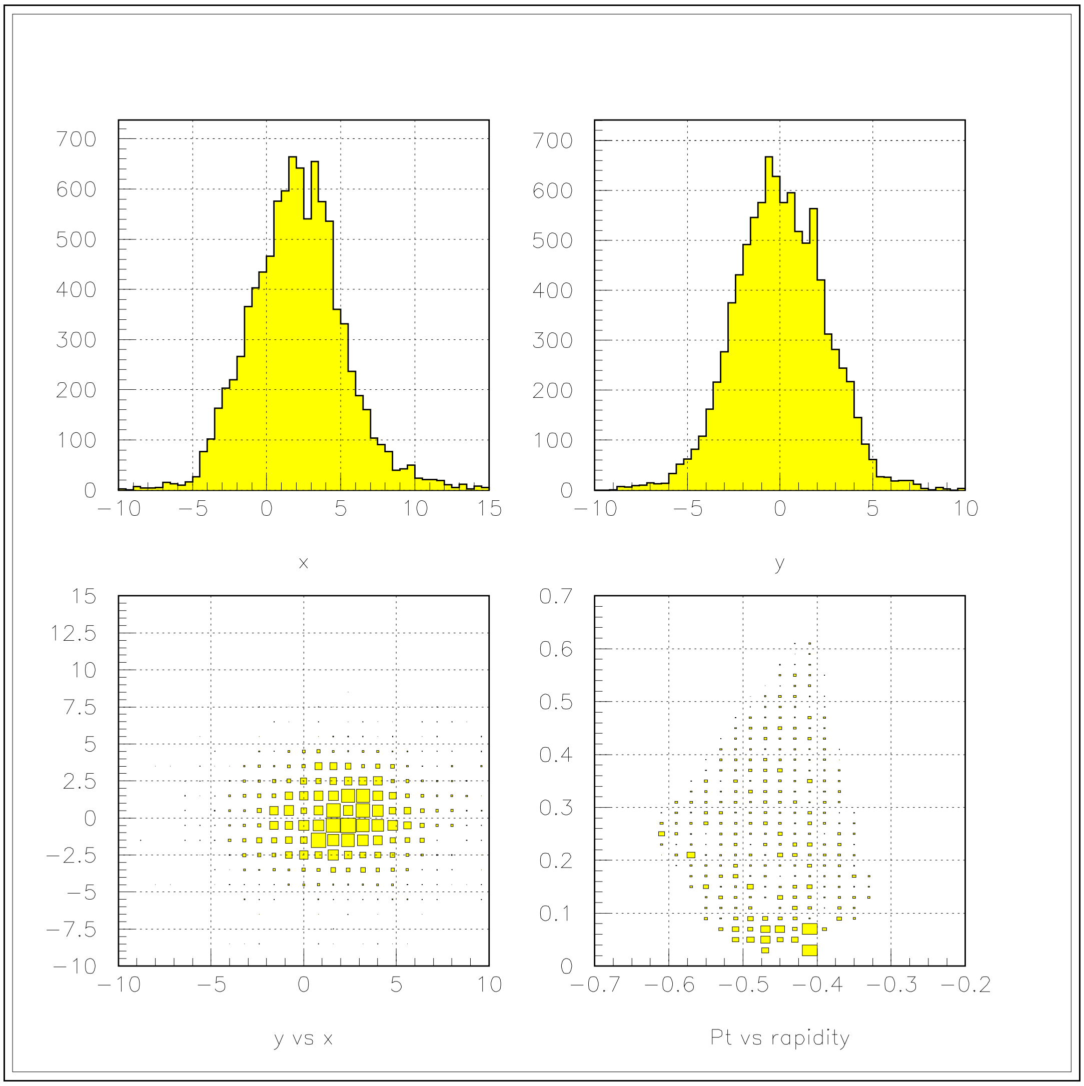

Figure 5.7: Characteristics of the RQMD protons (x and y, and transverse momentum vs rapidity), S+Pb collisions at 200 GeV/A, b=4fm (with limited acceptance); x and y coordinates are in fm, P_t in GeV

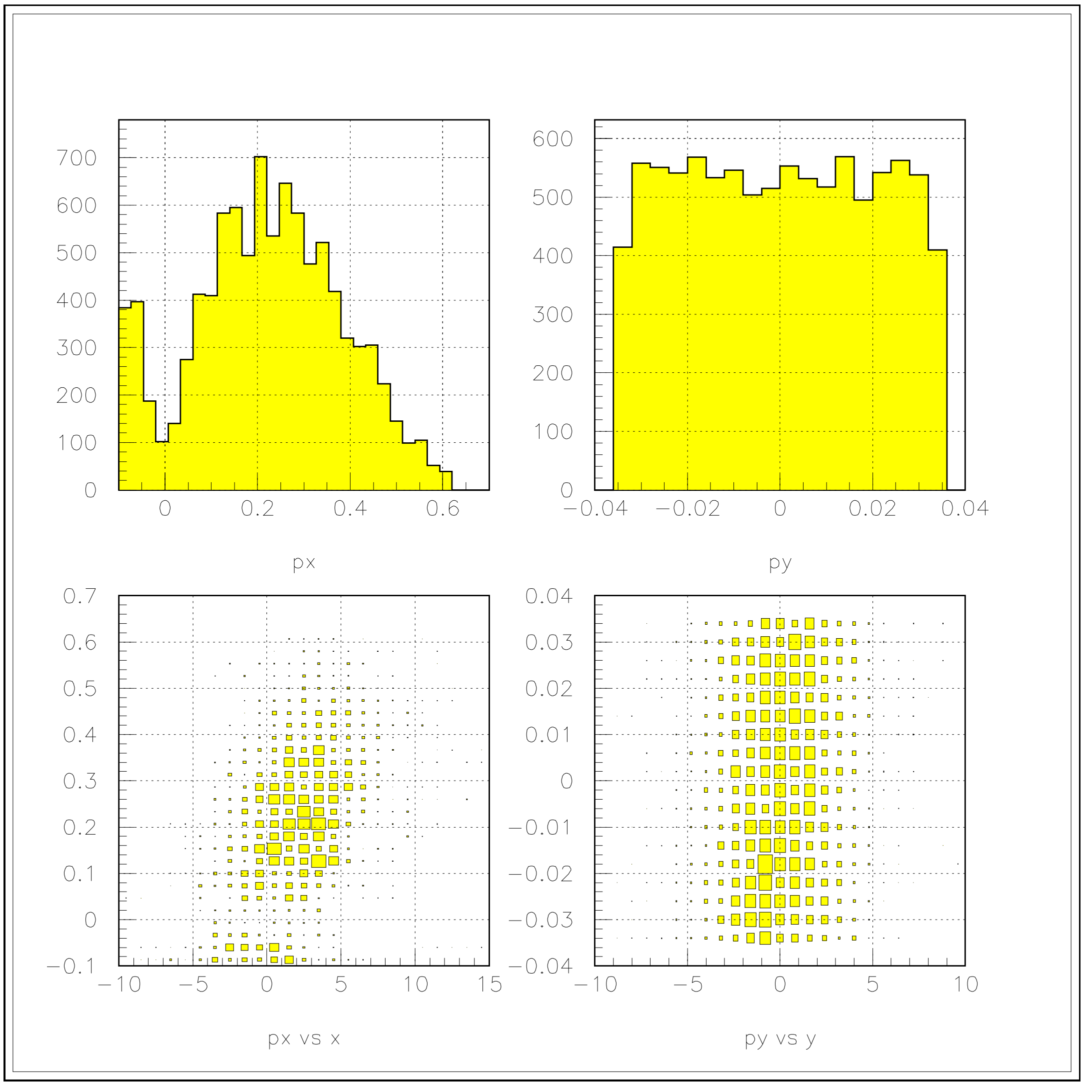

Figure 5.8: Characteristics of the `RQMD` protons (p_x, p_y), S+Pb collisions at 200 GeV/A, b=4fm (with limited acceptance). Coordinates are in fm, momenta in GeV.

was capable of producing output in three different formats, depending on the command line options:

1. Data stream suitable for input to a `GEANT` simulation program, where the particle codes were converted from the internal `RQMD` representation to `GEANT` standard – for the purposes of the event centrality study (see section 5.3)

2. A list of spatial and momentum information about proton emission points, suitable for input to the "correlator" code that we will discuss in section 5.2.3

3. Diagnostic messages helping to debug the `RQMD` data in case it was corrupted (see appendix D)

When constructing the MC pair sample, we choose option 2 from the above list and obtain a list of phase space points (i.e. a list of space-time coordinates of the emission points and 4-momenta of the particles). For the sake of brevity, in the following discussion we will sometimes also use the word "tracks".

Ideally, we would like to consider proton pairs produced in the same Monte Carlo events, meaning that if we have a MC event number N, we consider protons p_{1N} and p_{2N} and observe (calculate) the correlations between the two. However, despite the large total number of protons participating in the collision, the $\frac{dN}{dy}$ in the central rapidity region is relatively small (most of the "available" protons are actually spectators), the cross section of the process that leads to formation of a proton pair with $\sim$ 10 MeV relative momentum is tiny. The situation is aggravated by the shape of the NA44 acceptance, that is roughly $\pm$ 35 MeV in P_y, meaning that ϕ-acceptance is severely limited and whatever close pairs we have are just likely to be lost – this is illustrated in table 5.3. As a result, the very low overall "efficiency" of the chain

$$\texttt{RQMD} \Rightarrow \text{MC model of the Detector} \Rightarrow \text{Reconstructed Pair Sample}$$

makes it impossible to accumulate sufficient statistics in any reasonable time. To solve this problem, we make the following two assumptions :

1. There is an azimuthal degeneracy, i.e. the events can be randomly rotated in ϕ in order to increase statistics – we can pick up pairs that we would have missed otherwise

2. We can combine tracks from different Monte Carlo events and treat them as if they were coming from the same event

While the first point is really trivial, the second deserves an explanation. In a S+Pb event where total multiplicity is $\sim 10^3$, the number of degrees of freedom is so big that one does not expect any dynamical correlations among the secondary particles related to the conservation of energy and momentum [9]. The rationale behind this is, therefore, in close relation to the argument in 2.2.1, where the

[9] we have to admit that the validity of this argument becomes less certain when considering the p+Pb system that typically has about 40 particles the final state, if the nuclear debris is discounted

background was constructed by the event-mixing technique. In effect, we treat each particle as a point in the "cloud" of points that represent the phase space populated by the reaction products (and that also is exactly the same as "the source", in the heavy–ion physics parlance). Hence, we assume an approach where we study characteristics of the source by sampling two points at a time and looking at whatever correlations might exist.

5.2.3 Calculating Correlations in the Two-Proton System

By the time this work started in 1992, there was a software tool to calculate correlations in the system of two particles, created by S.Pratt (and widely known as "Pratt's code"). The most essential part of this program, written in `FORTRAN`, is a subroutine that performs integration of the Coulomb wave function and takes into account the strong interaction component by introducing a corresponding phase shift, in the way similar to equation 2.15 (see chapter 2). The main module of the program was responsible for I/O, pair formation, histogramming, etc. It used both event rotation and mixing technique discussed above.

The way the code was written, there was no direct way to take the momentum resolution into account. The apparatus acceptance was implemented as a user-supplied function that returned a flag, specifying whether the particle, given its momentum, fit into the acceptance or not.

In the form this code existed, it was not suited for the purposes of the present study because

1. it did not allow for inclusion of the actual apparatus model

2. the way it was written, even with event rotation, the program would spend most of the time trying to pick up *two* tracks at a time that would make it through the detector, which, given the rather narrow acceptance of the NA44 apparatus, is extremely time consuming

3. the structure of the program was not well suited for modifications

The solution was to keep intact the part that calculates the statistical weights, i.e. is responsible for evaluating correlations, and re-design the general infrastructure. It turned out that the most advantageous design is to split the program in two, each part being small and manageable, and establish an interface with the detector simulation software (discussed in the following section), by means of `UNIX` pipes. This design provides for an extreme degree of modularity (the detector simulation program can be easily changed or bypassed without a single modification elsewhere, and the final mixing program can also be modified irrespective of anything else) and is illustrated in Fig. 5.9, which is basically a subset of the diagram presented in Fig. 5.1. In this diagram, the part labeled "Correlation Code" is responsible for

- opening the file containing the `RQMD` proton tracks
- forming proton pairs and calculating the corresponding statistical weight
- performing a crude check on whether the pair fits into the acceptance, saving

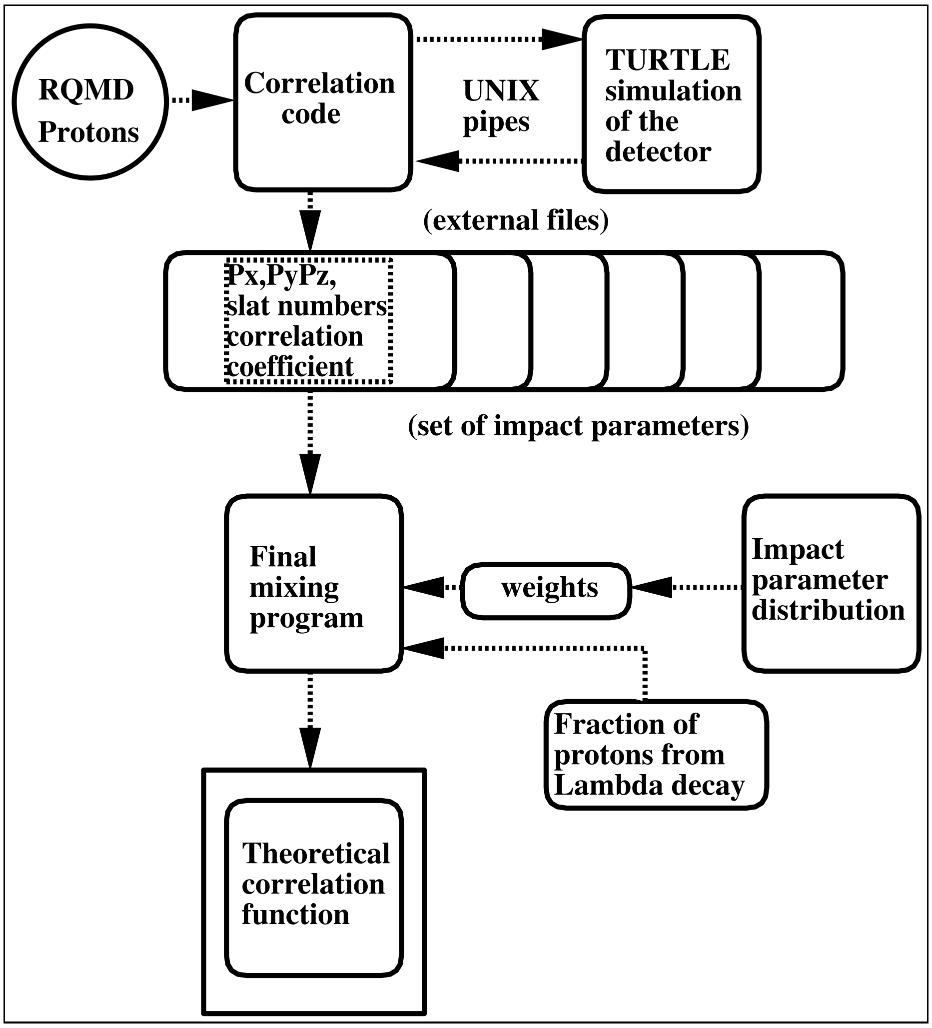

Figure 5.9: Implementation of the correlation program and the detector simulation interface

large amounts of the CPU time from being wasted on propagation of pairs that wouldn't reconstruct

- injecting pairs, via a `UNIX` pipe, into the program simulating the NA44 spectrometer and track reconstruction (see the following section)

- accepting the reconstructed pairs and storing them in a list (external file)

At this point, what we have is a list of *pairs*, or, rather, a set of such lists, for each impact parameter we are considering. The price we have to pay for the modularity is the necessity to store data sets in external files that are fairly big. On the other hand, we only have to run the lengthy `TURTLE` simulations once for each impact parameter and mix their results later (maybe including some types of background such as Λ decays), and that makes the system a lot easier to use. For example, if our centrality or background estimate changes, we just re-run the final mixing program once, in a matter of minutes.

5.2.4 The `TURTLE` Simulation of the Detector

The NA44 software features a certain degree of modularity, that allowed to build applications using "standard" infrastructure that included calibration and geometry databases, and a common track reconstruction system[10] that could be used for processing both real and Monte Carlo events. This is very important for the present study, since it helps to take the track reconstruction effects into account

[10] explained in section 4.4.1

in a consistent and credible manner. For this purpose, an application was built that included modules performing the following functions:

- initializing `UNIX` pipes for communication with the correlation program
- reading input tracks from a pipe (or waiting for such input)
- propagating particles through the detector [11], taking into account the actual detector acceptance and effects of multiple scattering in the target as well as other detector elements, and filling the `ZEBRA` banks necessary for subsequent track reconstruction
- momentum reconstruction using the same tracking algorithm and software modules as for the actual data
- generation of a flag signaling if the event was successfully reconstructed
- writing the reconstructed momenta and the reconstruction flag to a pipe, returning information to the correlation program

Essentially, this program was used as a "track reconstruction server", accessed asynchronously by the client program described in the previous section.

5.2.5 The Final Mixing of the MC Pair Samples

Based on the previously obtained list of correlated pairs, we further proceed to calculate the correlation function in a way very similar to that used with actual

[11] also based on the `TURTLE` software, see section 4.4.1

data:

1. a q_{inv} spectrum of "actual" is formed, with a possibility to include some physics background events, such as pairs where one proton came from a Λ decay (such pair is *not* correlated)

2. a q_{inv} spectrum of "background" is formed by event mixing technique

3. the ratio of the two spectra is found, with appropriate normalization — resulting in the Correlation Function

It is important that events of different impact parameter values be entered with appropriate weights, reflecting the centrality of the Monte Carlo sample, that in turn should be the same as that of the experimental data we are comparing with. Determination of these weights is the topic of the next section.

At this point, it is also necessary to take into account the momentum dependence of the m^2 cut efficiency (see section 4.4.6)[12]. In order to determine the efficiency factors, the distributions shown in Figs. 4.25 and 4.26 were parametrized and included in the final mixing program. Based on these data, in the process of the calculation each particle was assigned an additional (multiplicative) statistical weight corresponding to the m^2 cut efficiency that was defined by the particle's momentum.

[12]it is a natural place in the calculation since it is convenient to apply multiplicative factors to the weights of individual pairs that constitute the "actual" and "background" spectra

The magnitude of the effect associated with this momentum-dependent efficiency and its contribution to the systematic uncertainty will be discussed later in this chapter.

5.3 The Event Centrality Estimate

5.3.1 Dependence of the MC Correlation Function on the Event Centrality

To illustrate the importance of the centrality estimate, in Fig. 5.10 we present Correlation Functions generated for `RQMD` proton sources (S+Pb collisions at 200 GeV/A) at impact parameters $b = 1, 3, 5$ and 7 fm. In order to emphasize the dependence on b, we did not include in this calculation effects related to the momentum resolution and other factors, such as background protons from Λ decays, which will be discussed later in this chapter. As can be seen in Fig. 5.10, the dependence of the peak of the correlation function is quite significant; obviously, we have to make sure we understand the distribution of the impact parameter characterizing the data, i.e. match the centrality distribution of our Monte Carlo events with that of the data.

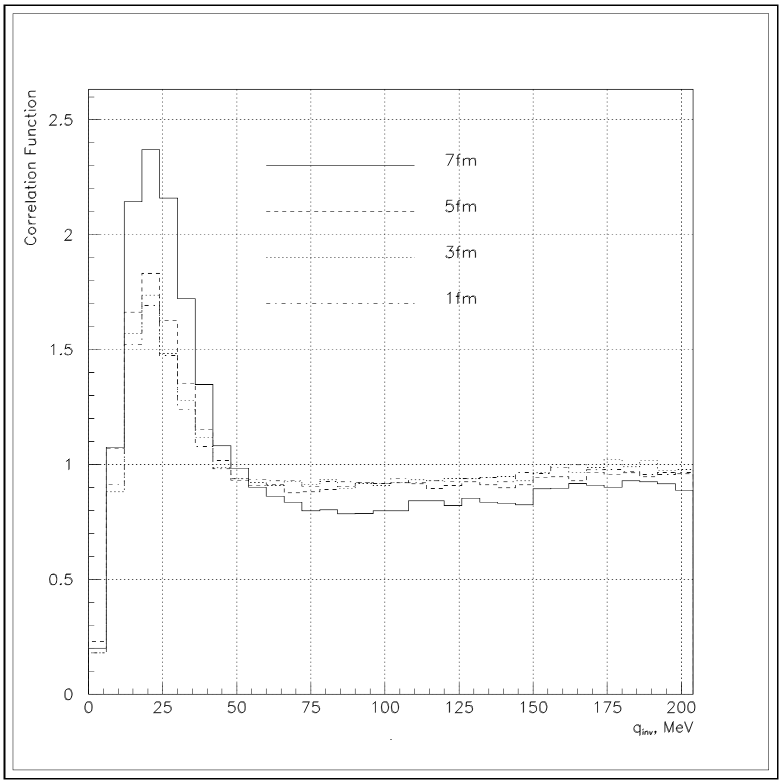

Figure 5.10: Correlation Functions generated for `RQMD` sources (S+PB collisions at 200 GeV/A) at impact parameters $b = 1, 3, 5$ and 7 fm; no momentum resolution or background effects taken into account

5.3.2 The Method

The Concept of the Method

To illustrate the method, let's consider first a naïve geometrical picture of a heavy-ion collision, where the two nuclei are represented by hard spheres. Similar to the argument presented in section 1.2, we can further consider two extreme cases, with the projectile nucleus either experiencing a head-on collision (impact parameter b equal to zero) or just grazing the target nucleus ($b = b_{max}$). The maximum value of the impact parameter of the collision in this hard sphere approximation is, obviously, just the sum of the radii of the participant nuclei, i.e. $b_{max} = R_{target} + R_{projectile}$. It is easy to see that, assuming random bombardment of the target nucleus, the density function of the impact parameter distribution (normalized to 1 event) will be

$$\frac{dN}{db} = \begin{cases} \frac{2}{b_{max}^2} b & \text{if } 0 < b < b_{max} \\ 0 & \text{otherwise} \end{cases}$$

i.e. it is linear with respect to b. This distribution only exists if there is no selectivity in terms of the event centrality (*"unbiased trigger"*). Since the trigger is often biased towards more "violent" collisions[13], as certainly was the case in NA44, the actual distribution of b tends to have a larger fraction of central and, correspondingly, lesser fraction of peripheral events. This is illustrated, in a very schematic way, in Fig. 5.11, where we sketch the differential cross-section $\frac{d\sigma}{db}$ as a function of b for both unbiased and central-biased trigger.

[13] as it should be if we are trying to observe phenomena taking place in a large nuclear volume

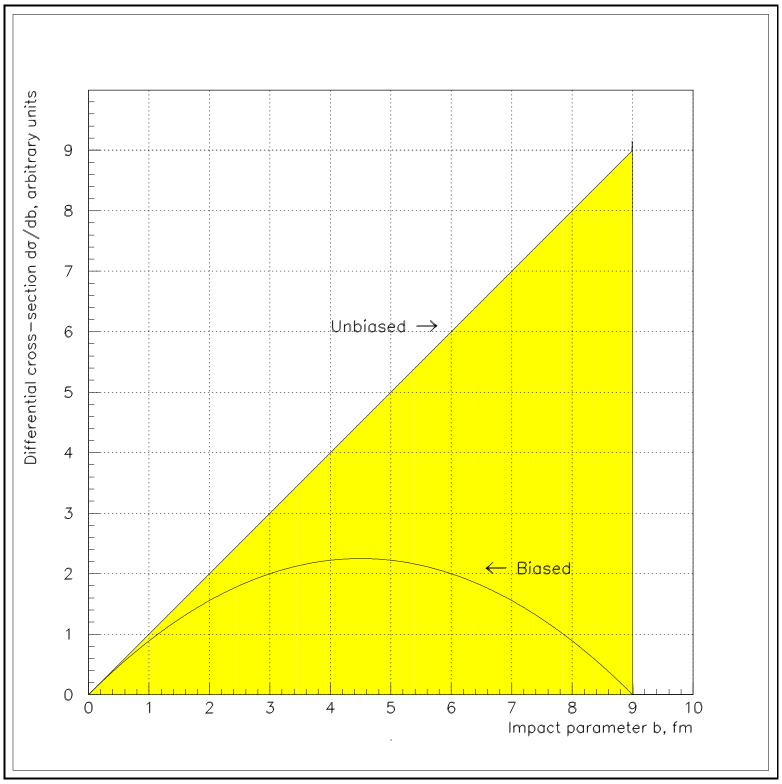

Figure 5.11: A schematic diagram of the differential cross-section $\frac{d\sigma}{db}$ as a function of b for unbiased and central-biased trigger

The actual data are a mix of events with a range of impact parameters, characterized by a certain density function whose shape is defined by the particular trigger bias. It is our goal here to investigate this distribution (which may be similar to the lower curve in Fig. 5.11) in order to take it into account when generating the theoretical proton correlation function.

The approach taken to extract information about the impact parameter can be explained in the following way: we denote the yet unknown distribution of impact parameter b as $\omega(b) = \frac{dN}{db}$, and the distribution of a measured observable x (in our case, the silicon detector multiplicity), for a fixed value of b, as $\theta(x;b)$; the actual distribution of that observable $\Theta(x) = \frac{dN}{dx}$, integrated over all values of b, takes the form

$$\Theta(x) = \int_0^{+\infty} \omega(b)\theta(x;b)db \qquad (5.1)$$

The density function $\Theta(x)$ is measured in the experiment, and we assume that $\theta(x;b)$ is somehow known (for example, from a model). Then we may consider equation 5.1 as an integral equation which we have to solve in terms of $\omega(b)$. We note right away that there are a number of reasonable assumptions that we can make about $\omega(b)$, that dramatically simplify the problem. This assumptions are based on the physics considerations presented above and illustrated in Fig. 5.11:

1. $\omega(0) = 0$ *(the curve must pass through zero)*

2. $\omega'(0) > 0$ *(it must have a positive slope at zero)*

3. $\omega''(b) < 0$ *(the curve has convex shape)*

Since $\theta(x;b)$ can't be measured directly, we use a Monte Carlo calculation to determine it. We understand that there may be a systematic error associated with this calculation and will analyze that error separately.

In our case, $\theta(x;b)$ is the silicon detector multiplicity, for a given (fixed) b. As a practical matter, we would prefer to determine $\theta(x;b)$ for a set of fixed values[14] of b and consider a set of distributions $\theta_{b_i}(x)$, defined for $b_1, b_2, ..., b_i, ..., b_N$. Thus, equation 5.1 becomes, via substitution of the integral by the discrete summation:

$$\Theta(x) = \sum_{i=1}^{N} \omega(b_i)\theta_{b_i}(x) \tag{5.2}$$

i.e. ω is now sampled at points b_i; we assume that N is large enough for that approximation to be reasonably precise. Yet another step in simplification of this equation is to approximate the unknown functional form of $\omega(b)$ by a polynomial, since it would allow a straightforward application of the assumptions listed above, in the form of certain restrictions on the value of the polynomial coefficients[15]. Hence, we come to

$$\Theta(x) = \sum_{i=1}^{N} \mathcal{P}^M(b_i; a_0, ..., a_M)\theta_{b_i}(x) \tag{5.3}$$

where $\mathcal{P}^M(b; a_0, ..., a_M)$ is a polynomial in b, of power M, and a is a vector of its coefficients. Therefore, our task is reduced to determination of a.

[14] i.e. we would like to somehow *parametrize* the unknown function $\theta(x;b)$

[15] and certain relations between them

Implementation

As discussed in section 4.5.2, we chose to use number of pads with signals above a certain threshold as the value characterizing the event multiplicity. The distribution of the number of silicon pads with signal above the threshold is shown in Figs. 4.30 and 4.31 for S+Pb and p+Pb data, respectively.

The basic idea is to extract the impact parameter distribution, as defined in the event generator, by performing a Monte Carlo calculation of the corresponding multiplicity of hits in the Silicon Pad Detector and subsequent matching of that multiplicity to one observed in the experiment. In view of the concept of the method explained above, we perform the following steps:

1. measure $\Theta = \frac{dN}{dn_{ch}}$ – the silicon detector hit multiplicity
2. calculate, via MC, $\theta_{b_i}(x)$, defined for a set of values $b_1, b_2, ..., b_i, ..., b_N$
3. solve the equation 5.3 in terms of the vector a; the resulting polynomial $\mathcal{P}$ is the impact parameter distribution

In order to obtain $\theta_{b_i}(x)$, the chain

`RQMD` events $\Rightarrow$ `GEANT` model of the Silicon Pad Detector $\Rightarrow dN/dn_{ch}$

is repeated for $b_i = 1...N$, and resulting distributions $\theta_i = \left.\frac{dN}{dn_{ch}}\right|_{b_i}$ are then recorded in the form of normalized histograms. We then *perform a fit* of the experimentally measured $\Theta = \frac{dN}{dn_{ch}}$ with $\sum_{i=1}^{N} \mathcal{P}^M(b_i; a_0, ..., a_M)\theta_{b_i}(x)$ (a being a vector of the fit parameters). The polynomial $\mathcal{P}^M(b; a_{fit})$ is then *our estimate* of $\omega(b)$.

Here we summarize the main components of the centrality analysis, from the technical point of view. Items 3 and 4 are a subject of separate sections.

1. Samples of `RQMD` events were generated at fixed values of impact parameter, covering the whole range from very central to very peripheral collisions

2. Events were further propagated through a full-blown `GEANT` simulation of the target area of the detector[16] in order to take into account effects such as photon conversions in the target and other detector elements in the vicinity of the silicon pad detector; also, dE/dx in each pad was calculated, in keV; an example of a distribution of dE/dx in a single pad, for S+Pb events, is shown in Fig. 5.12

3. Distribution of the number of hits was generated for each value of the impact parameter (see discussion below)

4. A fit of the experimental hit multiplicity distribution was then performed with a function that was a linear combination of theoretical curves (see discussion below)

5.3.3 The MC Silicon Multiplicity Distributions

The data from the `GEANT` simulation was written out in the Ntuple format, that carried the dE/dx information for each individual pad. A `FORTRAN` routine callable

[16]since the detector was located in the immediate vicinity of the dipole magnet, it was necessary to calculate the fringe magnetic field

from PAW was used to process these data: similar to the way we treated the exerimental data, a threshold was imposed in order to define a "hit" in the silicon detector pad. Because in MC there were no effects related to electronic noise and resolution, the separation of the pedestal from the signal was well defined, as can be seen in Fig. 5.12. The number of hit pads is calculated by simply looping

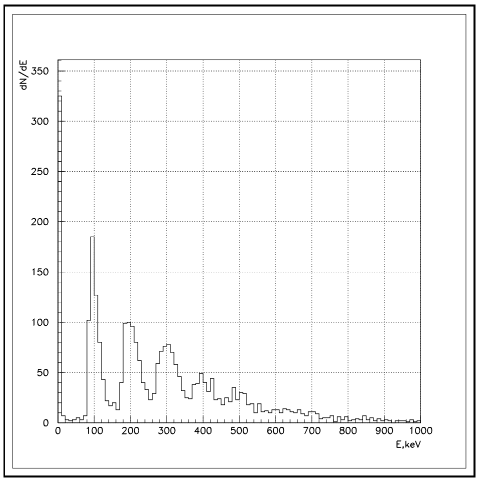

Figure 5.12: Distribution of dE/dx (keV) in a single pad, in a GEANT simulation of the Silicon Pad Detector, with RQMD S+Pb events

over the pads, on event-by-event basis, and incrementing a counter should there be a signal above the threshold. In order to be able to match the MC and the data in a meaningful way, we had to take into account the presence of "dead" channels, which was accomplished by including the actual dead channel map[17], as determined from the detector data, in the calculation.

This procedure, repeated for the S+Pb RQMD data for every impact parameter bin, $b = 1...9$ fm, resulted in a set of histograms of the number of hit pads; an

[17]at one point there were as many as 19 dead channels, i.e. 10% of the total channel count

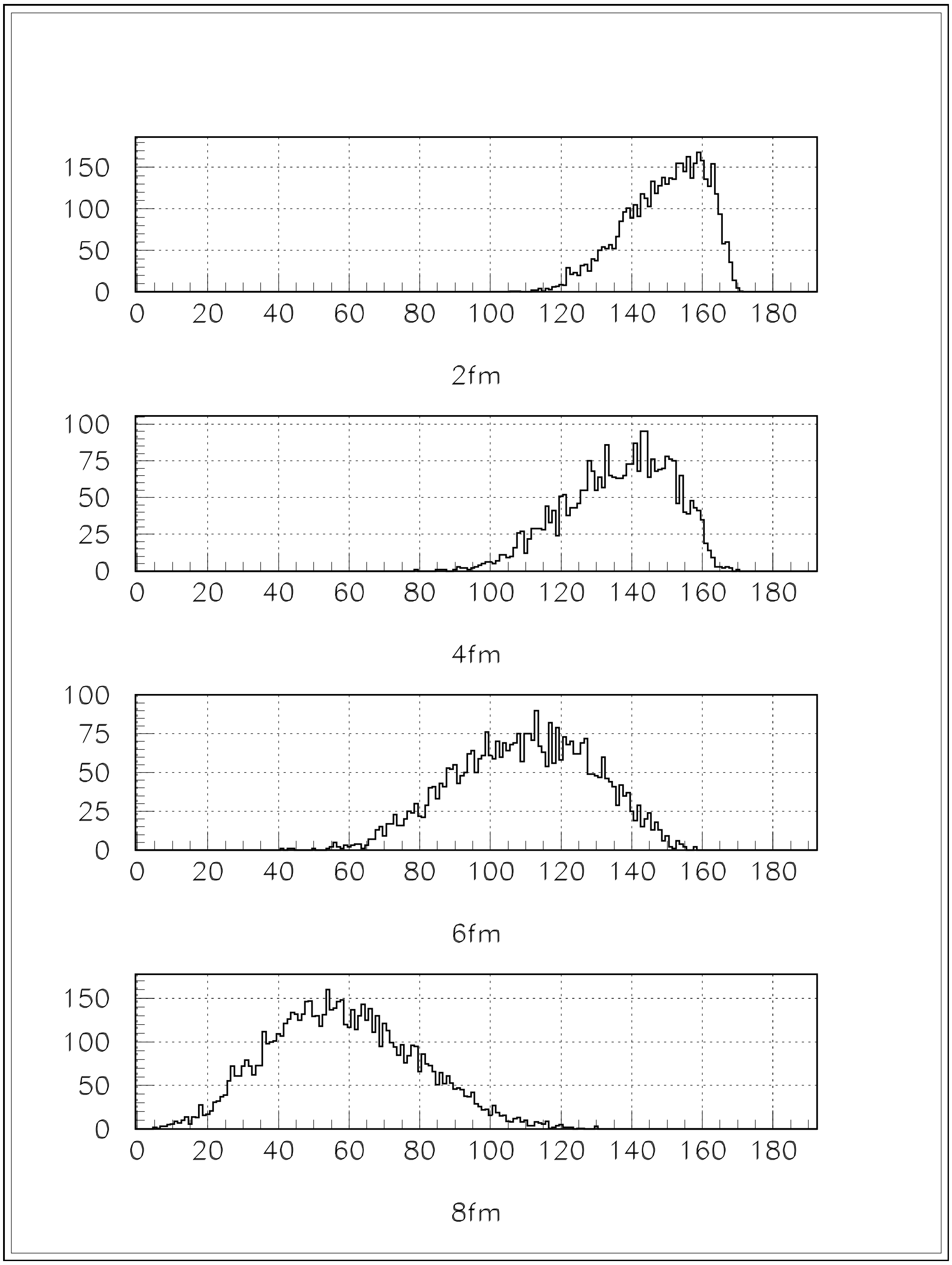

Figure 5.13: Distributions of the number of hit pads, in a `GEANT` simulation of the Silicon Pad Detector, with `RQMD` S+Pb events, for impact parameters 2, 4, 6 and 8 fm

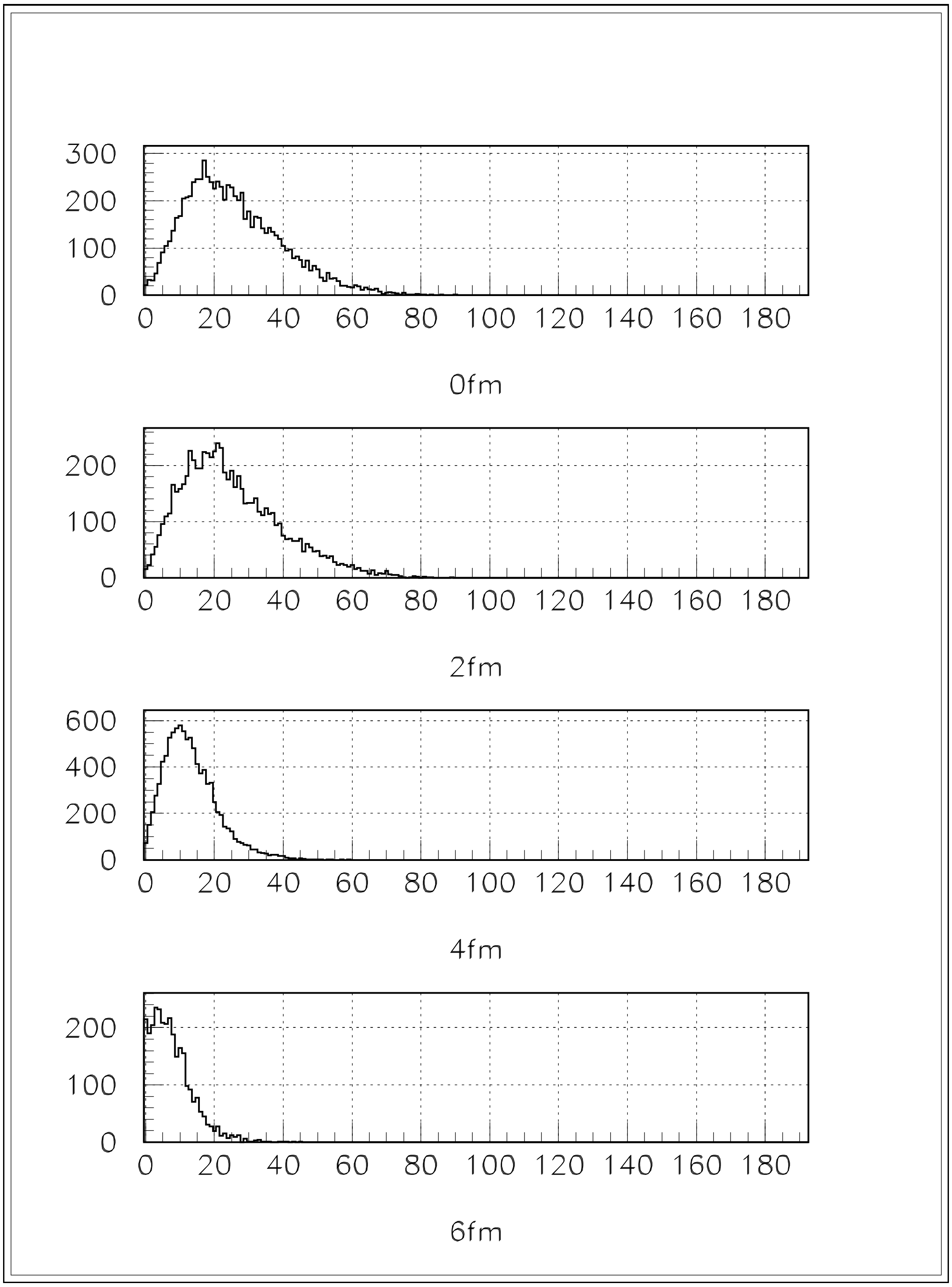

Figure 5.14: Distributions of the number of hit pads, in a `GEANT` simulation of the Silicon Pad Detector, with `RQMD` p+Pb events, for impact parameters 0, 2, 4 and 6 fm

example of such distributions generated at $b = 2, 4, 6, 8$ fm is shown in Fig. 5.13. Analogous distributions for the p+Pb system[18] for $b = 0, 2, 4, 6$ fm are presented in Fig. 5.14. These distributions were then normalized to same number of events in each centrality bin.

The tendency of these MC curves, as can be seen, is such that events for each impact parameter populate certain parts of the multiplicity scale: more central events (with smaller values of the impact parameter b) tend to have larger silicon detector hit multiplicities, whereas peripheral events produce significantly lower number of hits. In view of what has been said about the method we use to estimate the centrality, we can state that the function $\theta(x; b)$ is rather sensitive to b, making the proposed fitting procedure feasible.

From comparison of Figs. 5.13 and 4.30 we conclude that the S+Pb sample was not very strongly biased – the characteristic long tail of the multiplicity distribution must correspond to peripheral events (cf Fig. 5.13). The opposite is true for the p+Pb curves: a cursory inspection reveals that the $b = 0$ fm Monte Carlo curve appears to match the shape of the experimental distribution relatively well[19], meaning that larger impact parameters are likely to be represented with rather small weights. This, in fact, means that the trigger was rather strongly

[18] it is obvious from the curves in Fig. 5.11 that the fraction of events with $b \equiv 0$ fm should be identically zero; however, it will become clear from the following discussion that, in our Monte Carlo scheme, the $b = 0$ sample is simply used to approximate events with *very small* values impact parameter

[19] in the geometrical picture of the heavy-ion collision discussed above, $\omega(0) = 0$, meaning that there are *no events* with $b = 0$, so in fact we assume that this curve represents a set of events with a very narrow range of impact parameters close to 0

biased, i.e. tended to accept very central events. Of course, this needs to be quantified, which is exactly the topic of the following discussion.

5.3.4 Fitting the Data with the MC curves

At this point we have, on the one hand, the measured silicon multiplicity distribution (shown in Figs. 4.30 and 4.31 for S+Pb and p+Pb data), and a set of MC distributions similar to those shown in Fig. 5.13 for the S+Pb `RQMD` data. In order to reduce "statistical noise" and make implementation of the fit more feasible, each of these MC distributions $\theta(b_i)$ was then parametrized with a fifth-order polynomial (quite sufficient to obtain a good quality fit). The equation 5.3 was implemented as a `FORTRAN` routine callable from `PAW`, that contained definitions of both $\theta(b_i)$ and $\mathcal{P}^M$, with a (polynomial coefficients) defined as the vector of the fit parameters. As to the order M of the polynomial $\mathcal{P}^M$, it was empirically found that polynomials of the 3^{rd} order and higher yield very similar results, and it was decided to use $M = 3$.

An important, although somewhat technical, feature of the fit was the following: there was an additional fit parameter[20] that was a multiplicative factor for the argument of the polynomial, i.e. effectively the latter took the form

$$\mathcal{P}^M(a' \times b; a_0, a_1, a_2, a_3)$$

where all a's were fit parameters. The reasons for this factor were:

[20]we should note right away that in any case this factor was close to 1

- as explained in chapter 4, there was a threshold used to define the presence of a hit in a silicon detector pad. The separation of the dE/dx peaks from the pedestal was good but not ideal (Fig. 4.29), i.e. there still was a small probability that a pedestal signal would be recognized as a particle and vice versa

- there were some inefficiencies in the silicon detector, for example due to the space separating individual pads (that was not sensitive), that were hard to take into account and could affect the measured hit multiplicity on a percent level

- one can expect small deviations of the multiplicities predicted by the event generator from their actual values

- there could be some small systematic errors in the `GEANT` simulation

- due to pile-up effects in the detector we had to to introduce "dynamical correction" (see section 4.5.2) that itself is very likely to err on at least a percent level

The magnitude of all these effects combined was not large and the final value of a' was about 1.07, i.e. reasonably close to the "ideal" value of 1.0.

Having performed the fit (see Fig. 5.15), we can effectively use $\mathcal{P}^M(b; a_{fit})$ as our estimator of $\omega(b)$, the event centrality distribution. The uncertainty associated with this estimate will be a subject of one of section 5.6.

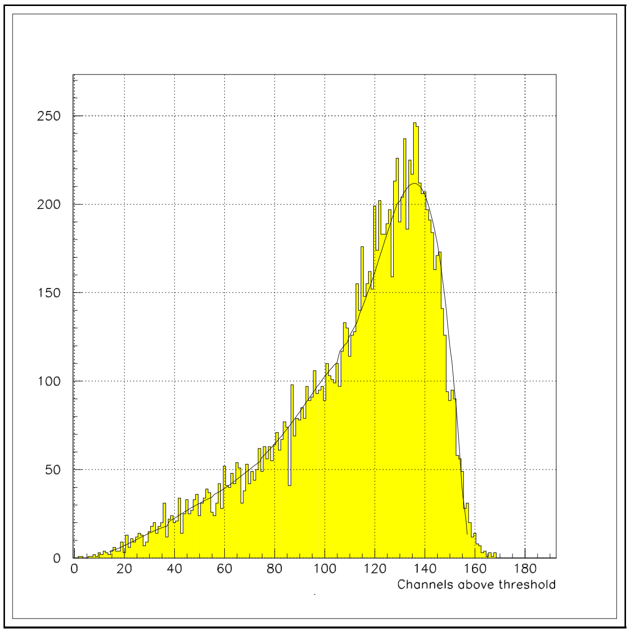

Figure 5.15: The distribution of the number of hit pads, S+Pb data, with a Monte Carlo fit

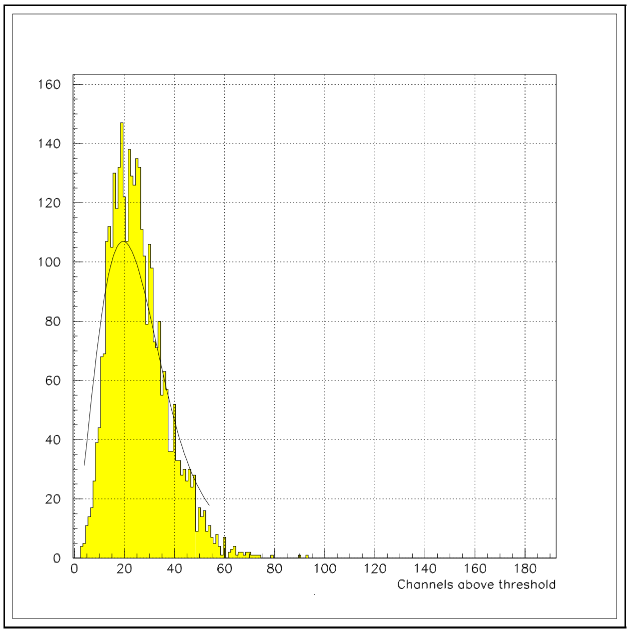

Figure 5.16: The distribution of the number of hit pads, p+Pb data, with a Monte Carlo fit

This procedure was successfully used on the S+Pb data. As already mentioned in the previous section, comparison of the Monte Carlo and experimental p+Pb multiplicity distributions (Fig. 5.14) indicates that the impact parameter distribution was rather narrow and characterized by small values of b. Because of this narrowness, the original fitting procedure was simplified: the available `RQMD` samples[21] at $b = 0, 2, 4$ and 6 fm (see Fig. 5.14) were each assigned a weight w_i and the fit took the form

$$\Theta(x) = \sum_{i=1}^{4} w_i \theta_{b_i}(a' \times x)$$

The fit[22], superimposed on the data, is shown in Fig. 5.16, and it corresponds to $w_{0fm} = 1$ and $w_{2,4,6fm} = 0$, meaning that we have to assume very high centrality for the p+Pb event sample, i.e. simply use b=0 fm in our calculations.

5.3.5 The Centrality Estimate

The distribution of b obtained for the S+Pb data set is shown in Fig. 5.17. We conclude that the trigger was moderately biased towards central events. It was used as input for the calculation of the S+Pb correlation function, where the `RQMD` events were appropriately weighted (section 5.2.1). The exact values of these weights for impact parameters 1...9 fm are listed in table 5.5 as "standard weights".

[21] as mentioned already, we assume that $b = 0$ sample represents a set of events with a very narrow range of impact parameters close to 0

[22] a', the scaling factor, was very close to 1

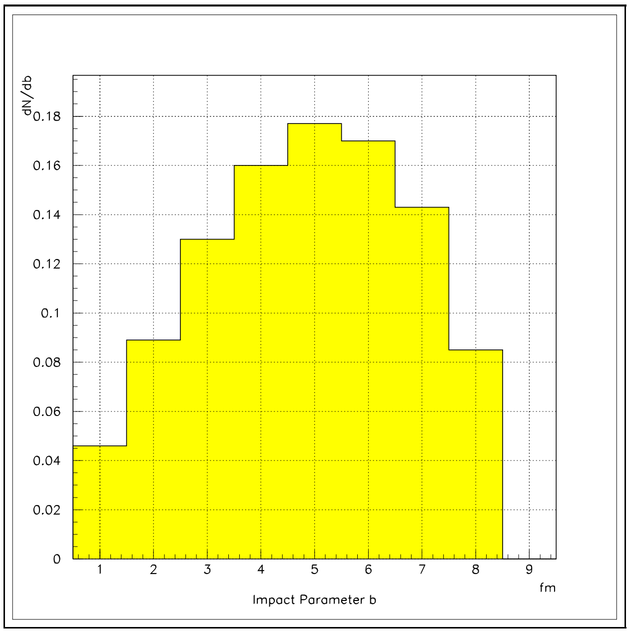

Figure 5.17: The Impact Parameter Distribution (S+Pb)

As explained above, based on the fit results, we chose use very central events ($b = 0$ fm) for our calculation of the p+Pb correlation function.

5.4 The Strange Baryon Contribution

As already mentioned in the introduction to this chapter and in chapter 2, the decay $\Lambda \rightarrow p + \pi^-$, as well as decays of other strange baryons, potentially are an important source of protons that would affect the shape of the measured correlation function. Pairs that contain protons coming from Λ decays are effectively uncorrelated, and assuming we can treat such pairs in the same way as "background" pairs (in the sense of the correlation function definition, see section 2.2.1) we can modify our calculations in order to see what effect such "dilution" of the

q_{inv} spectra can have. We have done this for several different levels of such "Λ contamination", and Fig. 5.18 shows the results (and the sensitivity of the correlation function to Λ's). In the rest of this chapter, unless otherwise noted, all the calculations are done assuming the distribution of impact parameter (centrality) obtained in the way explained in the previous sections.

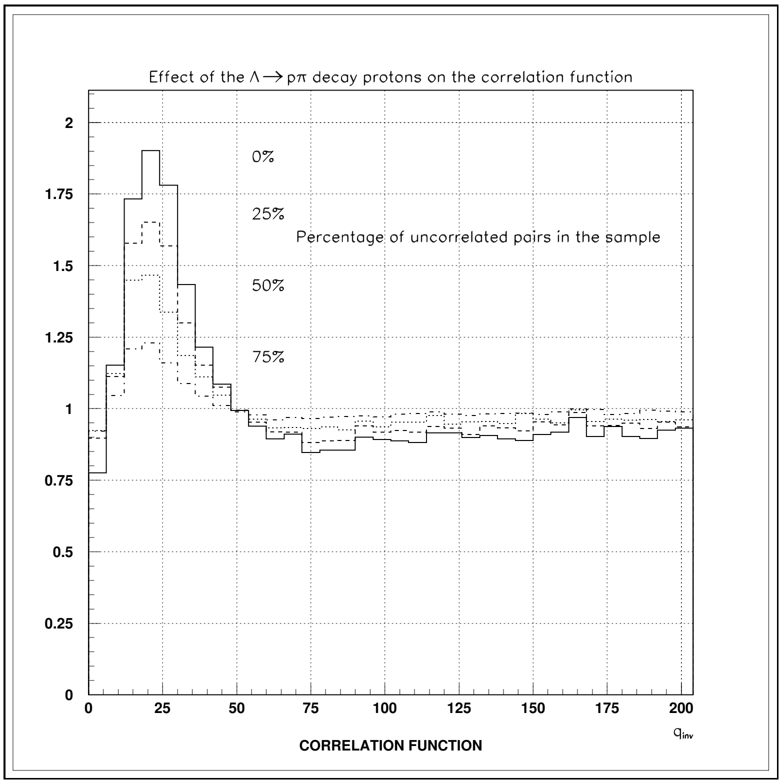

Figure 5.18: The effect of "Λ dilution" on the calculated Correlation Function (RQMD S+Pb events at 200 GeV/c), assuming different levels of Λ contribution (two-particle resolution included).

To illustrate the point, let's take a look at the *absolute* yields, over the whole rapidity range, of Λ's and protons, as predicted by RQMD (see table 5.2). The rapidity profile of Λ's according to RQMD is presented in Fig.5.19. Of course, this

Table 5.2: Absolute yield of Λ and protons at different impact parameter values (RQMD)

Impact Parameter, fm	2	4	6	8
N_Λ	12.5	9.6	5.9	2.2
N_p	100.2	99.8	99.7	99.0

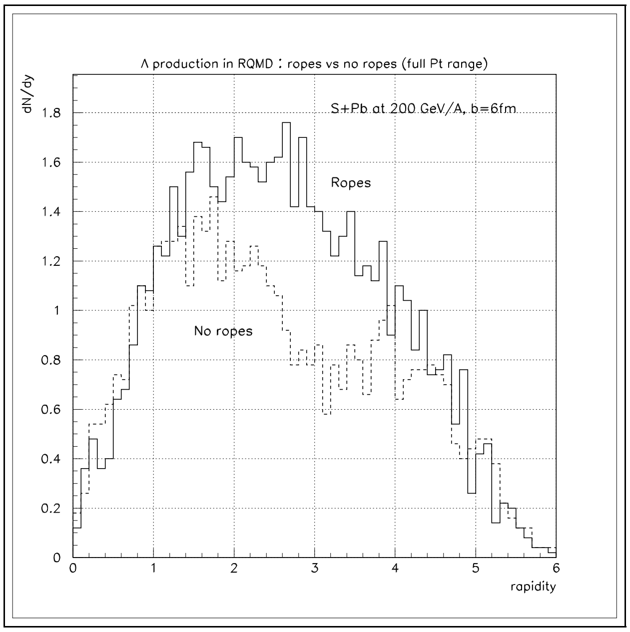

Figure 5.19: Λ rapidity distribution from RQMD S+Pb collisions, for a particular impact parameter

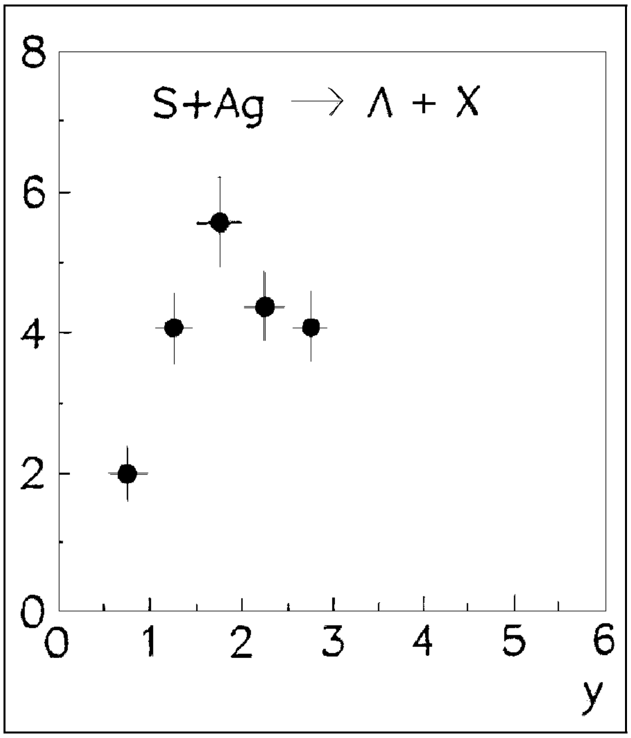

Figure 5.20: Λ rapidity distribution from NA35, extrapolated to full transverse momentum range

is just a starting point, since

1. we don't know what is the Λ "detection efficiency", i.e. probability that the decay proton will be successfully reconstructed

2. the numbers in the table 5.2 are for *all* rapidities, whereas the NA44 acceptance is limited in y, and in the particular setting we are considering is essentially a narrow slit at around mid-rapidity (see chapter 3). It is known [45, 46] that dN/dy distribution of the produced Λ's peaks somewhere between target and mid-rapidity and falls off on both sides (for illustration purposes we present Figs. 5.20 and 5.19), whereas the dN/dy of protons in asymmetric systems peaks at the target rapidity and then tapers off, hence, in case of the NA44 acceptance, the Λ/p ratio will be significantly larger

To resolve these issues[23], a more detailed MC study is needed [24]. The idea behind it is rather straightforward: we start with the `RQMD` data sample and a `GEANT` simulation of the detector (in order to describe the acceptance in most realistic way), and use the standard NA44 tracking procedures. Then, Λ's are propagated through the apparatus and one keeps track of the number of protons that were successfully reconstructed – "direct" and coming from Λ decays. The results can be used to estimate the ratio $\epsilon = \frac{N_\Lambda}{N_p + N_\Lambda}$, that is the fraction of protons coming

[23]There is a separate issue of how realistic is the `RQMD` simulation of the Λ production and how it relates to the available experimental data, which has direct bearing on the overall systematic uncertainty of our calculation and will be discussed in detail later

[24]a lot of credit for this study goes to J.Sullivan

from Λ decays in the total number of protons. These results are presented in table 5.3 (N_p and N_Λ are normalized per event).

Table 5.3: Number of successfully reconstructed RQMD protons, per event, at different values of the impact parameter (S+Pb)

Impact parameter, fm	2	4	6
N_p (Number of "true" protons, per event)$\times 10^2$	2.34	1.58	1.05
N_Λ (Protons from Λ decays, per event)$\times 10^2$	0.69	0.49	0.29
$\epsilon = \frac{N_\Lambda}{N_p+N_\Lambda}$	0.22	0.23	0.22

It turns out that $\epsilon = \frac{N_\Lambda}{N_p+N_\Lambda}$ does not show appreciable dependence on the impact parameter[25], therefore, it makes sense to take average over the whole range of centrality, with the result being $\epsilon_{average} = 22\%$. In a similar way, we repeated the simulation for p+Pb collisions, and the result came out to be also very close to 22% (see table 5.4).

Table 5.4: Number of successfully reconstructed RQMD protons, per event, at two different values of the impact parameter (p+Pb)

Impact parameter, fm	0	2
N_p (Number of "true" protons, per event)$\times 10^3$	1.07	0.93
N_Λ (Protons from Λ decays, per event)$\times 10^3$	0.19	0.17
$\epsilon = \frac{N_\Lambda}{N_p+N_\Lambda}$	0.22	0.23

However significant this factor is, it becomes even more dramatic when we estimate the fraction of the observed proton pairs that are composed of, so to

[25] within the available statistics

speak, "true" protons, "lambda" protons and their combinations. For example, assuming $\epsilon = 22\%$, the fraction of uncorrelated pairs where at least one of the particles is a decay proton is:

$$f_{uncorr} = 2\epsilon(1-\epsilon) + \epsilon^2 = 40\%$$

This appears to be a significant factor among others that define the shape of the correlation function and must somehow be taken into account. The effect of such

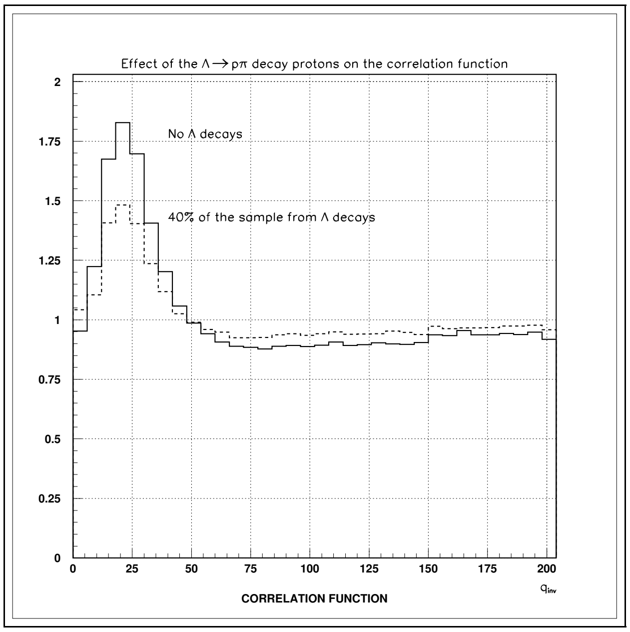

Figure 5.21: The effect of "Λ dilution" on the calculated Correlation Function (RQMD S+Pb events at 200 GeV/A), assuming 40% level of Λ contribution.

"Λ dilution" on the calculated Correlation Function is illustrated in Figs. 5.21 and 5.22, for S+Pb and p+Pb systems, respectively.

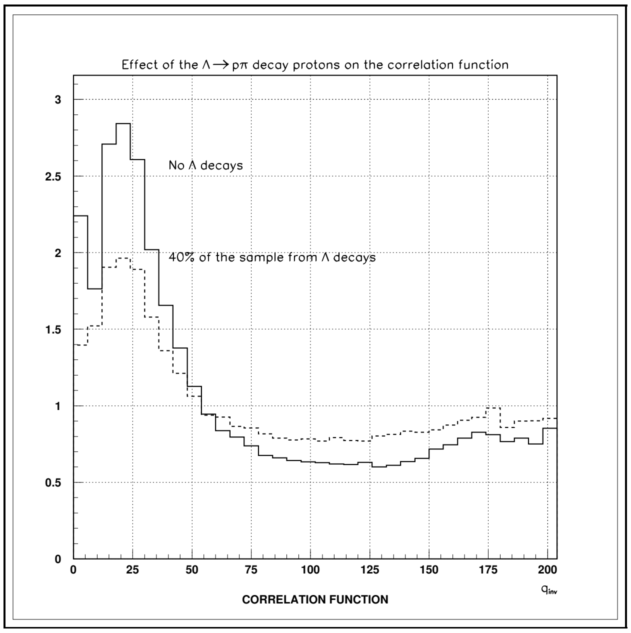

Figure 5.22: The effect of "Λ dilution" on the calculated Correlation Function (`RQMD` p+Pb events at 450 GeV/c), assuming 40% level of Λ contribution.

5.5 The Results of the Monte Carlo

We present the theoretical correlation function calculated for S+Pb and p+Pb systems[26], without systematic errors, in separate plots in Figs. 5.23 and 5.24.

The analysis of the systematic uncertainty of these calculations, coming from various parts of the Monte Carlo, is the topic of the next section.

[26] assuming $f_{uncorr} = 40\%$

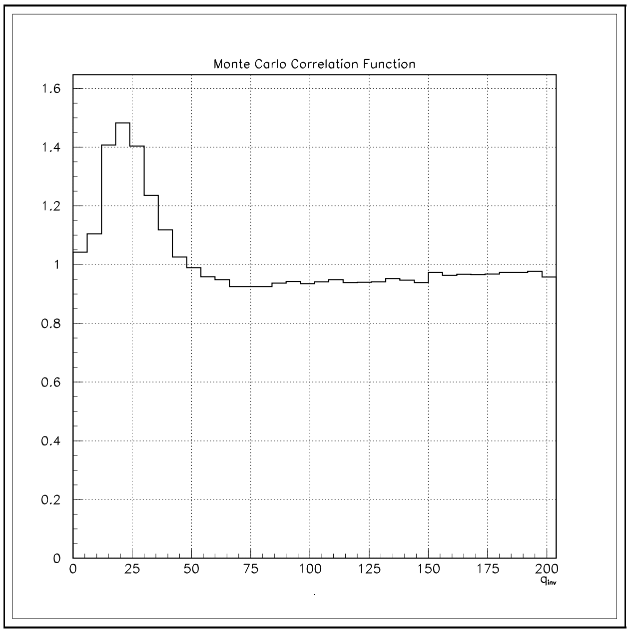

Figure 5.23: The theoretical Correlation Function (`RQMD` S+Pb events at 200 GeV/A), full MC.

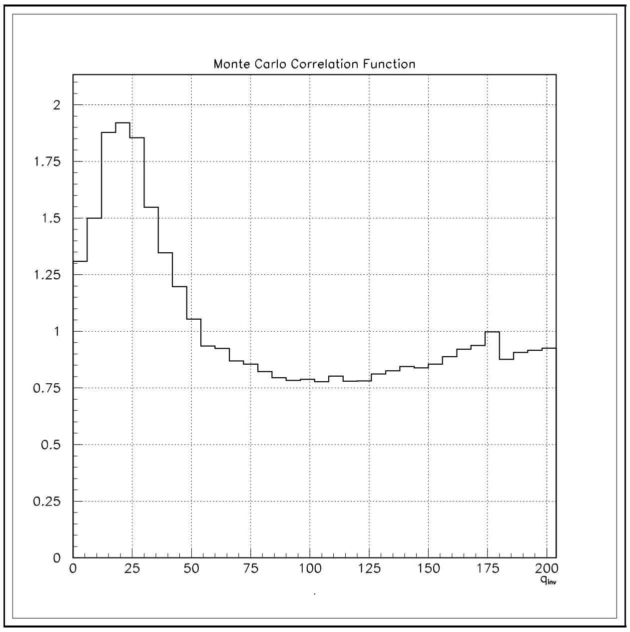

Figure 5.24: The theoretical Correlation Function (`RQMD` p+Pb events at 450 GeV/c), full MC.

5.6 The Uncertainty Margin of the Monte Carlo

5.6.1 Main Sources of Uncertainty in the Monte Carlo

As was explained earlier in this chapter, the Monte Carlo scheme had, among others, the following components:

1. TURTLE-based simulation of the NA44 detector

2. The event centrality estimate

3. Estimate of the momentum-dependent efficiency of the m^2 cut

4. Estimate of the Λ decays contribution

Each of these components carries a certain margin of systematic error due to the fact that our knowledge of some parameters (for example, details of Λ production) is approximate, some parts of the data that served as input to the MC were not without problems, and finally, Monte Carlo itself is only an approximation of physical processes.

In the above list, items 1–3 are related to the properties of the MC simulation itself. Item 4 is, in a certain sense, *external to the model:* as we will see, the existing data on Λ production, from different experiments, differ from each other and from the RQMD predictions. As follows from the analysis of the Λ contribution presented above, it is a relatively large factor that influences the correlation function, hence, its uncertainty may be (and as we will see, indeed is) a very important component in the overall systematic error in our simulation.

In the following, we will analyze the margin of systematic error associated with each relevant part of the MC *per se* (items 1–3 in the above list) and how it affects the overall accuracy of the calculated pp correlation function. Then, in a separate section, a discussion will be presented of how variations of one aspect of the `RQMD` model, the Λ production, can influence the results of the Monte Carlo, and how the existing data can be used to estimate the magnitude of this influence.

5.6.2 Systematic Uncertainty of the `TURTLE` Simulation

As has been explained in sections 5.2.1 and 5.2.4, the effects related to the two-particle acceptance and momentum resolution of the spectrometer are taken into account by propagating, in Monte Carlo, pairs of protons through the detector and using the same track reconstruction software that was used to process the experimental data. Such simulation may carry a degree of systematic uncertainty associated, for example, with the way the multiple scattering was calculated. To make sure the MC result is robust, it is instructive to vary some parameters of the simulation and check the results' sensitivity to such variations. Since the multiple scattering in the target was the leading contribution to the overall momentum resolution[27], the most straightforward exercise of that sort is to change the target thickness within certain limits and watch behavior of the correlation function.

It was decided that a $\pm 20\%$ change of the target thickness is a sufficiently

[27]we remind the reader that S+Pb data was taken with a 5 mm lead target and p+Pb with a 10 mm lead target

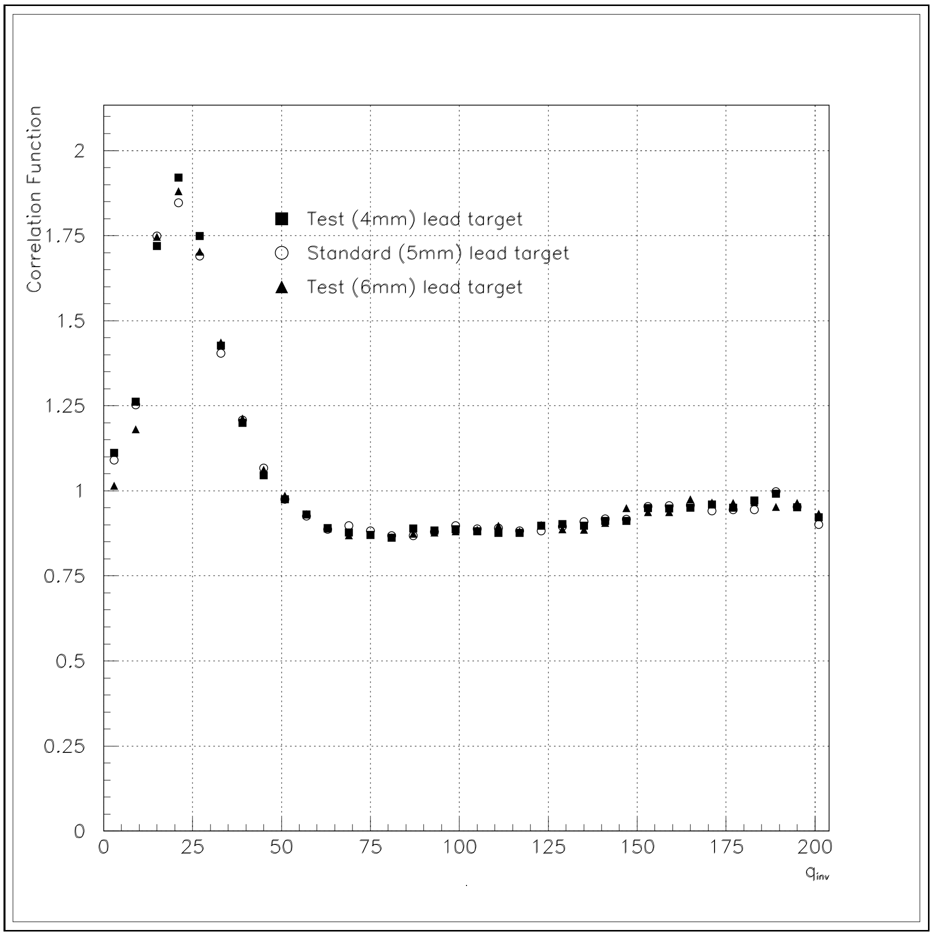

Figure 5.25: The stability of the calculated Correlation Function with respect to variation of the target thickness, S+Pb system (Λ decays not included); shown are results for 4, 5 and 6 mm Pb target (the actual value was 5 mm)

conservative estimate of the uncertainty of the Monte Carlo momentum resolution. To this end, we performed a dedicated MC study with a mix of 2,4,6 and 8 fm `RQMD` data, with realistic centrality distribution; we did not include the effects related to Λ decays in order to be able to see the momentum resolution effects more clearly.

The results, shown in Fig. 5.25, indicate that at this level the correlation function is insensitive to such variations. Closer inspection of this plot reveals that there's no systematic shift of $C(q_{inv})$ due to the different scale of the multiple scattering effects[28], and whatever small spread is present has the character of statistical fluctuation.

5.6.3 Systematic Uncertainty due to the Centrality Estimate

It follows from the discussion of the procedure used to obtain the centrality estimate in section 5.3.4 that the impact parameter distribution extracted from the silicon detector data, via solution of equation 5.3, can be affected by systematic uncertainty. Our approach will be to show that main features of the S+Pb centrality distribution shown in Fig. 5.17, such as peaking at about 5–6 fm and falling off at 8–9 fm, remain sufficiently stable under variety of assumptions and procedures, and so does the centrality estimate for the p+Pb data. We will also verify the stability the correlation function calculated with varying centrality distributions.

[28] had the correlation function been more sensitive to this parameter, one would expect a *flatter* curve for the thicker target and a *sharper* curve for the thinner one

In the following we will focus on the S+Pb data; we shall comment on the p+Pb centrality systematics later in this section. As already discussed in sections 4.5.2 and 5.3.4, the silicon detector data suffered from pile-up events, where signals from a certain number of pads, varying from event to event, were distorted and had large amplitudes unrelated to the actual dE/dx in the pad. This was demonstrated in Fig.4.29, where the dE/dx spectrum had a long, non-physical tail. We have also discussed the way to correct the problem by means of excluding such pads from consideration, on event-by-event basis, and correspondingly correct the event multiplicity ("dynamical correction", section 4.5.2). To answer the question of the systematic uncertainty associated with that procedure, we decided to modify it in such a way that the pads with non-physical signals were simply discarded and the resulting inefficiency is absorbed in one of the fit parameters, a' (section 5.3.4). This way we do not make any assumptions about the nature of inefficiency or the corresponding correction and only rely on the scaling factor a' to reconcile the data and the MC. The resulting polynomial was used to calculate "modified" weights of

Table 5.5: Event centrality in S+Pb collisions: weights of individual impact parameter bins and their systematic shift, S+Pb data

Impact parameter b, fm	1	2	3	4	5	6	7	8	9
"standard" weights, $\times 10^2$	4.6	8.9	13.0	16.0	17.7	17.0	14.3	8.5	0.0
"modified" weights, $\times 10^2$ (see text)	4.6	8.8	12.2	14.6	15.7	15.7	13.9	10.1	4.3

individual centrality bins; the results, in comparison with the "standard" weights, are shown in table 5.5. It can be seen that the distribution has slightly shifted in the direction of large impact parameters. In order to see what effect is has on the correlation function, we performed the requisite calculations and present the comparison of the "modified" vs "standard" centrality in Fig.5.26. Apparently,

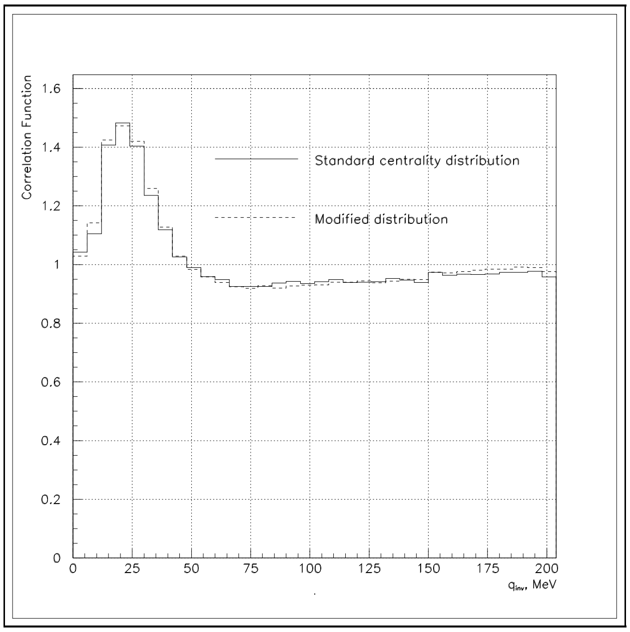

Figure 5.26: S+Pb Proton Correlation Functions Calculated with "Standard" and "Modified" Centrality Distributions (see text)

the sensitivity of the result to such modifications of the procedure is minimal. For an additional check of the stability of the result, we decided to consider an extreme case: the "modified" weights presented in table 5.5 were modified even further such that impact parameter bins 1 and 2 fm were excluded entirely and their weights were added to bins of 9 and 8 fm, respectively[29].

Our conclusion (see Fig.5.27) is that even in that case (not likely realized) the

[29]obviously, such procedure is rather artificial and is aimed at estimating what would happen in the "worst case scenario", when the centrality estimate is seriously flawed

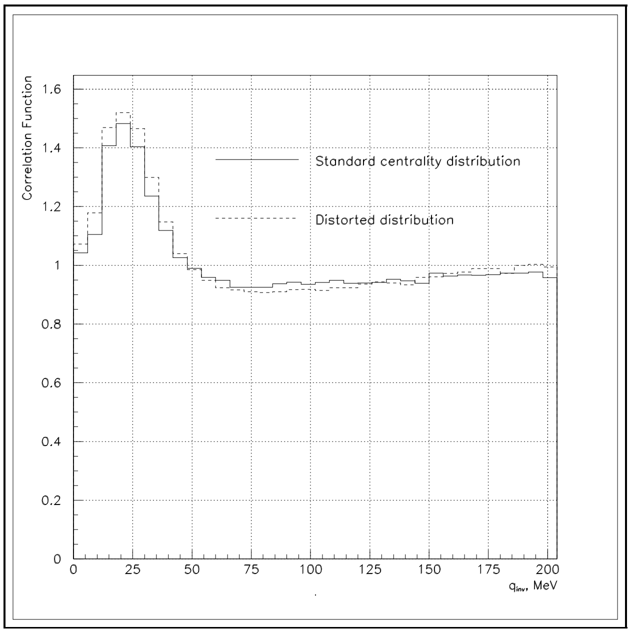

Figure 5.27: S+Pb Proton Correlation Functions Calculated with “Standard” and “Distorted” Centrality Distributions (see text)

respective changes in $C(q_{inv})$ are still moderate[30].

Similar procedures were carried out for the p+Pb data. It turns out that the multiplicity distributions are rather stable and the fit always tends to converge to the $b = 0$ fm result (see section 5.3.4). In any case, to verify the stability of the MC correlation function with respect to the centrality estimate, we performed a calculation for $b = 2$ fm and present comparison with the $b = 0$ correlation function in Fig. 5.28 (as can be seen, the variation, relative to the amplitude of the peak, is small).

[30]we will show in section 5.7 that the uncertainty due to the Λ decays constribution is still a larger factor

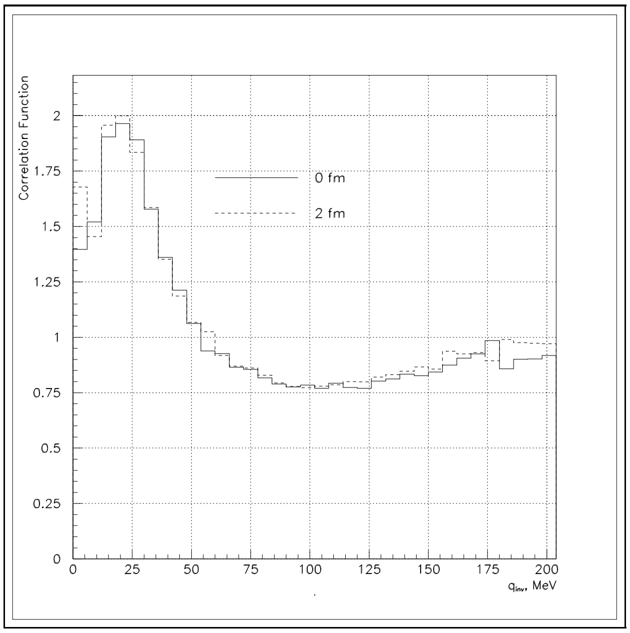

Figure 5.28: p+Pb Proton Correlation Functions Calculated with "Standard" ($b = 0$ fm) and "Distorted" ($b = 2$ fm) Centrality Distributions (see text)

5.6.4 The Momentum-Dependent Efficiency of the m^2 Cut

In section 4.4.6 we addressed the issue of the momentum dependence of the efficiency of the m^2 cut. As we mentioned in our discussion of the "final mixing" part of the Monte Carlo, we use the parametrized m^2 distributions (Figs. 4.25 and 4.26) to calculate, for each particle, the appropriate efficiency factor. The magnitude of the effect of this efficiency is illustrated in Figs. 5.29 and 5.30, for S+Pb and p+Pb systems. As can be seen, the effect itself is not large. In a separate calculation, aimed at determination of its systematic uncertainty, we varied the values of the m^2 cutoff in a way similar to the stability test we performed on the experimental data (section 4.4.6). It turns out that the corresponding variations

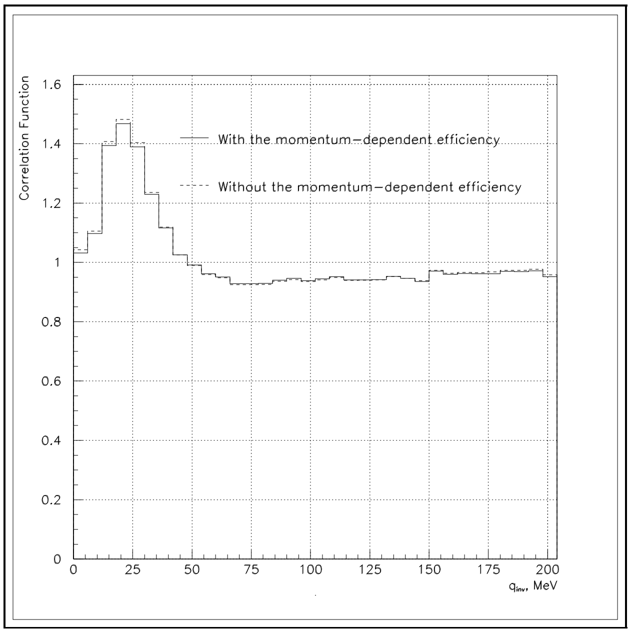

Figure 5.29: The magnitude of the effect of the Momentum-Dependent Efficiency on the Correlation Function, S+Pb MC

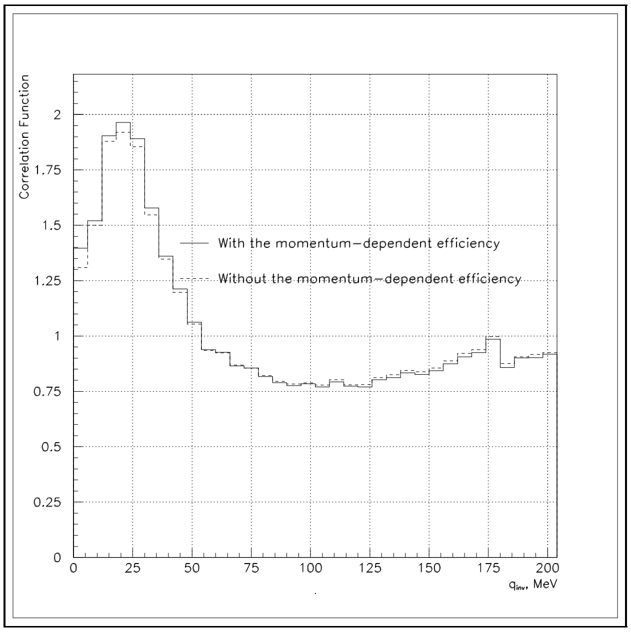

Figure 5.30: The magnitude of the effect of the Momentum-Dependent Efficiency on the Correlation Function, p+Pb MC

of the correlation function are quite negligible.

5.7 Uncertainty Associated with Λ Decays

Experimental data on Λ production

At the time this thesis is being written, there exist data from two experiments, NA35 and NA36, that studied production of Λ in heavy-ion collisions, in the central rapidity region [45, 46]. It is unfortunate that at present there is a significant disagreement between the results of these two experiments, and that is illustrated in figure 5.31 taken from [46]. There the ratio Λ/n^- is plotted as a function of negative multiplicity, allowing to compare results for different systems. As can

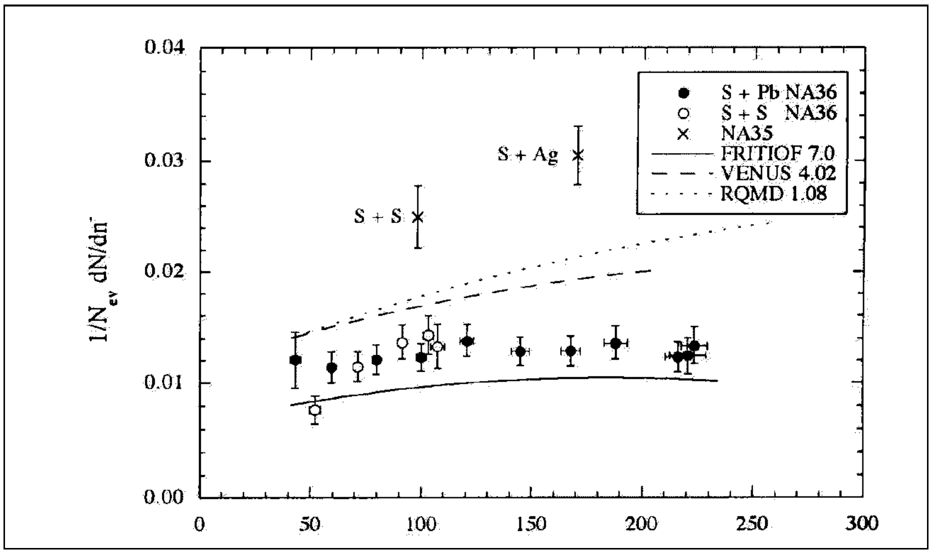

Figure 5.31: Λ/n^- from NA36, NA35 and three theoretical models in the region $1.5 \leq y \leq 3.0$ and $0.4 \leq p_t \leq 1.8$ GeV/c

be seen, the model we use as a reference, RQMD 1.08, predicts Λ yields at levels that are, roughly, the median of these two measurements. Also, in Fig. 5.32 the Λ rapidity distribution[31] is plotted as a function of rapidity [46]. Having this com-

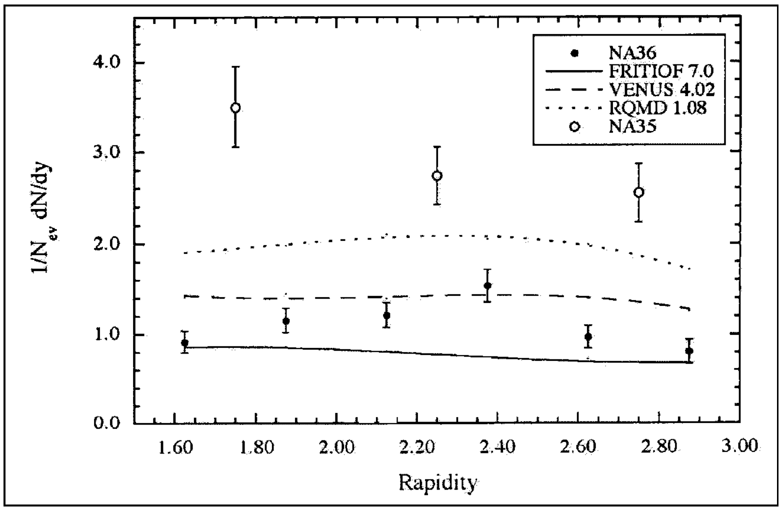

Figure 5.32: Λ rapidity distribution from NA36, NA35 and three theoretical models in the region $1.5 \leq y \leq 3.0$ and $0.4 \leq p_t \leq 1.8$ GeV/c

parison available presents an opportunity to estimate the margin of systematic uncertainty of the Λ yields. In the rapidity range of interest it is roughly $\pm$ 35%. Based on the previously determined value of ϵ (see table 5.3) and using a simple error propagation, we obtain the following[32]:

$$\epsilon = (22 \pm 6)\%, f_{uncorr} = 40^{+8}_{-11}\%$$

We can now use these numbers to determine, via Monte Carlo, the margin of uncertainty this imposes on the correlation function that we calculate (see Fig. 5.33).

[31] the NA35 data points were scaled by the ratio of negative particle multiplicities

[32] we remind the reader that f_{uncorr} is the fraction of *uncorrelated* pairs in the sample from which the correlation function is generated

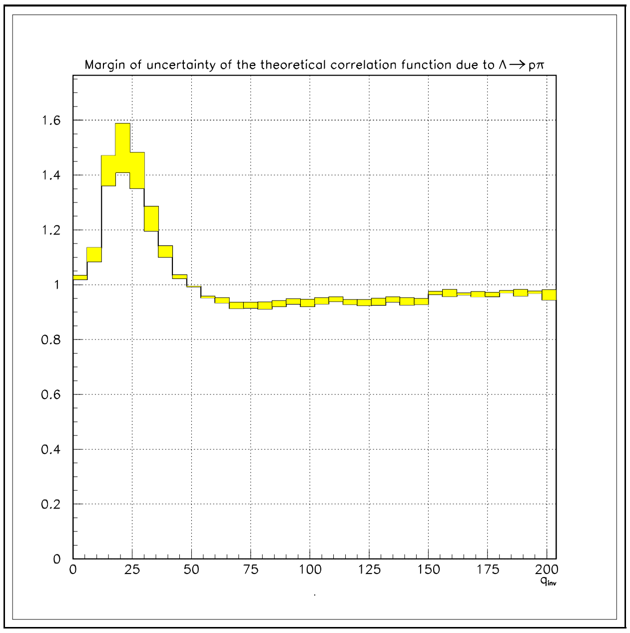

Figure 5.33: The margin of systematic uncertainty of the calculated Correlation Function due to Λ decays, S+Pb system

Similarly, let us estimate the uncertainty associated with Λ decays, for p+Pb system. The production of Λ in p+Pb collisions was studied by NA36 [47]. In Fig. 5.34, the dN/dy distribution of Λ's is presented and compared to three models, including `RQMD` 1.08, in the p$_t$ range $0.6 < p_t < 1.6$.

Note that in the rapidity interval of interest, 2.3–2.8, $\epsilon_{rqmd} = 22\%$ and the `RQMD` predictions are, roughly, 35 to 40% higher than the data. In absence of an equivalent measurement by NA35, it makes sense to assume a "corridor" for the value of ϵ defined as $\pm|\epsilon_{\mathrm{RQMD}} - \epsilon_{\mathrm{NA36}}|$, which is equivalent to

$$\epsilon = (22 \pm 7)\%, f_{uncorr} = 40^{+10}_{-12}\%$$

The corresponding range of the correlation function values is shown in Fig. 5.35.

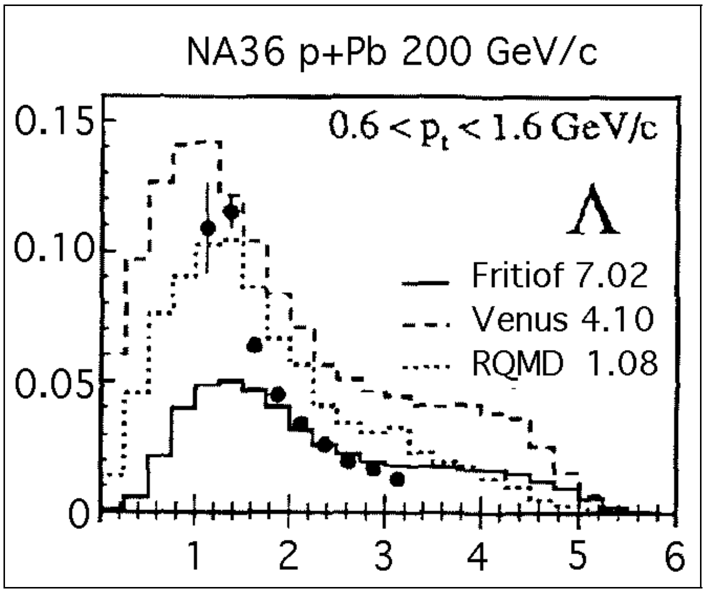

Figure 5.34: Λ rapidity distribution from NA36 (p+Pb collisions) and three theoretical models in the region $0.6 < p_t < 1.6$ GeV/c

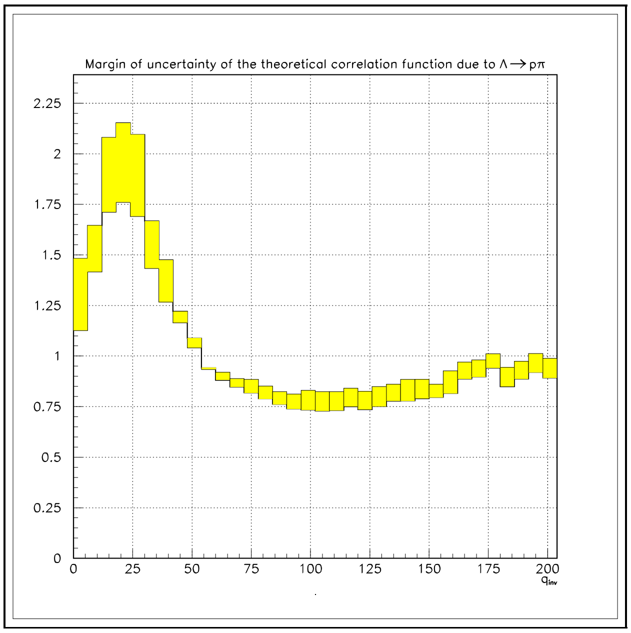

Figure 5.35: The margin of systematic uncertainty of the calculated Correlation Function due to Λ decays, p+Pb system

Other sources of protons and Λ's

For the sake of completeness, let's consider other strange baryons that may contribute to the overall number of observed protons (table 5.6). Acceptance for the

Table 5.6: Yields (RQMD at b=4fm) and decay modes of particles that may contribute to the overall number of protons

Particle	N	Decay mode (branching ratio)	$c\tau$
p	99.8	–	–
Λ	9.6	$\Lambda \to p + \pi^-$ (63.9%)	7.9
Σ^+	2.8	$\Sigma^+ \to p + \pi^0$ (51.6%)	2.4 cm
Σ^0	2.8	$\Sigma^0 \to \Lambda + \gamma$ (100%)	2.2×10^{-11} m
Ξ^0	1.3	$\Xi^0 \to \Lambda + \pi^0$ (99.5%)	8.7 cm
Ξ^-	1.3	$\Xi^- \to \Lambda + \pi^-$ (99.9%)	4.9 cm

last particle, Ξ^-, is negligible because of its negative charge; Ξ^0 has $c\tau$=8.7 cm, and, taking into account the Lorentz boost, must decay somewhere inside dipole 1 (see chapter 3), with the resulting Λ's going even further downstream and more likely to miss the aperture of the quadrupole magnet. In general, we conclude that Σ^0 and Σ^+ are probably the only other source of protons that deserves attention[33]. However it is still much weaker than Λ. Given the generous margin of systematic uncertainty we assumed for the Λ yields and absence of reliable dN/dy data for Σ's, it makes sense to disregard their contribution in the framework of our MC.

[33]note that Λ's coming from Σ^0 decays ($c\tau = 2.2 \times 10^{-11}$ m) are already included in the measured Λ yields and therefore effectively included in our analysis of the systematic uncertainty

5.8 Summary of the Systematic Uncertainty

We have analyzed various sources of systematic uncertainty, inherent in several components of our Monte Carlo scheme, including the `TURTLE`-based simulation of the NA44 detector, the event centrality estimate and the momentum-dependent efficiency of the m^2 cut. Our general conclusion is that the calculated correlation function, for both S+Pb and p+Pb systems, is rather stable under reasonable variations of the parameters and procedures of the Monte Carlo.

We have also analyzed a factor that is *fixed* in the framework of the model – the Λ decays constribution. We have shown, however, that the existing data on the Λ production indicate that the model predictions concerning Λ's may carry a degree of systematic error that can have a significant effect on the uncertainty of the correlation function. In particular, thus accrued systematic error is actually larger than other factors intrinsic to the MC scheme, quoted above.

Chapter 6

Discussion of the Results

6.1 Introduction

In this chapter, we are going to discuss the results of our study of two-proton correlations, with emphasis on the comparison of the data and the theory. Since this discussion is based on various aspects of both data and Monte Carlo that we considered in the preceding chapters, it seems logical to summarize here what has been done so far.

In chapter 4, we presented

- The experimental data
- Procedures used to extract the proton pair sample from the data
- The measured proton correlation function for the S+Pb and p+Pb systems
- The stability of the correlation function with respect to the PID cuts
- The dependence of the measured proton correlation function on the event multiplicity as measured by the silicon pad detector

In chapter 5, the discussion included

- General structure of the MC scheme
- Main components of the MC, such as the RQMD event generator, simulation of the NA44 apparatus, and the event centrality estimate that was based on matching the silicon detector multiplicity as calculated in a GEANT-based Monte Carlo with the observed values
- Fraction of protons coming from strange baryon decays (such as $\Lambda \to p\pi^-$), which will effectively "dilute" the observed correlations
- Analysis of the systematic uncertainty in various components of the Monte Carlo calculation
- Analysis of the systematic uncertainty associated with a particular aspect of the RQMD model – strange baryon production

We will now turn to the discussion of the analysis results.

6.2 The Data and the MC results

The two-proton correlation function calculated based on the experimental data was presented earlier, in Figs. 4.16 and 4.17 for S+Pb and p+Pb systems, respectively. The "baseline" Monte Carlo results (with no systematic errors) are shown in Figs. 5.23 and 5.24. Here we present these curves superimposed on the data points (Figs. 6.1 and 6.2).

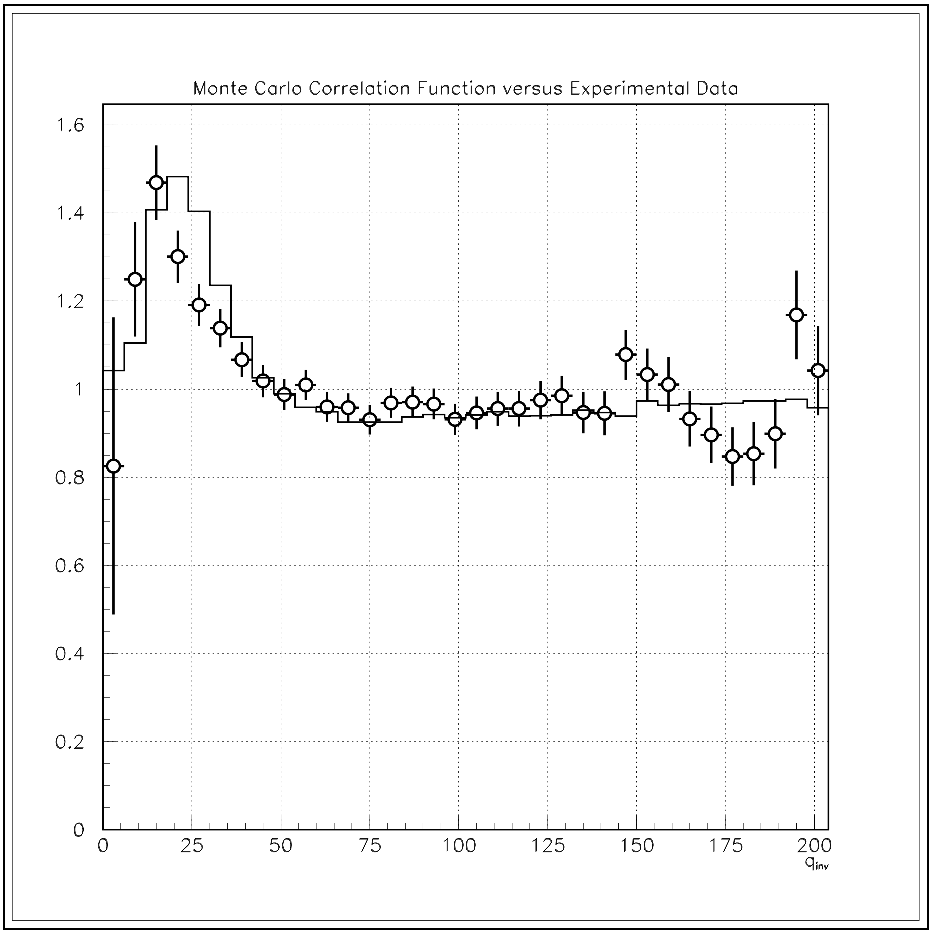

Figure 6.1: Data vs RQMD Proton Correlation Function for 200 GeV/A S+Pb collisions, data vs MC with no systematic errors. The open circles are data, the solid line is MC.

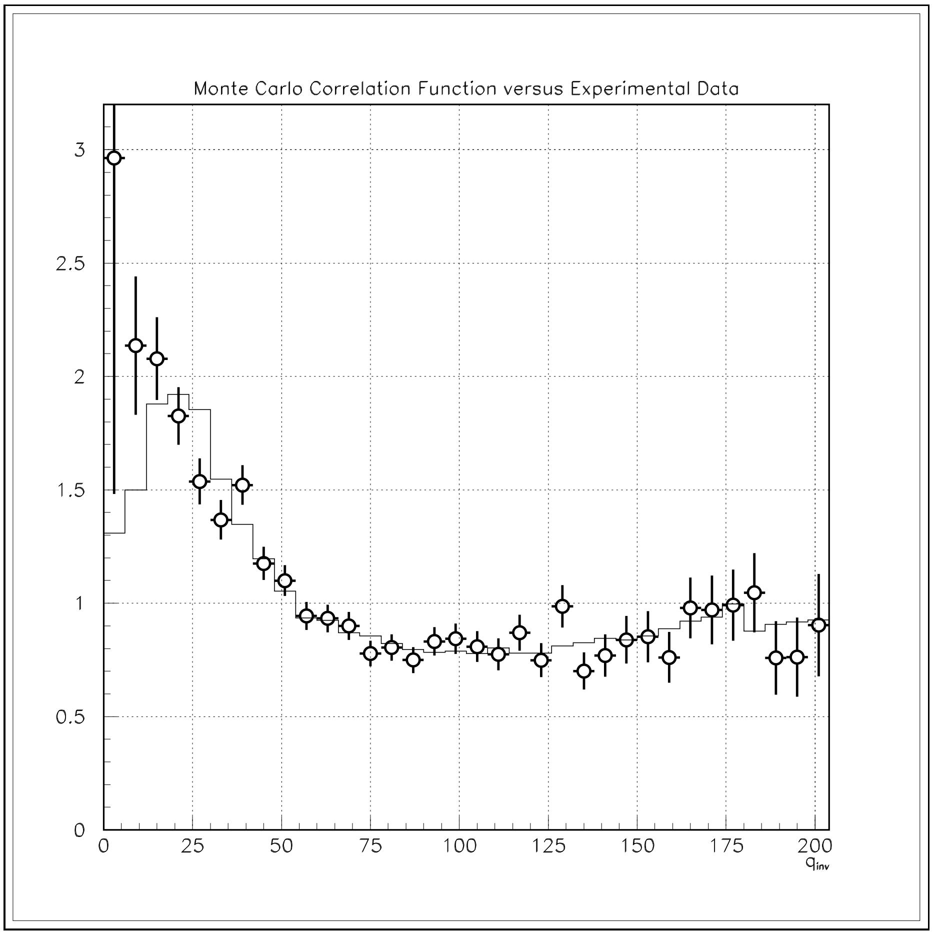

Figure 6.2: Data vs `RQMD` Proton Correlation Function for 450 GeV/A p+Pb collisions, data vs MC with no systematic errors. The open circles are data, the solid line is MC.

We commented on the features of the measured correlation function in section 4.4.5:

1. Both correlation functions, S+Pb and p+Pb, exhibit an enhancement in the low q_{inv} region, signaling the presence of correlation between two protons emanating from the reaction volume

2. Within the statistical errors, both curves are compatible with a maximum (peak) at $q_{inv} \approx 20$ MeV (which is expected – see chapter 2 for explanation)

3. The amplitude of the enhancement is larger in case of p+Pb system, which can be interpreted, qualitatively, as an indication of a smaller particle source.

We note that these characteristics are the same in the data and MC, even though the numerical values are different, especially in the S+Pb case.

It follows from our discussion of the systematic uncertainty in chapter 5 that the event centrality estimate was probably the leading factor in the overall uncertainty of the MC correlation function[1]. We analyzed variations in its shape resulting from certain modifications of the procedure used to determine the impact parameter distribution (section 5.6.3); this was illustrated in Fig. 5.26 for the S+Pb simulation. In case of p+Pb, the results of fitting the multiplicity distributions proved largely insensitive to such modifications and indicated that the impact parameter distribution was very narrow and corresponded to most central

[1]we will return to the issue of Λ decays soon

events[2]. It was decided that a conservative estimate of the sensitivity of the p+Pb correlation function can be made by taking *a half of its variation* between b=0 and 2 fm.

Thus calculated margin of uncertainty is presented in Figs. 6.3 and 6.4, with superimposed data points.

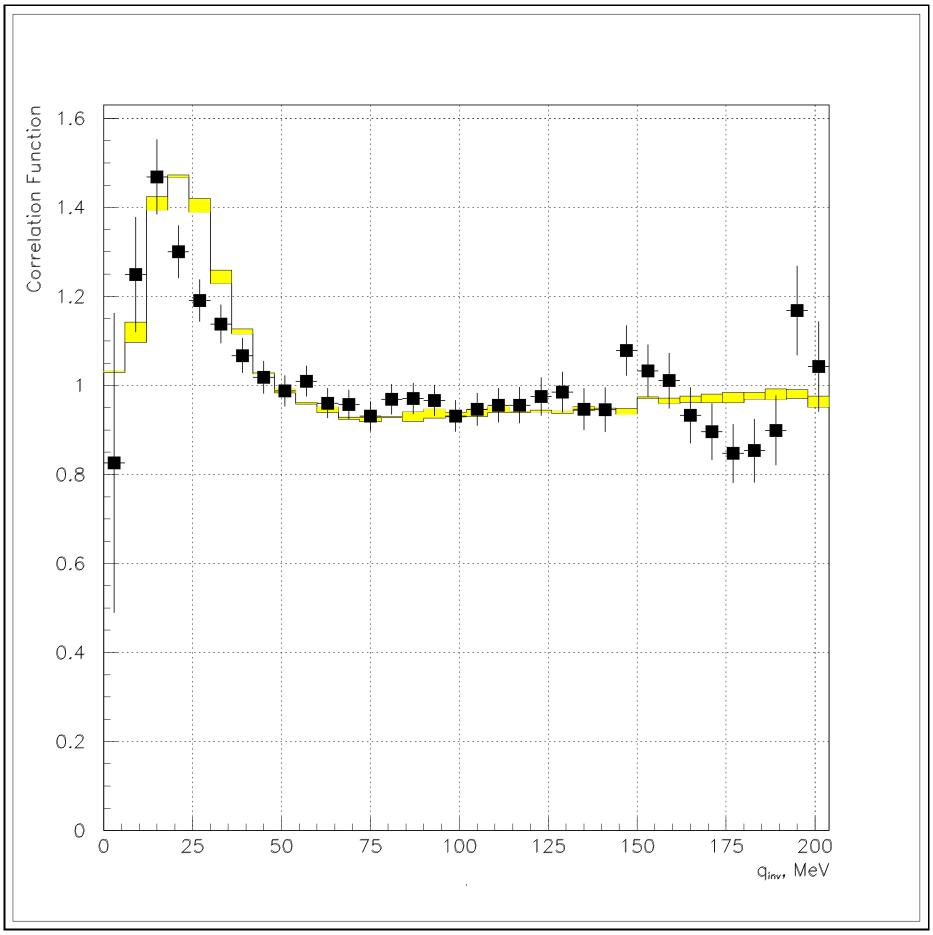

Figure 6.3: Data vs `RQMD` Proton Correlation Function for 200 GeV/A S+Pb collisions, data vs MC with the systematic errors due to the event centrality.

As the S+Pb plots show, the data points in the region q_{inv}=20–40 MeV tend

[2]technically this meant that b was found to be equal to 0

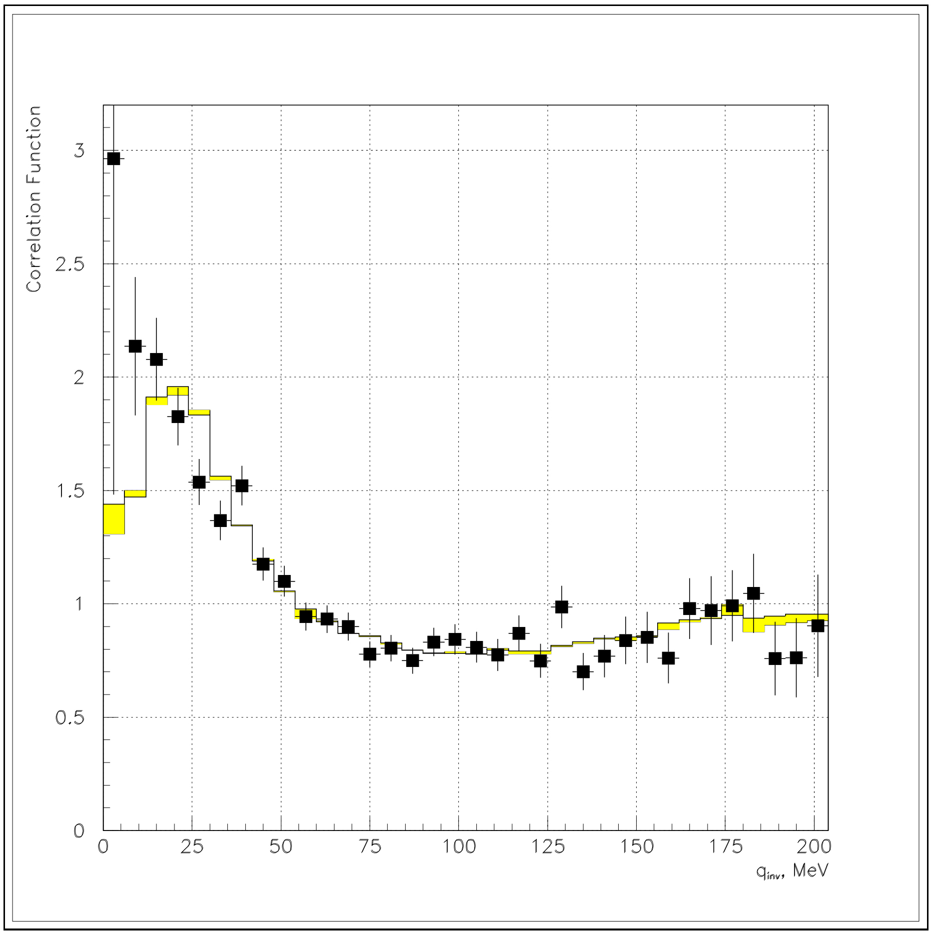

Figure 6.4: Data vs RQMD Proton Correlation Function for 450 GeV/A p+Pb collisions, data vs MC with the systematic errors due to the event centrality.

to lie somewhat lower than the MC predictions, the difference being of the order of 1.5–3 standard deviations[3]. The value of the function around the expected peak ($q_{inv} \approx 20$ MeV) is, roughly, 1.30 ± 0.05 in the data vs 1.48 ± 0.03 in the MC – the quoted errors are statistical for the data and systematic for the Monte Carlo.

There is a similar trend in the p+Pb data sample, but since the statistics of that sample was somewhat poorer, this feature is not as clearly pronounced.

As explained in section 2.3, a source of protons that is more localized is expected to yield a curve with a *sharper peak*, and, reciprocally, a source that is more diffuse would be characterized by a *flatter* correlation function. The difference between the data and the Monte Carlo results could, therefore, be interpreted as an indication that the measured proton source, in S+Pb reaction, is somewhat *larger* than predicted by `RQMD`[4]. An alternative interpretation is that dynamical effects in `RQMD` are different from those in the actual source.

6.3 The Role of Uncertainty Associated with Λ Decays

If we consider the possibility that the `RQMD` predictions regarding the strange baryon production are not precise (a contention, as we already discussed, based on the available experimental data), the resulting additional uncertainty of the Monte Carlo makes the discrepancy smaller.

Using the MC uncertainty margin derived in section 5.7, we present the results for S+Pb collisions in Fig. 6.5, and in Fig. 6.6 for p+Pb. We note that if this

[3] there are total of 4 points, in 6 MeV bins, that exhibit such difference

[4] as we just noted, this is less certain for p+Pb

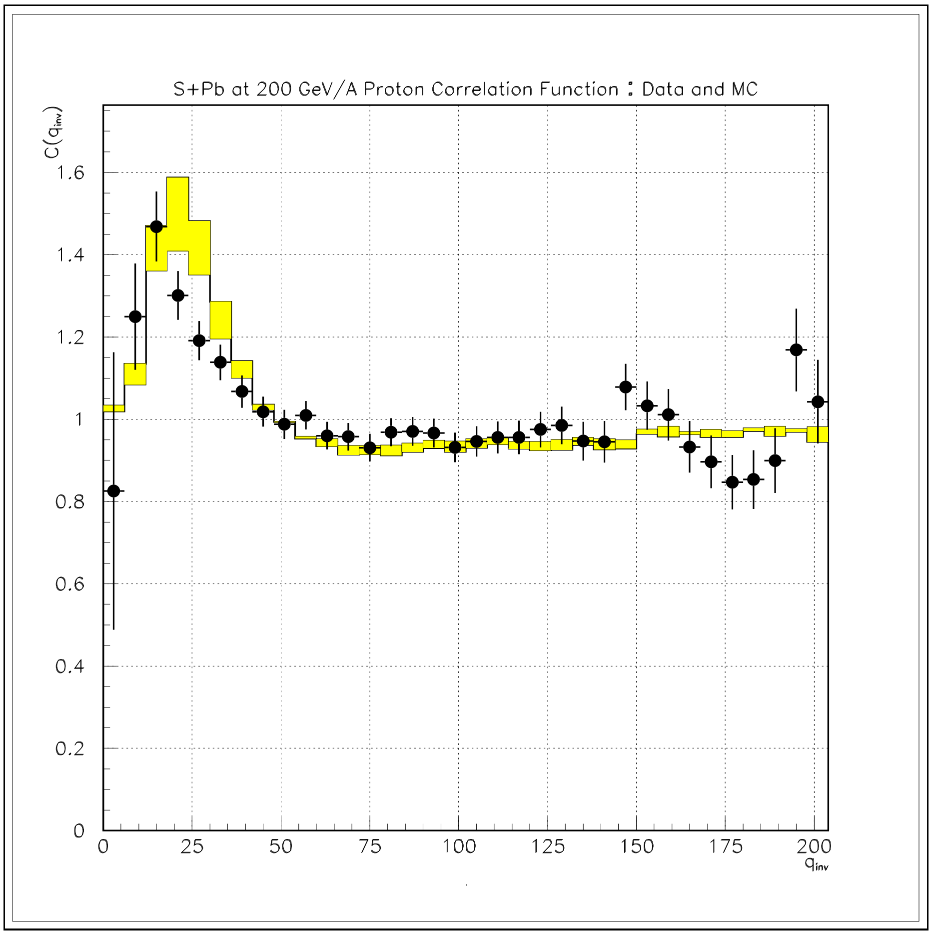

Figure 6.5: Data vs RQMD Proton Correlation Function for 200 GeV/A S+Pb collisions, MC systematic error band band due the Λ contribution uncertainty

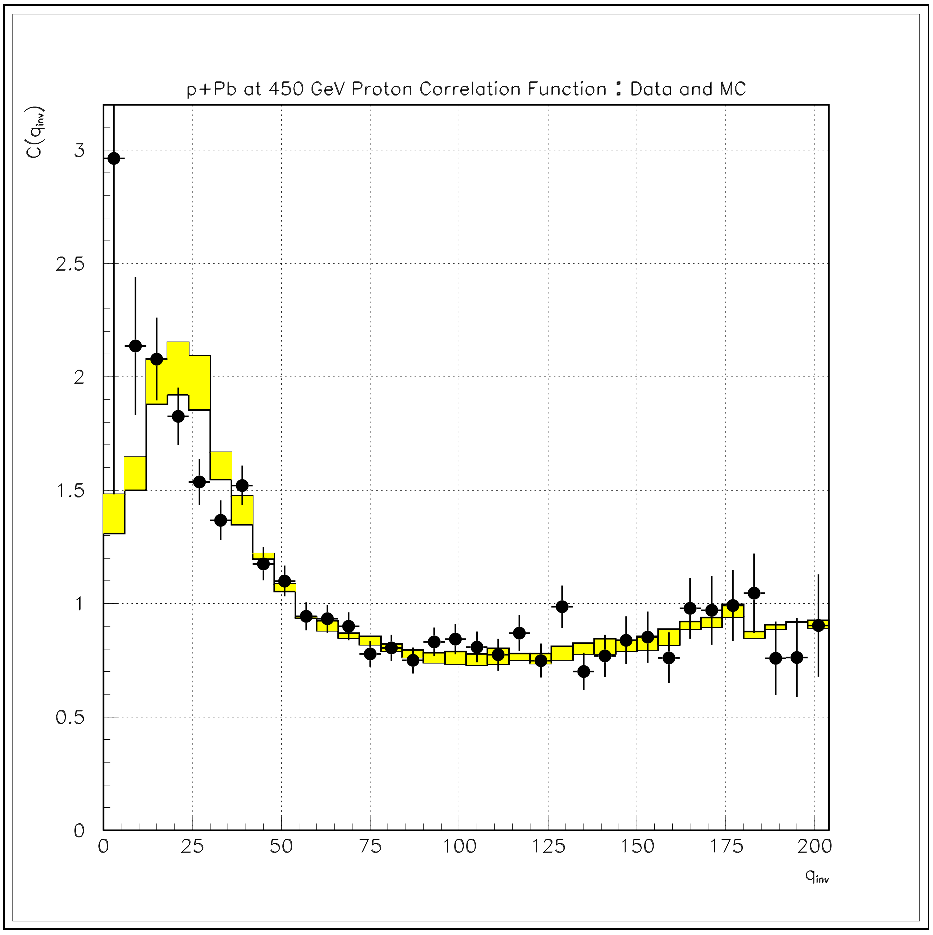

Figure 6.6: Data vs RQMD Proton Correlation Function for 450 GeV/A p+Pb collisions, MC systematic error band band due the Λ contribution uncertainty

uncertainty is taken into account, the discrepancy between the data and Monte Carlo becomes less significant, compared to the statistical errors of the data.

Chapter 7

Conclusions

We have measured two–proton correlations in $^{32}S+^{208}Pb$ collisions at 200 GeV/c per nucleon and $p+^{208}Pb$ collisions at 450 GeV/c, using the data from the focusing spectrometer of the NA44 experiment at the CERN Super Proton Synchrotron. The measurement was possible thanks to the following properties of the spectrometer:

- Good two-particle resolution provided by the high-granularity hodoscope system and the focusing optics

- Reliable particle identification, based on the Čerenkov counters and the precision time-of-flight measurement

The charged particle multiplicity of the measured events was determined by means of the Silicon Pad Detector with 2π azimuthal acceptance, covering the pseudo-rapidity range $1.5 < \eta < 3.3$.

The technique of intensity interferometry of pairs with low relative momentum has been used, whereby the correlation function was defined as

$$C(\mathbf{p}_1, \mathbf{p}_2) = A\frac{R(\mathbf{p}_1, \mathbf{p}_2)}{B(\mathbf{p}_1, \mathbf{p}_2)}$$

where $\mathbf{p}_{1,2}$ are the particles' 3-momenta, $R(\mathbf{p}_1, \mathbf{p}_2)$ ('the real distribution'), is the density of the measured inclusive proton pairs in the phase space, $B(\mathbf{p}_1, \mathbf{p}_2)$ ('the background distribution') is constructed using the standard event mixing technique, and A is a normalization constant. Having introduced a kinematic variable

$$q_{inv} = \frac{1}{2}\sqrt{-\Delta p^\mu \Delta p_\mu},$$

where $\Delta p^\mu = p_1^\mu - p_2^\mu$ and $p_{1,2}^\mu$ are 4-momenta of the particles that constitute the pair, we reduced the above form to

$$C(q_{inv}) = A\frac{R(q_{inv})}{B(q_{inv})} \tag{7.1}$$

We used the experimental data to calculate thus defined correlation function for S+Pb and p+Pb systems and present the results in Figs. 4.16 and 4.17, respectively. The errors in these plots are statistical. The data were also studied from the point of view of their stability with respect to the event selection criteria and procedures, in order to estimate the experimental systematic errors. It was found that such errors are, in general, smaller than statistical.

The prominent feature of the two-proton correlation function, largely defined by the Final State Interactions in the system of two protons leaving the particle source, that one expects to see in the data, is the presence of an enhancement at $q_{inv} \approx 20$ MeV. A difference in the magnitude of this enhancement between S+Pb and p+Pb systems is also expected, due to the vastly different reaction volume. These features, by large, are borne out in the data.

The dependence of the proton correlations on the event multiplicity was found (Figs. 4.32 and 4.32). In both cases, the correlation function formed from events with higher multiplicity tended to have smaller values of the enhancement, that could be interpreted as a signal of a larger source.

The data were also compared with the predictions of the `RQMD` (version 1.08) event generator. The emission points and momenta of individual protons, as defined in `RQMD`, were used to calculate a correlation weight of each pair according to the prescription [14]

$$w(i,j) \equiv |\phi_{\mathbf{k}_{ij}}(\mathbf{r}_i - \mathbf{r}_j - \mathbf{v}_{ij}(t_i - t_j))|^2 \qquad (7.2)$$

where ϕ represents the two-particle wave function and was found by numerical solution of the Scrödinger equation, taking into account both strong and Coulomb interaction. This weight was then used to form the q_{inv} spectrum of proton pairs and the correlation function was calculated in the usual manner, using the event mixing technique to create the "background" sample (see equation 7.1).

In order to make a meaningful comparison between the data and the theoretical result, we have identified and studied the following important factors:

- Acceptance and two–particle resolution of the spectrometer

- Event centrality (i.e. trigger bias)
- Contamination of the proton sample by strange baryon decays

These factors were then incorporated in a sophisticated Monte Carlo scheme.

The two–particle resolution of the spectrometer was taken into account during the calculation of the correlation weights (equation 7.2), by propagating each proton pair, in simulation, through the model of the apparatus and using the standard NA44 track reconstruction software to determine the particles' momenta as they would be measured by the apparatus.

The centrality was estimated using the data from the silicon multiplicity detector in conjunction with a `GEANT` simulation of that detector. A method was developed, whereby the MC multiplicity distributions were matched to the data through a fitting procedure, from which the impact parameter distribution was estimated.

Lastly, we studied the reconstruction of proton tracks coming from Λ decays and calculated a correction factor to be applied to the model predictions when comparing them to the measured correlation function, that turned out to be very significant.

The systematic uncertainty of each component of the Monte Carlo was analyzed. It was established that, if parameters of the model are kept constant, a small discrepancy is observed between MC and S+Pb data, which can be interpreted either as an indication that the measured proton source is somewhat larger than predicted by `RQMD`, or that dynamical parameters if the source are not described quite correctly. The same is true for the p+Pb data, even though it is less pronounced due to larger statistical and systematic errors.

We have demonstrated that at this point, the existing experimental data on strange baryons production, as measured by different experiments (NA35, NA36) are not consistent. If the strange baryon production is estimated from the experiment rather than `RQMD`, an additional uncertainty margin is introduced. This makes the discrepancy between MC and the data less significant.

Bibliography

[1] H. J. Rothe, *Lattice Gauge Theories*, World Scientific, 1992.

[2] C.-Y. Wong, *Introduction to High-Energy Heavy-Ion Collisions*, World Scientific, 1994.

[3] H. R. Schmidt and J. Schukraft, J. Phys. G: Nucl. Part. Phys. (1992) 1705.

[4] B. S. Kumar, Nucl. Phys. **A590** (1995).

[5] R. A. Salmeron, An introduction to the search for the quark-gluon plasma, In B. Sinha, editor, *Quark-Gluon Plasma*, 1990.

[6] B. Müller, Nucl. Phys. **A525** (1995) 3.

[7] J. Barrette et al., Phys. Rev. **C45** (1992) 819.

[8] M. Gonin, Nucl. Phys. **A553** (1993) 799.

[9] J. T. Mitchell et al., Nucl. Phys. **A566** (1994) 415.

[10] D. Rörich et al., Nucl. Phys. **A566** (1994) 35.

[11] S. Pratt, Phys. Rev. **D33** (1986) 1314.

[12] J. D. Bjorken, Phys. Rev. **D27** (1983) 140.

[13] D. Boal, C. Gelbke, and B. Jennings, Rev. Mod. Phys. **62** (1990) 553.

[14] S. Pratt, Two-particle and multi-particle measurements for the quark-gluon plasma, In R. Hwa, editor, *Quark-Gluon Plasma II*, 1995.

[15] B. Jacak, Nucl. Phys. **A590** (1995) 215.

[16] R. J. Morse, *Bose–Einstein Correlation Measurements in 14.6 A GeV/c Nucleus–Nucleus Collisions*, Ph D Thesis, Massachusetts Institute of Technology, August 1990.

[17] A. Sakaguchi, Study of Multiplicity Depdendence of Pion Source Size at NA44 and Expansion Scenario, In *Second International Symposium on Quantum Interferometry Studies, Hiroshima*, 1995.

[18] W. G. Lynch et al., Phys. Rev. Lett. **51** (1983) 1850.

[19] G. Stephans, Target Dependence of Proton Source Sizes at 14.6 GeV/c, In *HIPAGS 93*, 1993.

[20] T. C. Awes et al., Z. Phys. **C65** (1995) 207.

[21] S. E. Koonin, Phys. Lett. **B70** (1977) 43.

[22] P. Dupieux et al., Phys. Lett. **B200** (1988) 17.

[23] H. A. Gustafsson et al., Phys. Rev. Lett. **53** (1984) 544.

[24] W. A. Zajc et al., Nucl. Phys. **A544** (1992) 237.

[25] V. A. Vutsadakis, *Small Relative Momentum Proton Correlations in Relativistic Heavy Ion Collisions*, Ph D Thesis, Massachusetts Institute of Technology, January 1992.

[26] S. Panitkin, Private Communication (SUNY at Stony Brook).

[27] H. Sorge et al., Z. Phys. **C59** (1993) 85.

[28] H. Sorge et al., Phys. Lett. **B289** (1992) 6.

[29] H. Sorge, Phys. Lett. **B344** (1995) 35.

[30] J. Sullivan et al., Nucl. Phys. **A566** (1994) 527.

[31] S. Pratt, Nucl. Phys. **A566** (1994) 103.

[32] M. G. Bowler, Z. Phys. **C29** (1985) 617.

[33] O. E. Vossnack, Nucl. Phys. **A566** (1994) 535.

[34] T. Humanic, Nucl. Phys. **A566** (1994) 115.

[35] S. Pandey, *Investigation of the Space–Time Evolution of the Interaction Region in Heavy Ion Collisions using Bose–Einstein Interferometry Techniques*, Ph D Thesis, University of Pittsburgh, September 1993.

[36] S.Nagamiya, Nucl. Phys. **A400** (1983) 399.

[37] M. G. Bowler, Z. Phys. **C46** (1990) 305.

[38] R. Reid, Annals of Physics **50** (1968) 411.

[39] R. Lednicky et al., Rapport Intenre SUBATECH 1994.

[40] W. A. Zajc, *Two Pion Correlations in Heavy Ion Collisions*, Ph D Thesis, University of California, 1982.

[41] T. Kobayashi and T. Sugitate, Nucl. Instr. Meth. **A287** (1990) 389.

[42] K.L.Brown and Ch.Iselin, CERN-Preprint February 1974.

[43] CERN Library writeup Q121, *Paw - Physics Ananysis Workstation.*

[44] H. Sorge, Nucl. Phys. **A566** (1994) 633.

[45] M.Gaździcki, Nucl. Phys. **A590** (1995) 197.

[46] E.G.Judd, Nucl. Phys. **A590** (1995) 291.

[47] E. Andersen et al., Strangeness Production in p+Pb reactions at 200 GeV/c, In *Strangeness and Quark Matter International Symposium, Crete, Greece*, 1994.

[48] A. Messiah, *Quantum Mechanics*, John Wiley & Sons, 1968.

Appendix A

The Rapidity Variable

For a particle that has, in some reference frame F, energy E and longitudinal momentum p_z, the rapidity is defined by

$$y = \frac{1}{2} ln \left(\frac{E + p_z}{E - p_z} \right) \tag{A.1}$$

We observe that if the particle is traveling in the positive z direction with a velocity β, $E = \gamma m$ and $p_z = \gamma \beta m$ and the rapidity can also be written

$$y_\beta = \frac{1}{2} ln \left(\frac{1 + \beta}{1 - \beta} \right) \tag{A.2}$$

It is easy to verify that under a Lorentz transformation to a new coordinate frame F' that is moving with respect to F with velocity β, the rapidity of the particle in F' is given by

$$y' = y - y_\beta \tag{A.3}$$

It is obvious that the Lorentz transformation is equivalent to a shift in y. This property makes the rapidity an extremely useful variable since the *shape* of the rapidity distributions of the physical observables is Lorentz-invariant.

If a particle is emitted at an angle θ, the rapidity may be written

$$y = \frac{1}{2} ln \left(\frac{\sqrt{m^2 + p^2} + pcos\theta}{\sqrt{m^2 + p^2} - pcos\theta} \right) \tag{A.4}$$

and for high energies, when $p \gg m$, it becomes

$$y \approx \eta \equiv -ln \left(tg \frac{\theta}{2} \right) \tag{A.5}$$

Thus defined η is called pseudorapidity and depends only on the angle of emission θ, which means it can be measured without knowing the momentum of the particle.

Appendix B

Coulomb Wave Functions

In the following presentation we follow [48]. The Schrödinger equation for the system of two particles with charges Z_1, Z_2 is written

$$\left[-\frac{\hbar^2}{2m}\Delta + \frac{Z_1 Z_2 e^2}{r}\right]\psi(\mathbf{r}) = E\psi(\mathbf{r}) \tag{B.1}$$

where E is the energy in the c.m.s. If we put

$$E = \frac{\hbar^2 k^2}{2m} = \frac{1}{2}mv^2 \tag{B.2}$$

$$\gamma = \frac{Z_1 Z_2 e^2}{\hbar v} \tag{B.3}$$

equation B.1 may be rewritten

$$(\Delta + k^2 - \frac{2\gamma k}{r})\psi(\mathbf{r}) = 0 \tag{B.4}$$

It can be shown that this equation has a solution of the form $e^{ikz}f(r-z)$. Upon substitution in B.4 one obtains an equation of the Laplace type whose regular solution at the origin is the confluent hypergeometric series $F(-i\gamma|1|v)$, where $v = ik(r-z)$. The Schrödinger equation B.1 thus has a regular solution

$$\psi_c = e^{-\frac{1}{2}\pi\gamma}\Gamma(1+i\gamma)e^{ikz}F\left[-i\gamma|1|ik(r-z)\right] \tag{B.5}$$

Considering its behavior at the origin, we find

$$\psi_c(0) = e^{-\frac{1}{2}\pi\gamma}\Gamma(1 + i\gamma) \tag{B.6}$$

$$|\psi_c(0)|^2 = \frac{2\pi\gamma}{e^{2\pi\gamma} - 1} \tag{B.7}$$

It is easily recognized as the "Gamow correction factor" (equation 2.13) in section 2.3, with the above defined γ being identical to η; thus, the Gamow factor describes, in essence, the suppression of $|\psi_c|^2$ at the origin due to the Coulomb repulsion between the two particles. It is quite obvious that, strictly speaking, this factor is only applicable in a situation when both particles *are emitted from the same point*, i.e. in case of a point-like particle source.

Appendix C

The RFDTP method

Let c_j^{theory} be the vector of the bin values of the theoretical correlation function $C(q_{inv})$ and b_j the vector of the bin values of the *measured* “background” distribution (formed by the event mixing technique). In [25] the theoretical $C(q_{inv})$ was calculated using a Gaussian source parametrization and the computer code by Scott Pratt [11].

Vector s_j is then defined such that its components are written

$$s_j = c_j^{theory} b_j \tag{C.1}$$

and, taking into account the definition of the correlation function (section 2.2.1), can be considered the “real” q_{inv} distribution, i.e. “the signal”. This signal is then subject to the influence of the spectrometer response function. Denote the *measured* values of s_j as s'_j, then

$$s'_j = a \sum_i R_{ij} s_j \tag{C.2}$$

where a is a normalization factor and the apparatus response is described by the matrix R_{ij}.

Thus, the *RFDTP* approach is to generate R_{ij}, for example by means of a Monte Carlo simulation, and then apply it to the signal distribution s_j. The parameters of the source are then varied in such a way that s'_j fits the experimental data.

Appendix D

The NA44 software and computers

The computers used for the data analysis and simulation in NA44 included[1]

- at CERN, an IBM mainframe (widely known as CERNVM) that existed in 3090-600 and 9000-720 modifications and is currently being phased out, a CERN VAX cluster that included assorted CPU types and recently ALPHA processors, and the newly available `UNIX` facilities (CSF and CERNSP)
- at Columbia University Nevis Labs, a Silicon Graphics Challenge in its 4 processor implementation and an Indy PC
- at participating institutions, VAXen and HP workstations

The main NA44 software complex gradually evolved over the years and was originally related to the code written for the HELIOS experiment. The sheer amount and content of the code is not trivial. In 1993 it was 150k lines, and now,

[1] Description of the online system, see section 3.4.3

in 1996, it is probably well beyond 200k. [2]

The programs intended for processing the data share the same infrastructure and libraries with Monte Carlo applications. That not only makes work easier, but also provides a great degree of consistency in the way geometry and tracking are implemented in both, making Monte Carlo studies of the reconstruction effects very credible. The software includes a tape management system based on the CERN *FATMEN* package.

Originally, the code maintenance was based on `PATCHY`, a rather old package developed at CERN that allowed users to create their own version of the code by "patching" the original source with corrections. It provided the possibility to reference globally defined variables in a consistent way and a degree of automation in updating the master source. It was ported to a number of platforms and provided, via a special intermediate file format, portability of its files.

Later `CMZ` ("Code Management with `ZEBRA`") was introduced that used a tree data structure to organize user files and generated `PATCHY` corrections automatically, making it easy for users to develop parallel and updated versions; it provided a similar capability of handling global definitions. Its binary file format is portable and it can run on a variety of platforms.

The disadvantages of `CMZ` are:

[2] The most advanced version of the Dow Jones Telerate server currently has 800k lines of code, but we at NA44 do not profit from CASE tools and other amenities

1. it is impossible to use the rich assortment of `UNIX` filters on the source files as they normally exist in internal `CMZ` format

2. it is difficult to use the `make` utility, for pretty much the same reason, while `CMZ` does not have its own way to track cross dependencies

3. it does not have a versatile “locking” mechanism, although write protection is available

Still, using `CMZ` was crucial in creating a unified programming environment on a variety of platforms.

Some of the Monte Carlo tasks in the present study required non-trivial computing resources; in particular, generation of the massive ($\propto 10^4$) `RQMD` event sample required significant CPU time (up to 0.5 hour for one central S+Pb event) and storage capacity ($\approx$100kB per event). Part of this work was done using remote HP computers that were writing the `RQMD` output data in real time on the disk located at Nevis Labs by means of `rsh` protocol. This in fact necessitated validation of the data files since there was a possibility of the data being corrupted due to severed network links.